



Block copolymer self-assembly based device structures

Rasappa, Sozaraj; Morris, Michael A.; Holmes, Justin D.

Publication date:
2013

[Link back to DTU Orbit](#)


Citation (APA):
Rasappa, S., Morris, M. A., & Holmes, J. D. (2013). *Block copolymer self-assembly based device structures*.

General rights

Copyright and moral rights for the publications made accessible in the public portal are retained by the authors and/or other copyright owners and it is a condition of accessing publications that users recognise and abide by the legal requirements associated with these rights.

- Users may download and print one copy of any publication from the public portal for the purpose of private study or research.
- You may not further distribute the material or use it for any profit-making activity or commercial gain
- You may freely distribute the URL identifying the publication in the public portal

If you believe that this document breaches copyright please contact us providing details, and we will remove access to the work immediately and investigate your claim.

Title	Block copolymer self-assembly based device structures
Author(s)	Rasappa, Sozaraj
Publication date	2013
Original citation	Rasappa, S. 2013. Block copolymer self-assembly based device structures. PhD Thesis, University College Cork.
Type of publication	Doctoral thesis
Rights	<p>© 2013, Sozaraj Rasappa. http://creativecommons.org/licenses/by-nc-nd/3.0/</p> 
Embargo information	No embargo required
Item downloaded from	http://hdl.handle.net/10468/1237

Downloaded on 2014-03-20T20:39:29Z

Block Copolymer Self-assembly Based Device Structures

Sozaraj Rasappa

Department of Chemistry
University College Cork
Ireland.



UCC

Coláiste na hOllscoile Corcaigh, Éire
University College Cork, Ireland

This thesis is presented to the National University of Ireland for the
degree of
Doctor of Philosophy

May 2013

Supervisor: Prof. Michael A Morris

Co- Supervisor: Prof. Justin D Holmes

Head of Department: Prof. Michael A Morris

Declaration

I Sozaraj Rasappa verify that this Thesis is my own work and I have not acquired a degree in this university or elsewhere on the foundation of this Ph.D. thesis.

Sozaraj. R

Date :

“By the blessings of my parents, teachers, professors and God, I have been able to complete my Ph.D. thesis successfully and it is my pleasure to acknowledge those concerned.”

I would like to thank **Prof Michael A Morris, Prof Justin D Holmes** and **Science Foundation Ireland** from bottom of my heart for giving me this funding opportunity to do my Ph.D. at this university in a high-end project.

I am very grateful and pleased at all time to **Dr Dipu Borah**, PDRF, Chemistry department, University College Cork, for making me to think, create, struggle and understand the basic concepts of my project along with personnel care with no time concepts from the day one of my Ph.D till thesis submission.

Special thanks to **Mr Matthew Shaw**, INTEL Researcher-in-Residence, **Dr Tandra Ghoshal, Dr Parvaneh Mokarian Tabari**, all the members of lab 343 and Poly Team.

I would like to thank **Mr Ramsankar** for his valuable research support all the times in UCC and CRANN lab.

I put my sincere thanks to **Dr Colm Macmanamon, Dr Paul Delany, Mr Atul Thorat, Mr Timothy Collins, Mr Cian Cummins, Mr Atul Chaudhari** and **Lab-115** researchers for excellent knowledge transfer.

A special thanks to **Dr Matthias Jauch** for all the IT assistance over the past few years, especially for retrieving and saving my laptop data during problems.

I always thankful to the administrative and technical staff of UCC- chemistry department for putting up with me for in my Ph.D: **Ms Mary O'Neill, Ms Eileen O'Callaghan, Ms Colette Pettit, Ms Christine Dennehy** and **Mr Terry Horgan**.

I wish to express my deep sense of gratitude to INTEL Researcher-in-Residence, **Mr Peter Gleeson**, for his thoughtful consideration and support to my project in the field of plasma etching technique.

Words are inadequate to express my deep sense of gratitude to my Microscopy guide **Dr Colm Faulkner**, Experimental Officer, AML, CRANN, for his whole hearted encouragement even in holidays, constant guidance all throughout my Ph. D.

I am very much pleased to inscribe my sense of gratitude to senior experimental officers **Dr Markus Boese** and **Mr Tarek Lutz**, AML, CRANN, for their constant encouragement and help whenever needed and special thanks to their timely help.

I express my sincere thanks to **Mr Cathal McCauley**, Senior Technical officer, AML, CRANN and **Mr Dermot Daly**, AML, CRANN, for their constant help throughout the completion of my first year.

I would like to record my sincere gratitude to **Mr Des Keany**, Senior attendant, CRANN and **Mr James Dempsey**, Facilities manager, CRANN for their social support throughout this research work.

My regards further reach all the members of **Integration Group of Theme – II, CRANN** for constant help in my research work.

I wish to express my sincere thanks to all the Professors, faculty members, non-teaching staffs and friends in CRANN, Tyndall and UCC for their constant help throughout the completion of this first year report.

I want to thank my brother **Mr Ezhilan Rasappa** and to my Sister in law **Mrs Kiruthika Ezhilan** for their constant support, care and understandings all the time.

I really pleased to thank my Masters project guide **Dr Nirmala A Grace** for motivating me to do my Ph.D.

Last but not least I have no words to thank my **Father** and **mother** for their continuous support in all my success and failures also I wish to extend my gratitude to their grandson **HariDev**.

I wish to dedicate this thesis to all teachers, lecturers, post doctorates and professors who are strongly supporting and helping for their student betterment.

List of published papers

- [1] **S. Rasappa**, D. Borah, R. Senthamaraikannan, C. C. Faulkner, M. T. Shaw, P. Gleeson, J. D. Holmes, M. A. Morris, *Thin Solid Films* **2012**, 522, 318.
- [2] **S. Rasappa**, D. Borah, C. C. Faulkner, T. Lutz, M. T. Shaw, J. D. Holmes, M. A. Morris, *Nanotechnology*, **2013**, 24, 065503.
- [3] D. Borah, **S. Rasappa**, M. T. Shaw, R. G. Hobbs, N. Petkov, M. Schmidt, J. D. Holmes, M. A. Morris, *J. Mater. Chem. C*, **2013**, 1, 1192.
- [4] D. Borah, **S. Rasappa**, R. Senthamaraikannan, M. T. Shaw, J. D. Holmes, M. A. Morris, *J Colloid Interface Sci.* **2013**, 393, 192.
- [5] D. Borah, **S. Rasappa**, R. Senthamaraikannan, B. Kosmala, M. T. Shaw, J. D. Holmes, M. A. Morris, *ACS Appl. Mater. Interfaces*, **2013**, 5, 88.
- [6] D. Borah, M. Ozmen, **S. Rasappa**, M. T. Shaw, J. D. Holmes, M. A. Morris, *Langmuir*, **2013**, 29, 2089.
- [7] D. Borah, M. T. Shaw, **S. Rasappa**, R. A. Farrell, C. C. O'Mahony, C. M. Faulkner, M. Bosea, P. Gleeson, J. D. Holmes, M. A. Morris, *J. Phys. D Appl. Phys.* **2011**, 44, 174012.
- [8] **S. Rasappa**, D. Borah, R. Senthamaraikannan, C. C. Faulkner, J. J. Wang, J. D. Holmes, M. A. Morris, *Sci. Adv. Mater.* **2013**, 5, 1.

List of Accepted paper

- [1] C. Mcmanamon, P. Delaney, C. Kavanagh, J. J. Wang, **S. Rasappa**, M. A. Morris. Just accepted in *Langmuir*.

List of papers under Review

- [1] *Swift Nanopattern Formation of PS-b-PMMA and PS-b-PDMS Block Copolymer Films Using a Microwave Assisted Technique*
D. Borah, R. Senthamaraikannan, **S. Rasappa**, B. Kosmala, M. T. Shaw, J. D. Holmes, and M. A. Morris
Under Review: ACS Nano

List of submitted papers

- [1] **S. Rasappa**, D. Borah, R. Senthamaraikannan, C. C. Faulkner, M. T. Shaw, J. D. Holmes, M. A. Morris, Submitted to *Journal of nanoscience and nanotechnology – ASP*.

[2] D. Borah, **S. Rasappa**, R. Senthamaraiannan, C. C. Faulkner, M. T. Shaw, J. D. Holmes, M. A. Morris, Submitted to *Langmuir*-ACS.

List of papers in preparation

[1] *Nanodimensioned 3-D Copper Nanowires Fabricated by Soft Block Copolymer Templates for Selective Sensing of Dopamine.*

S. Rasappa, D. Borah, J. D. Holmes, and M. A. Morris

Proposed Journal: Chemistry of Materials

[2] *A Highly Efficient Sensor Platform Using Simply Manufactured Nanodot Patterned Substrates.*

S. Rasappa, T. Ghoshal, D. Bora, R. Senthamaraiannan, J. D. Holmes and M. A. Morris

Proposed Journal: Nanoscale

[3] *Soft-graphoepitaxy for Directed Self-assembly of PS-b-PDMS on Nanoimprinted POSS Substrates*

D. Borah, **S. Rasappa**, R. Senthamaraiannan, A. Francone, C. Simao, O. Lorret, M. Salaun, B. Kosmala, M. T. Shaw, B. Dittert, N. Kehagias, M. Zelsmann, C. S. Torres, and M. A. Morris

Proposed Journal: Chemistry of Materials

[4] *Directed Self-assembly by Graphoepitaxy of Lamellar-forming Polystyrene-block-polydimethylsiloxane Block Copolymer on Nanopatterned POSS Substrates Fabricated by Soft Ultraviolet Nanoimprint Lithography*

D. Borah, **S. Rasappa**, R. Senthamaraiannan, B. Kosmala, M. Salaun, M. Zellsman, M. T. Shaw, O. Lorret, G. Lontos, K. Ntetsikas, A. Avgeropoulos, C. Simao, N. Kehagias, C. S. Torres, and M. A. Morris

Proposed Journal: Macromolecules

[5] *Soft Graphoepitaxy for Large Area Directed Self-assembly of Polystyrene-block-polydimethylsiloxane Block Copolymer on Nanopatterned POSS Substrates Fabricated by Nanoimprint Lithography*

D. Borah, **S. Rasappa**, R. Senthamaraiannan, B. Kosmala, M. Salaun, M. Zellsman, M. T. Shaw, O. Lorret, G. Lontos, K. Ntetsikas, A. Avgeropoulos, C. Simao, N. Kehagias, C. S. Torres, and M. A. Morris

Proposed Journal: Advanced Materials

[7] *Graphoepitaxial Directed Self-assembly of Polystyrene-block-Polydimethylsiloxane Block Copolymer on Substrates Functionalized with Hexamethyldisilazane to Fabricate Nanoscale Silicon Patterns*

D. Borah, **S. Rasappa**, R. Senthamaraiannan, J. D. Holmes, and M. A. Morris

Proposed Journal: Macromolecules

[8] *Nanoscale Template Mask from PS-*b*-PDMS Block Copolymer Self-assembly Based on Microwave Assisted Solvothermal Method*

R. Senthamaraikannan, D. Borah, **S. *Rasappa***, B. Kosmala, J. D. Holmes, and M. A. Morris

Proposed Journal: Nanotechnology

List of Figures

Figure 1.1. Phase diagram for a conformational symmetric diblock copolymer, calculated using self-consistent mean field theory.

Figure 1.2. Schematic of different substrates. (a) SOI substrate, (b) SiO₂ substrate and (c) topographically patterned substrate.

Figure 2.1. 2D Tapping mode AFM topography images of DB74 deposited and annealed at 180 °C for 3 h on (a) bare and (b) PB3 polymer brush anchored substrates and annealed (170 °C/6 h). TEM cross-section image of the same brush layer is in **Figure 2.1(c)**. The inset is the TEM cross-section image of bare silicon substrate. The cartoons inset in **Figures 2.1(a) and (b)** show the proposed lamella orientation in thin films. The PS (green) and PMMA (orange) microphase separate to form PS and PMMA lamellae. In the inset of **Figure 2.1(b)** the brush layer is also indicated.

Figure 2.2. 2D Tapping mode AFM topography images of PS-*b*-PMMA thin films of DB74 (BCP was annealed at 180 °C for 3 h) in toluene deposited on various polymer brushes (all annealed at 170 °C for 6 h).

Figure 2.3. 2D Tapping mode AFM topography images of DB74 microphase separated films after annealing at 180 °C for 3 h) deposited on PB3 polymer brush layers. The polymer brush was annealed at 170 °C for (a) 6 h, (b) 24 h, and (c) 48 h.

Figure 2.4. 2D Tapping mode AFM topography images of BCP films of various molecular weight (DB36, DB74, DB104 and DB176) in toluene deposited on PB3 polymer brush layer. The brush layer was annealed at 170 °C for 6 h whilst the BCP film was anchored annealed at 180 °C for (a) 3 h, (b) 6 h, (c) 12 h and (d) 24 h. The cartoons in **Figure 2.4** (below) show the proposed effect of increasing anneal time (left to right) on pattern formation: PS (green) and PMMA (orange).

Figure 2.5. FTIR spectra of PS-*b*-PMMA (DB74) on brush (PB3) annealed at 180 °C for different times as shown. (a) and (b) are different spectral regions to show main features as indicated. The insert in (a) shows typical data of the peaks used for normalisation as described in the text.

Figure 2.6. Further FTIR data as **Figure 2.5**. Top is quantitative analysis showing the relative decrease of the peak area of -C-O-C and the C=O stretching peak. Bottom left, figure showing the increase in a feature attributable to reaction of PMMA with the substrate as a function of heating period. Bottom right, the development of a band due to presence of formaldehyde type species at these longer heating times.

Figure 2.7. (a) C1s XPS spectra of the brush (PB3) and the BCP (DB74) at various heating times at 180°C (as described in text). **(b)** TGA data the random copolymer brush (PB3) and diblock copolymer (DB74).

Figure 3.1. Top-down SEM images after selective PMMA etch of BCP films of various molecular weight (DB36, DB74, DB104 and DB176) in toluene deposited on PB3 as shown in **Table 2.2**. polymer brush layer. The brush layer was annealed at 170°C for 6 h whilst the BCP film was anchored annealed at 180°C for **(a)** 3 h, **(b)** 6 h, **(c)** 12 h and **(d)** 24 h.

Figure 3.2. SEM images of PS-*b*-PMMA after selective PMMA etch, for 6 s after annealed for 3 h for 180°C **(a)** 18K-18K, **(b)** 37K-37K, **(c)** 52K-52K and **(d)** 85K-91K.

Figure 3.3. SEM images of PS-*b*-PMMA film after 120 s PMMA etch period. **(a)** Tilt image indicating PS removal and **(b)** higher resolution top down image.

Figure 3.4. Top down SEM images of BCP patterns of various molecular weight PS-*b*-PMMA films on silicon substrates. Molecular weights as indicated in figures. All scale bars $1\mu\text{m}$.

Figure 3.5. (a) SEM tilt image of pattern transferred polymer pattern. **(b)** TEM cross-section of the same.

Figure 3.6. Cross-section TEM images of silicon lines formed via BCP pattern transfer. **(a)** PS-*b*-PMMA 91 k–85 k, **(b)** PS-*b*-PMMA 52k–52 k, **(c)** PS-*b*-PMMA 37 k–37 k, **(d)** PS-*b*-PMMA 18 k–18 k.

Figure 4.1. Top-down SEM data for various PS-*b*-PMMA BCPs. **(a)** 18k-18k, **(b)** 37k-37k, **(c)** 52k-52k and **(d)** 85k-91k. The scale bar shown in each one is 200 nm. The insert to **Figure 4.1a** is a TEM cross-section revealing the homogeneity of the

brush layer. The lower layer is bulk silicon and the upper layer is evaporated Pt to protect the polymer film.

Figure 4.2. Calculated (\blacktriangle) and measured (\blacksquare) domain (or pitch size) as a function of molecular weight.

Figure 4.3. Cross-section TEM of silicon nanowires formed by pattern transfer of PS-*b*-PMMA nanopattern transferred into the substrate. (a), (b), (c) show features formed after a silicon etch for periods of 9, 17 and 21 s respectively. (d) is an expansion of the data shown in (a) and (e) is a high resolution image of same showing the silicon lattice planes present in these features. (f) is a small area electron diffraction pattern of a single nanowire feature also illustrating the crystallinity of the etched materials.

Figure 4.4. Cross-section TEM of silicon nanowires formed by pattern transfer of PS-*b*-PMMA nanopattern transferred into the substrate. (a), (b), (c) show features formed after a silicon etch for periods of 9, 17 and 21 s respectively. (d) is a high resolution image of same showing the silicon lattice planes present in these features. Note the triangular feature shape compared to that shown in **Figure 4.3**. The sidewall slope is approximately the same for a pattern sizes suggesting similar etch process and material variables.

Figure 4.5. Details on the PS mask left after a selective PMMA etch. In all cases, SEM (a) and TEM (b and c) reveal the presence of rounded PS features. Data are shown for 18k-18k PS-*b*-PMMA. (d) and (e) are schematics showing how these mask profiles are transferred to silicon to produce the line edge profiles described in **Figures 4.3 and 4.4**.

Figure 4.6. (a-d) SEM top-down images of silicon nanowires produced by pattern transfer using PS-*b*-PMMA 37k-37k at various silicon etch times of 9, 17, 21 and 30s. The graphical image shows the variation in feature size versus etch time for the 85k-91k (\blacksquare), 37k-37k (\blacktriangle) and 18k-18k (\bullet) systems.

Figure 5.1. Top-down SEM images of *in-plane* PDMS cylinders on planner silicon substrates after a sequential CF₄ and O₂ plasma etches of microphase separated PS-*b*-PDMS films. The substrates were anchored with PDMS brush to get microphase separation of PS-*b*-PDMS film by solvent annealing in a saturated toluene

environment for 3 h. Monolayer and multilayers of *in-plane* PDMS cylinders are shown in (a) and (b), respectively. Insets in (a) and (b) are the cross-section SEM images showing monolayer and multilayers of PDMS cylinders and respective schematics. (c) is the FTIR spectrum of the oxidized PDMS cylinders after CF₄ and O₂ plasma etches of microphase separated PS-*b*-PDMS film. The SEM images of PDMS brush anchored planar silicon substrates after cleaning and microphase separation of PS-*b*-PDMS are shown in (d) and (e), respectively. The schematic showing the monolayer and multilayers of PDMS cylinders in dewetted regions is given in (f)

Figure 5.2. Top-down SEM images of PDMS brush anchored planar silicon substrates after cleaning, exposed to UV-O₃ for 5 min (a), 10 min (b) and 15 min (c). The images before cleaning are given in (d), (e) and (f) for 5 min, 10 min and 15 min, respectively.

Figure 5.3. FTIR spectra of PDMS brush anchored planar silicon substrates after cleaning exposed to UV-O₃ for 0 min (a), 5 min (b), 10 min (c) and 15 min (d).

Figure 5.4. (A) Top-down SEM images showing the coverage and extent of dewetting of microphase separated PS-*b*-PDMS films. The PDMS brush anchored substrates after cleaning were exposed to UV-O₃ for 5 min (a), 10 min (b) and 15 min (c). SEM images of PS-*b*-PDMS film coverage on PDMS brush anchored substrates prior to cleaning, exposed to UV-O₃ for 5 min, 10 min and 15 min are shown in (d), (e) and (f), respectively. (B) Top-down SEM images of *in-plane* PDMS cylinders on planar silicon substrates after a sequential CF₄ and O₂ plasma etches of microphase separated PS-*b*-PDMS films. The substrates were anchored with PDMS brush to get microphase separation of PS-*b*-PDMS film by solvent annealing in a saturated toluene environment for 3 h. SEM images of *in-plane* PDMS cylinders on PDMS brush anchored substrates after cleaning and exposing to UV-O₃ for 5 min, 10 min and 15 min are shown in (a), (b) and (c), respectively. Insets in (a), (b) and (c) are the cross-section SEM images. The *in-plane* PDMS cylinders on PDMS brush anchored substrates prior to cleaning, exposed to UV-O₃ for 5 min, 10 min and 15 min are shown in (d), (e) and (f), respectively. Insets in (d), (e) and (f) are the cross-section SEM images.

Figure 5.5. Top-down SEM images of *in-plane* PDMS cylinders on patterned silicon substrates after a sequential CF_4 and O_2 plasma etches of microphase separated PS-*b*-PDMS films. The substrates were anchored with PDMS brush to get microphase separation of PS-*b*-PDMS film by solvent annealing in a saturated toluene environment for 3 h. The PDMS brush anchored substrates after cleaning were exposed to UV- O_3 for 0 min (**a**), 5 min (**b**), 15 min (**c**) and 30 min (**d**) as detailed in the experimental section.

Figure 5.6. Top-down SEM images of *in-plane* PDMS cylinders on planner silicon substrates (**A**) and on patterned silicon substrates (**B**). The substrate was anchored with PDMS brush to get microphase separation of PS-*b*-PDMS film by solvent annealing in a saturated toluene environment for 3 h. The microphase separated PS-*b*-PDMS films were exposed to UV- O_3 for 5 min (**a**), 15 min (**b**) and 30 min (**c**) as an alternative to sequential CF_4 and O_2 plasma etches as detailed in the experimental section.

Figure 5.7. (**a**) Low resolution and (**b**) high resolution top-down SEM images of PDMS cylindrical patterns transferred to underlying planner silicon substrate (inset, (**b**) is the cross-section SEM image). (**c**) Focused Ion Beam (FIB)- cross-section SEM image of PDMS cylindrical patterns transferred to underlying silicon substrate (inset is the schematic showing oxidized PDMS cylinders on silicon nanowires). The pattern transfer was performed with a sequential CF_4 , O_2 , CHF_3/Ar and CHF_3/SF_6 plasma etches as detailed in the experimental section. The substrate was anchored with PDMS brush to get microphase separation of PS-*b*-PDMS film by solvent annealing in a saturated toluene environment for 3 h.

Figure 5.8. (**a**) Top-down low resolution and (**b**) tilted SEM images of PDMS cylindrical patterns transferred to underlying patterned silicon substrate (inset, (**b**) is the cross-section SEM image). The substrate was anchored with PDMS brush to get microphase separation of PS-*b*-PDMS film by solvent annealing in a saturated toluene environment for 3 h. The pattern transfer was performed with a sequential CF_4 , O_2 , CHF_3/Ar and CHF_3/SF_6 plasma etches as detailed in the experimental section.

Figure 6.1. (a) Top-down SEM image of the PS template after selective plasma etching of PMMA block of the microphase separated PS-*b*-PMMA (18k-18k) film on SOI substrate, anchored with a random HO-PS-*r*-PMMA polymer brush. Inset in (a) is the 20° tilted SEM cross-section image. (b) FIB cross-section SEM image of PS template.

Figure 6.2. Low resolution (a) and high resolution (b) top-down SEM images of SiNWs fabricated using PS mask by etch pattern transfer.

Figure 6.3. (a) TEM cross-section image of SiNWs fabricated as described in the text. (b) Expansion of the data shown in (a), and is a high resolution TEM image of same showing the silicon lattice planes present in the features. (c) Small area electron diffraction (SAED) pattern of a single SiNW feature also illustrating the crystallinity of the etched material. (d) Statistical feature size (nm) diagram of SiNWs against feature number. This is a representative sample and the mean size of 7.35 nm (+/- 0.25 nm (3 σ)) can be measured using large data.

Figure 6.4. Energy filtered TEM cross-section images of SiNWs fabricated using PS template mask and etched into SOI substrate: (a) carbon; (b) oxygen and (c) silicon mapping. For each element white contrast denotes higher concentration of the element indicated.

Figure 6.5. Comparative cyclic voltammograms showing the current response (in phosphate buffer) of the non-patterned SOI substrate electrode, a SiNW electrode and the same electrode in the presence of 0.2 M ethanol (0.5 M phosphate buffer solution (pH= 7.4) used in all data). As labeled in figure.

Figure 6.6. (a) Comparative cyclic voltammograms showing the current response of the SiNW electrode with 0.2 M ethanol in a 0.5 M phosphate buffer solution (pH= 7.4) at different scan rates. (b) Plot of I_p vs. $v^{1/2}$ for the anodic process. (c) Tafel plot of E_p vs. $\log v$ for the anodic process. (d) Multiple scanning (10 runs) of the SiNW electrode in 0.2 M ethanol phosphate buffer solution.

Figure 6.7. (a) Comparative cyclic voltammograms showing the current response of SiNW electrode in a 0.5 M phosphate buffer solution (pH= 7.4) at different concentrations of ethanol at a scan rate of 10 mVs⁻¹. (b) Plot of I_p vs. concentration of ethanol.

Figure 7.4.1. (a) Top-down SEM image of the PS template obtained from microphase separated PS-*b*-PMMA (18k-18k) film after selective dry etching of PMMA block (inset is the cross-section SEM image of the PS template), (b) Top-down SEM image of Cu nanowires obtained by depositing copper on PS mask template. (c) Dark-field TEM cross-section images of Cu nanowires with 3-*D* geometry. (d) Bright-field TEM cross-section image of Cu nanowires with 3-*D* geometry.

Figure 7.4.2. (a) X-ray diffraction (XRD) spectrum Cu nanowires and (b) EDS spectrum of Cu nanowires.

Figure 7.4.3. (a) Electrochemical AC impedance spectroscopy (EIS) scan of Cu nanowires on SiO₂ substrate in an electrolyte mixture of 0.1 mol L⁻¹ KCl and 0.5 mmol L⁻¹ Fe(CN)₆^{4-/3-}. (b) and (c) Linear *I-V* characteristics of Cu nanowires on SiO₂ substrate and bare SiO₂ substrate in the electrolyte mixture.

Figure 7.4.4. (a) Charging profile at current 25 mA, 50 mA and 75 mA. (b) discharging profile at current -25 mA, -50 mA and -75 mA of Cu nanoelectrodes in an electrolyte mixture of 0.1 mol L⁻¹ KCl and 0.5 mmol L⁻¹ Fe(CN)₆^{4-/3-} for 100 s. (c) Time analysis of charging and discharging phenomena in Cu nanoelectrodes in the electrolyte mixture.

Figure 8.1. (a) AFM topography 2-*D* image of microphase separated PS-*b*-PMMA (18k-18k) film on SiO₂ substrate anchored with a random HO-PS-*r*-PMMA polymer brush. Inset (a) is the FFT of the topography image. (b) Top-down SEM image of the PS template created by a selective etch of the PMMA block. Inset (b) is the cross-section SEM image. (c) FIB cross-section image of PS template.

Figure 8.2. (a) Top-down SEM image of GeNWs obtained after PS lift-off. Inset (a) is the high resolution SEM image. (b) Bright-field TEM cross-section image of GeNWs obtained after PS lift-off.

Figure 8.3. XRD diffractogram of GeNWs developed on SiO₂ substrate. Silicon features from the substrate can also be seen and are indexed as shown according to JCPDS card nos. 040545 and 271402.

Figure 8.4. Top-down SEM images of GeNWs annealed at **(a)** 573 K and **(b)** 873 K for 30 min in inert environment (Ar). **(c)** Plot of GeNW feature size *vs.* anneal temperature.

Figure 8.5. Raman spectra of GeNWs annealed at different temperatures.

List of Tables

Table 2.1. Characteristics of hydroxyl-terminated random copolymers and diblock copolymers composed of styrene and methylmethacrylate used for present study.

Table 2.2. Water contact angle and film thickness (ellipsometry) of hydroxyl-terminated random copolymers and diblock copolymer films on silicon substrates. Polymer concentration was 1.0 wt % in all cases. Before and after in the deposition column indicate prior to and after the anneal schedule, respectively.

Table 2.3. Pitch and PS width of nanoscale PS templates developed by selective PMMA etch of self-assembled patterns of diblock copolymer films annealed at different times.

Table 3.1. Taguchi Matrix System for OIPT 100 ICP 180 Plasma lab system for PMMA etch rate detection. Constant parameters- total gas flow -Ar+O₂ is 25sccm, Etch time 6 secs, Temperature-20⁰C and He backside 5 Torr.

Table 3.2. Measured data of PS and PMMA film thickness post Ar +O₂ plasma etch at different flow rates of argon+oxygen and PS to PMMA etch selectivity for 2 wt% PS and 4 wt% PMMA homopolymer films after etching.

Table 4.1. Characteristics of hydroxyl-terminated random copolymer and diblock copolymers composed of styrene and methylmethacrylate. M_w is the molecular weight.

Table 5.1. Details of polymer characteristics used in the present study.

Table 5.2. Water contact angle and film thickness data of polymer brush and diblock copolymer films on silicon substrates.

Table 6.1. Characteristics of polymers used for present study.

Table 8.1. Characteristics of polymer used for present study.

List of Schemes

Scheme 1.1. Schematics shows the arrangement of blocks in (a) AB diblock, (b) ABA triblock, (c) ABC triblock

Scheme 1.2. Schematic of different substrates. (a) SOI substrate, (b) SiO₂ substrate and (c) topographically patterned substrate.

Scheme 5.1. Schematic of PS-*b*-PDMS self-assembly on PDMS brush anchored substrates and subsequent etching steps.

Scheme 6.1. Details of the fabrication of SiNWs from microphase separated PS-*b*-PMMA (18k-18k) film on SOI substrate anchored with a random HO-PS-*r*-PMMA polymer brush.

Scheme 6.2. Ethanol oxidation reaction mechanism at the SiNW electrode.

Scheme 7.1. Schematic diagram of the fabrication of Cu nanowires using PS template obtained from microphase separated PS-*b*-PMMA (18k-18k) film on SiO₂ substrate anchored with a random PS-*r*-PMMA polymer brush.

Scheme 7.2 (a) Schematic of conventional EDL supercapacitor. (b) Schematic of electrical double layer formation on 3-*D* structured copper nanoelectrode supercapacitor. (c) Schematic of electron transport phenomenon in top and bottom layer copper nanoelectrodes.

Scheme 8.1. Schematic diagram of the fabrication of GeNWs using a PS template obtained from microphase separated PS-*b*-PMMA (18k-18k) film on SiO₂ substrate whose surface was chemically modified with a random HO-PS-*r*-PMMA polymer brush.

Abbreviations and acronyms

ICT : Information and Communication Technology

CMOS : Complementary metal–oxide–semiconductor

FET : Field effect transistor

MOSFET : Metal oxide semiconductor field effect transistor

UV : Ultra Violet

O₃ : Ozone

PS-*b*-PMMA : polystyrene-*diblock*-poly(methyl methacrylate)

HO-PS-*r*-PMMA : Hydroxyl terminated-polystyrene-*random*-poly(methyl methacrylate)

PMMA : polymethylmethacrylate

PS: Polystyrene

PS-*b*-PDMS : polystyrene-*block*-polydimethylsiloxane

PDMS : Polydimethylsiloxane

BCP : block copolymer

SEM : Scanning electron microscope

TEM : Transmission electron microscope

AFM: Atomic force microscope

TGA : Thermal gravimetric analysis

XPS : X-ray photoelectron spectroscopy

FTIR : Fourier transform infrared spectroscopy

FIB : Focused ion beam microscope

ICP : Inductively coupled plasma

RIE : Reactive ion etching

DSA : Directed self-assembly

IC : Integrated circuit

SOI : Silicon on insulator

ITRS : International technology roadmap for semiconductors

RF : Radio frequency

ARDE : Aspect ratio dependent etching

OPIT : Oxford instruments plasmalab technology

CV : Cyclic voltammetry

EDLC : Electric double layer capacitor

SC : Super capacitor

θ_a : Contact angle

DI : Deionised water

SiNW : Silicon nanowire

GeNW : Germanium nanowire

CVD : Chemical vapour deposition

T_g : Glass transition temperature

JCPDS : Joint committee on powder diffraction standard

L_C : Crystallite grain size

I-V : Current-Voltage

Table of contents:**Chapter 1: Introduction**

1.1. Current CMOS device fabrication and its challenges	1
1.2. What are block copolymers?	3
1.3. Diblock copolymer phase diagram	4
1.4. Physical parameters in block copolymer films	6
1.5. Surface neutralization using brush Chemistry	7
1.6. Graphoepitaxy method to control alignment	8
1.7. Metal and semiconductor nanowires	9
1.8. Types of substrates	10
1.9. References	11

Chapter 2: Polymer brush chemistry for PS-b-PMMA self-assembly

2.1. Abstract	14
2.2. Introduction	14
2.3. Materials and methods	16
2.3.1. Materials	16
2.3.2. Preparation of anchored brush substrates	16
2.3.3. Deposition of the diblock copolymer and pattern formation	17
2.3.5. Characterisation	17
2.3.5.1. Contact angle measurements	17
2.3.5.2. Film thickness measurements	17
2.3.5.3. Atomic Force Microscope (AFM)	17
2.3.5.4. FTIR measurements	18
2.3.5.5. X-ray photoelectron spectroscopy (XPS)	19
2.3.5.6. Thermal gravimetric analysis (TGA)	19
2.3.5.7. Scanning electron microscope (SEM)	19
2.3.5.8. Focused ion beam (FIB) and transmission electron microscope (TEM)	19
2.4. Results and discussions	19
2.4.1. Effect of polymer brush on BCP pattern formation	19

2.4.2. Characterisation of the brush layer	20
2.4.3. Variation of the brush and effects on pattern formation	21
2.4.4. Effect of brush anneal time on pattern formation	23
2.4.5. Effect of BCP anneal time and molecular weight on pattern formation	24
2.4.6. FTIR, XPS and TGA analysis of the BCPs	27
2.4.7. General discussion of the results	31
2.5. Conclusions	33
2.6. References	33

Chapter 3: BCP template to nanowire fabrication by ICP plasma etch

3.1. Abstract	37
3.2. Introduction	37
3.2.1. Plasma processing for development of nanoelectronics	39
3.3. Materials and methods	39
3.3.1. Plasma etching	39
3.3.2. BCP polymer development	39
3.3.3. Film characterization	43
3.3.4. Scanning electron microscope (SEM)	43
3.3.5. Focused ion beam (FIB) and transmission electron microscope (TEM)	43
3.4. Results and discussions	43
3.5 Conclusions	51
3.6. References	52

Chapter 4: Feature size control by Plasma over-etch technique

4.1. Abstract	54
4.2. Introduction	54
4.3. Materials and methods	55
4.3.1. Materials	55
4.3.2. Polymer brush deposition and BCP thin film preparation	56
4.3.3. Soft mask template preparation and pattern transfer	56

4.3.4. Characterization of materials	56
4.4. Results and discussions	57
4.4.1. Polymer brush and BCP self-assembly	57
4.4.2. Feature size control by plasma over-etch	59
4.5. Conclusions	64
4.6. References	65

Chapter 5: PS-b-PDMS self-assembly and its pattern transfer

5.1. Abstract	67
5.2. Introduction	67
5.3. Materials and methods	69
5.3.1. Materials	69
5.3.2. Polymer brush deposition	70
5.3.3. BCP thin film preparation	70
5.3.4. Ultraviolet-ozone (UV-O ₃) treatment	70
5.3.5. Plasma etching of BCP thin films	71
5.3.6. Characterization of materials	72
5.3.6.1. Contact angle measurements	72
5.3.6.2. Film thickness measurements	72
5.3.6.3. FTIR measurements	72
5.3.6.4. Scanning electron microscope (SEM)	72
5.4. Results and discussion	73
5.4.1. BCP self-assembly on PDMS brush	73
5.4.2. Dewetting and UV-O ₃ exposure of PDMS brush	74
5.4.3. FTIR study of the PDMS brush	77
5.4.4. BCP self-assembly on UV-O ₃ exposed polymer brush	78
5.4.5. Directed self-assembly by graphoepitaxy	80
5.4.6. UV-O ₃ exposure of microphase separated PS-b-PDMS films	81
5.4.7. Pattern transfer to underlying substrate	82
5.5. Conclusions	84
5.6. References	85

Chapter 6: Ultrathin silicon nanowire fabrication for sensors

6.1. Abstract	88
6.2. Introduction	88
6.3. Materials and methods	90
6.3.1. Materials	90
6.3.2. Polymer brush deposition	90
6.3.3. Block copolymer film deposition	91
6.3.4. On-chip mask development and pattern transfer	91
6.3.5. Characterization of materials	91
6.3.6. Electro-oxidation of ethanol by the SiNW structure	92
6.4. Results and discussions	92
6.4.1. Fabrication of SiNW structure from BCP thin films	92
6.4.2. Electro-oxidation of ethanol by the SiNW electrode	96
6.5. Conclusions	101
6.6. References	102

Chapter 7: 3-D copper nanowires as an electrode material

7.1. Abstract	105
7.2. Introduction	105
7.3. Materials and methods	106
7.3.1. Development of diblock copolymer self-assembled patterns	106
7.3.2. Preparation of diblock copolymer templates	107
7.3.3. Development of capacitor structures	107
7.3.4. Characterization of materials	107
7.3.5. Electrochemical characterization of copper nanowires	108
7.4. Results and Discussions	108
7.5. Conclusions	114
7.6. References	114

Chapter 8: Fabrication of germanium nanowires via BCP template

8.1. Abstract	116
---------------	-----

8.2. Introduction	116
8.3. Materials and methods	117
8.3.1. Materials	117
8.3.2. BCP film preparation	118
8.3.3. PS template preparation	118
8.3.4. Ge deposition and PS template lift-off	119
8.3.5. Annealing of GeNWs	119
8.3.6. Material characterization	120
8.4. Results and discussion	121
8.4.1. BCP self-assembly and PS template fabrication on SiO ₂ substrate	121
8.4.2. Fabrication and characterisation of GeNW arrays	122
8.4.3. Effect of thermal treatment on GeNWs	125
8.5. Conclusions	127
8.6. References	127
Chapter 9: Conclusions	130

Abstract

This thesis investigated the block copolymer (BCP) thin film characteristics and pattern formation using a set of predetermined molecular weights of PS-*b*-PMMA and PS-*b*-PDMS. Post BCP pattern fabrication on the required base substrate a dry plasma etch process was utilised for successful pattern transfer of the BCP resist onto underlying substrate. The resultant sub-10 nm device features were used in front end of line (FEoL) fabrication of active device components in integrated circuits (IC). The potential use of BCP templates were further extended to metal and metal-oxide nanowire fabrication. These nanowires were further investigated in real-time applications as novel sensors and supercapacitors.

1.1. Current CMOS device fabrication and its challenges

The field of Information and Communication Technology (ICT) is witnessing growth rate unprecedented in history [1]. Moore's Law results in strong increases in demand for the semiconductor industries towards chip manufacturing and continued scaling of transistors [2, 3]. This device size miniaturization seen over forty years results in increase in device speed, package density, low power use combined with low cost production of consumer electronics. Transistor design has been largely unchanged for many years and progress has been around scaling of the basic CMOS device [4]. The miniaturisation technique has been enabled by both the top-down and bottom-up approaches in the semiconductor industries [5, 6].

The most common top-down approach to fabrication of device structures involves photolithographic patterning techniques using short-wavelength optical sources [7]. Photolithography is prominent in the field of semiconductor chip manufacturing because of its high degree of refinement and ability to reach the transistor size of sub-100 nm. With high pattern fidelity photo lithography uses a short wavelength sources such as, UV (Ultra Violet), extreme UV and X-rays to obtain feature size less than 100 nm regime [8-10].

The scanning electron beam microscopy (SEM) technique can be used as a lithographic technique. It uses a beam of energised electrons to create patterns at sub-50 nm resolution. Scanning Ion beam lithography is also a valuable methodology to create the patterns on a surface in the nanoscale regime but with lesser resolution than possible with the electron beam technique [11].

Nanoimprint lithography is a kind of mechanical stamping or molding technique which has the ability to manufacture feature size between 20 and 40 nm without using expensive light electrons or ion sources [12]. The working principle of these imprint techniques all vary, but they are all based on a basic concept of making a master "stamp". The application of these stamps creates sub-50 nm resolution patterns. One variation of the technique is where the stamp's surface is coated with a very thin film (the ink) that can then be deposited ("inked") directly onto the surface to reproduce the stamp's pattern. A guiding patterning of a molecular monolayer on a surface can be achieved for example by stamping an ink of thiol molecules that contain a sulfur end group functionalized organic molecules

directly onto a gold-coated surface. On the other hand the stamp physically presses the pattern into a thin layer of material. This surface layer is typically a polymeric material that is made pliable for the molding process by being heated during the stamping procedure. Plasma etching can then be used to remove the thin layer of the masking material under the stamped regions; any residual polymer is thus removed, and a nanoscale lithographic pattern is left on the surface. Another variation is to make the relief pattern out of photoresist on a silicon wafer by optical or electron-beam lithography and then pour a liquid precursor - for example, polydimethylsiloxane, a form of silicone - over the pattern and then cure it. The result is a rubbery solid that can be peeled off and used as a stamp. These stamps can be inked and printed as described above, or they can be pressed to the surface and a liquid polymer is allowed to flow into the raised regions of the mask by capillary action and cured in place. A distinction for this latter approach is that the stamp is flexible and can thus be used to print nanoscale features on curved surfaces. These nanoscale printing techniques offer several advantages beyond the ability to use a wider variety of materials with curved surfaces. In particular, such approaches can be carried out in ordinary laboratories with more inexpensive equipment than that needed for conventional submicron lithography.

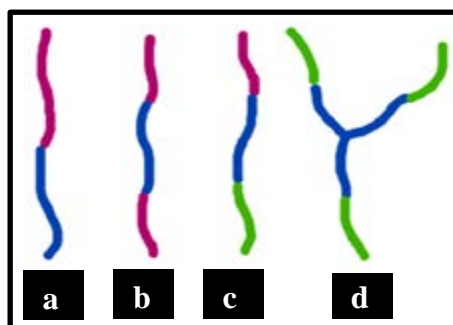
The challenge for all top-down techniques is that, while they work well at the microscale (at millionths of a metre), it becomes increasingly difficult to apply them at nanoscale dimensions. A second disadvantage is that they involve planar techniques, which means that structures are created by the addition and subtraction of patterned layers (deposition and etching) and arbitrary three-dimensional objects are difficult to construct. In order to overcome these issues another process methodology called the bottom-up approach may prove to be significant [13].

Bottom-up, or self-assembly, approaches to nanofabrication use chemical or physical forces operating at the nanoscale between molecules or objects to assemble basic units into larger structures. As component size decreases in nanofabrication, bottom-up approaches provide an increasingly important complement to top-down techniques [14]. The bottom-up approach is the realm of nanoscience and nanotechnology and derives from research that allows molecular and atomic manipulation. Bottom-up nanofabrication process involves spontaneous self-

assembly. Lithographic methods using the “Bottom-up” approach of self-assembly allow block copolymers, colloidal particles, biocompatible materials [15] which generate pattern through local chemical interactions between molecules or particles. Diblock copolymers are popular materials for the self-assembly. Here two chemically distinct blocks microphase separate from each other to form nanoscale domains in a regular periodic structure [13]. The methodology of the self-assembly using block-copolymers is cost-effective and may have both expense, dimension and ease of fabrication advantages compared to the current UV lithography technique [14, 13]. The nanopatterns fabricated by the block copolymer systems are highly reproducible and stable. Block copolymer systems could offer a high resolution enhancement compared to the current UV lithography techniques [15, 13].

1.2. What are block copolymers?

A polymer is a large molecule (macromolecule) composed of repeating regular structural units typically connected by covalent chemical bonds. A block copolymer is a polymer which is formed by adding two or more monomeric species distinct blocks as shown in scheme1.1.



Scheme 1.1. Schematics shows the arrangement of blocks in (a) AB diblock, (b) ABA triblock, (c) ABC triblock and (d) starblock polymers [16].

The blocks in the block copolymer can be connected in a different ways. Since the block copolymers comprise two or more homopolymer subunits linked by covalent bonds, the union of the homopolymer subunits may require an intermediate non-repeating subunit, known as a junction block. Block copolymers with two or

three distinct blocks are called diblock copolymers and triblock copolymer, respectively as shown in scheme 1.1.a and 1.1.b.

The main body of work in this thesis is focused mainly on the PS-*b*-PMMA (polystyrene-*b*-poly (methyl methacrylate)) block copolymer is abbreviated as PS-*b*-PMMA (or PS-PMMA). This is made by first polymerizing styrene, and then subsequently polymerizing MMA. This polymer is a "diblock copolymer" because it contains two different chemical blocks.

1.3. Diblock copolymer phase diagram

The blocks in the diblock copolymers tend to phase separate into micro domains forming different mesophase structure. The size scales of domains are governed by the chain dimensions and the block ratio determines the mesa phase structure. The predicted equilibrium mesa phases for diblock copolymers are Spheres (S), Cylinder (C), Gyroid (G) and Lamellae (L) which are shown in the phase diagram Figure 1.1. PS-*b*-PMMA are of interest because they can demonstrate excellent "microphase separation" and form well-arranged nanoscopic dimensioned structures. For PS-*b*-PMMA phase separation is induced on a scale that is directly related to the size of the copolymer chains and results in morphologies typified by a pattern of chemically distinct domains of periodicity λ in the 10-100 nm range. The origin of this self-assembly derives from the immiscible of PS and PMMA with each other similar to oil and water. PS and PMMA mixtures will not mix together and instead macrophase separate from each other. PS-*b*-PMMA behaves in a similar way called microphase separation. PS can be considered as "oil-like" combination of a hydrophobic first block and a "water-like" hydrphilic second block (PMMA). Thus they would like to phase separated but this is prevented by the covalent bond between the blocks. This results in "microphase separation" in which the "oil" and "water" phases separate to form nanometer-sized structures. The possible structures are shown in **Figure 1.1**.

The phase behaviour (**Figure 1.1**) of block copolymers can be theoretically predicted within the self-consistent Field theory, according to which the critical parameters are:

$$f = \text{volume fraction of one block (the minority one)}$$

χ = Flory–Huggins interaction parameter, which is inversely proportional to temperature, and reflects the interaction energy between different segments

N = degree of polymerization.

When χN exceeds a critical value, $(\chi N)_{\text{ODT}}$ (ODT= order–disorder transition) the block copolymer microphase separates into a periodically ordered structure, with a length scale of approximately ~5-500 nm. The structure that is formed depends on the copolymer architecture and composition and it is the one that most minimizes the interfacial tensions.

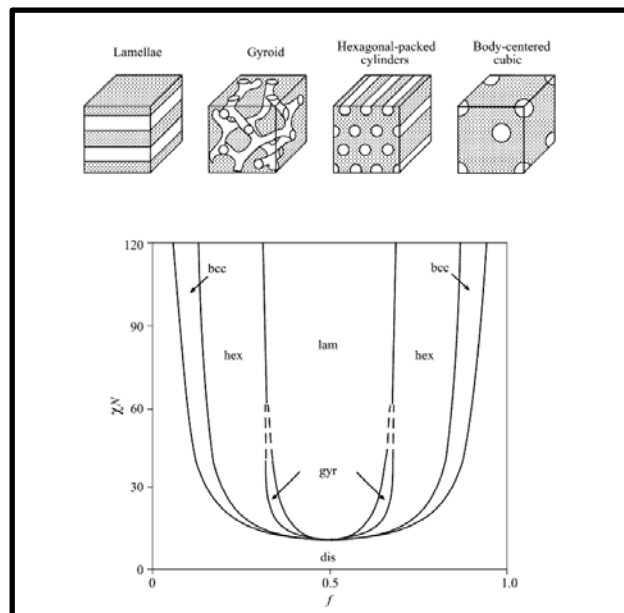


Figure 1.1.Phase diagram for a conformational symmetric diblock copolymer, calculated using self-consistent mean field theory [17].

For diblock copolymers like PS-*b*-PMMA, a lamellar (lam) phase is observed for *symmetric diblocks* ($f = 0.5$), whereas *asymmetric diblocks* form hexagonal-packed cylinder (hex) or body-centred cubic (bcc) spherical structures. A complex bicontinuous cubic gyroid (gyr) phase has also been identified for block copolymers between the lam and hex phases near the ODT and a hexagonal perforated layer (hpl) phase has been found to be metastable in this region [17].

1.4. Physical parameters in block copolymer films

Block copolymer films can be prepared by the spin-casting technique, where drops of a solution of the polymer in a volatile organic solvent are deposited on a spinning solid substrate as detailed in *Chapter 2* (often silicon wafers are used due to their uniform flatness). The polymer film spreads by centrifugal forces and the volatile solvent is rapidly driven off. With care, this method can deposit films with a low surface roughness over areas of square centimetres. The film thickness can be controlled through the spin speed and the concentration of the block copolymer solution or the volatility of the solvent which also influence the surface roughness. Dip coating is another reliable method for fabricating uniform thin films. Whatever the deposition technique, if the surface energy of the block copolymer is much greater than that of the substrate dewetting will occur.

Careful control of film thickness is required to generate uniform thin films. In the case that wetting condition takes place, two different situations can happen;

1. Symmetric wetting, if the same block is located at both interfaces.

$$\text{Film thickness is: } T = nL \quad (1.1)$$

where L is the intrinsic polymer-length scale.

2. Asymmetric wetting, if a different block preferentially wets the interface with the substrate or air.

$$\text{The film has a uniform thickness: } T = (2n + 1) L/2 \quad (1.2)$$

In both **equations (1.1 & 1.2)**, n is an integer.

In block copolymer thin films, film formation by spin or dip coating usually results in a disordered structure “frozen-in” by rapid solvent evaporation. The assembly of these films into regular nanometer scale domains by micro-phase separation is often facilitated by thermal annealing. Here, polymer chains, in the film, become increasingly mobile above the material’s glass temperature adjusting themselves in order to achieve the most favourable energetic configuration. The annealing temperature should be below the point at which the template pattern disorders (Order To disorder transition) due to very rapid reaction of the polymer chains. In general the range of the annealing temperature (T) should be:

$$T_{\text{Glass Transition}} < T < T_{\text{OTD}} \quad (1.3)$$

1.5. Surface neutralization using brush Chemistry

BCP systems offer excellent control over pattern dimension and structure, lamellar, cylindrical, spherical and gyroid (as shown in **Figure 1.1**). However, the use of BCP methods can prove a challenge because the interfacial interactions of the polymer blocks with the substrate and the environment can influence pattern formation and, in particular pattern orientation for use of BCP in lithography. In cylinder or lamellae forming BCP systems the micro domain orientation can be either parallel or vertical to the substrate surface plane depending on preferential interface interactions or surface energy effects. Very frequently, a perpendicular domain orientation in thin films is desirable so it can be used as an effective template or mask for substrate feature development as outlined above [18]. The use of a host of methods such as solvent annealing, thermal annealing, and electric field application, homopolymer blending and chemical modification of substrate is used to improve the wetting behaviour and to control the interfacial and surface energies to control surface coverage and pattern orientation [19]. The concept of attaching random copolymers to a substrate surface as a ‘brush’ so that surfaces neutral to both blocks can be created is well established [20]. Molecular grafting of random copolymers like HO-PS-*r*-PMMA, PS-OH and PDMS-OH to a substrate surface can result in a thin, uniform and non-preferential (i.e. chemically neutral to both blocks) brush layer. This brush enables the control of wetting behaviour and interfacial interactions of the diblock copolymer components and the substrate thereby promoting perpendicular or parallel orientation is strongly dependent on effective orientation control in the BCP system of PS-*b*-PMMA and the relative composition of the HO-PS-*r*-PMMA brush layer. Whilst authors have optimised the brush composition and molecular weight to properly define pattern orientation, there have been few systematic studies of the effect of the brush molecular weight on pattern control and thermal stability of thin BCP films as discussed in **Chapters 2&4**.

Andreozzi *et al.*, have studied brush effects on the dimensions and orientation of cylinder forming PS-*b*-PMMA noting strong cylinder diameter changes. The PS-*b*-PMMA system has such relevance to the microelectronics industry as a potential alternative to conventional photolithography (since PS and PMMA are used as resists in fabrication), it is of considerable interest to understand

the interaction and the effect of the polymer brush with the pattern forming BCP. PS-*b*-PDMS is also a potential BCP system for creation of large area alignment with desired nanoscale region. For the PS-*b*-PDMS (polystyrene-*b*-polydimethylsiloxane) BCP system two major issues arise: strong surface dewetting due to high hydrophobicity and difficulties in controlling feature orientation, particularly, for definition of parallel versus vertical cylinder alignment. To overcome these limitations, a surface pre-treatment with a PDMS brush is usually required. However, it should be noted that whilst the use of a PDMS brush can improve these BCP thin films, dewetting the BCP coverage at the substrate and regions of irregular thickness can remain problematic as reported here and elsewhere. However, despite the imperfect nature of these potentially important films, reports of methods of tuning the surface chemistry of PDMS brush in an effort to improve the BCP film and control orientation is scant. In order to improve the brush chemistry using simple, reproducible and facile processing we have developed a methodology using UV-O₃ exposure to facilitate highly regular self-assembly of this PS-*b*-PDMS system over large substrate areas [21]. Results are highly promising and prove the ability of the technique to yield an “on-chip mask” for etch transfer to the substrate surface.

1.6. Graphoepitaxy method to control alignment

Graphoepitaxy is a technique used to control the alignment (i.e. pattern direction to a structure feature) over large area [21]. Topographically patterned substrates for hard-graphoepitaxy are fabricated by e-beam lithography. The science behind this technique is that the side walls will act as a barrier for the diblock polymer and prevent random spreading of the BCP film, instead it forces the pattern to align to the topography in a narrow size regime. Graphoepitaxy is almost exclusively used for the directed assembly method for microphase separation of block copolymers [21, 22]. This methodology represents a combination of both top-down and bottom-up approaches for the generation of highly regular patterns on substrates. The deposition of block copolymer thin film over a prepatterned substrate and subsequent high-temperature annealing and the physical confinement imposed by the side wall of the topographic pattern enforces lateral ordering of self-assembled nanodomains along the pattern edge as discussed in *Chapter 4*. The

regular closed packing of neighbour nanodomains gives the lateral formation of ordered surface morphology throughout the film plane and results in highly dense nanopattern assembly within the topographic confinement. This process enhances the directed self-assembly of block copolymers in the trenches of prepatterned substrates. This graphoeptaxy technique is a multistep process starting from photolithography to subsequent pattern transfer to get the prepatterned substrate. Directed self-assembly (DSA) in graphoeptaxy increases the coherence length of the features over microscopic dimensions which is limited in planar substrates to micron scales or less. DSA is the only way of confining BCP in a narrow region to get the translational alignment with coherence length of a few centimeters.

Once the “ideal” BCP patterns are fabricated on a substrate, one block can be removed selectively and the other block subsequently used as an etch mask to transfer the pattern to the substrate. Whilst originally wet chemistries were used as etches, the advantages of dry plasma etching, where chemically active radicals/ions are used to remove material, have led to its almost exclusive use. As mentioned in detailed in *Chapter 3* the advantages of inductively coupled plasma (ICP) and reactive-ion etching (RIE) methodologies in terms of anisotropy (i.e. etching in vertical direction only with little or no lateral etching), large area and high-density at relatively low pressures have led to the adaption of these sources in industry. Perhaps the greatest advantage of plasma techniques in modern integrated-circuit (IC) manufacturing is the uniformity of the etch process which results in extremely uniform features.

1.7. Metal and semiconductor nanowires

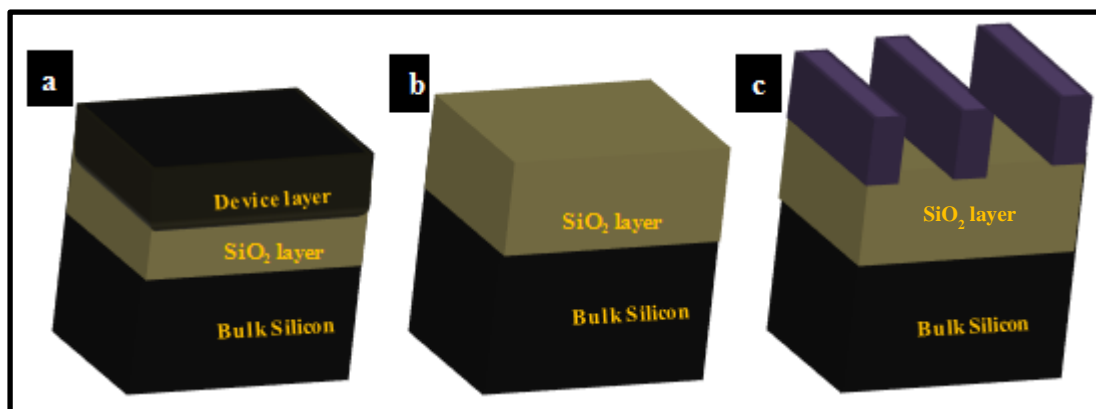
The conventional and modern semiconductor industries utilise metal and semiconductor materials for the transistor devices. Silicon (Si), Germanium (Ge) and Copper (Cu) all play a vital role in the semiconductor industries in determining the performance of a transistor. Silicon is globally available, abundant, stable and a very strong material with the same crystal structure as diamond. The thermal oxidation of silicon forms an excellent oxide (SiO_2) which has an almost perfect great interface with bulk silicon substrate and it has a very low interface-state density ($\sim 10^{10} \text{cm}^{-2} \text{eV}^{-1}$). The deposition of SiO_2 does not produce the excellent interface

that the thermal oxide forms. Also, note that this advantage has less significance for FETs using high- ϵ_r (high k) gate dielectric materials (e.g. HfO_2). On the other hand germanium is potentially an equally important semiconducting material. It can be grown at relatively low temperatures compared to silicon and substantially higher electron and hole mobility suggesting potential for higher-speed devices.

Copper is an important metal in device fabrication especially for use as interconnects and devices. The most important benefit of using copper in integrated circuits is that it offers lower resistivity than aluminium which, historically, has been the dominant interconnect and supercapacitor material [23]. Using a lower resistivity interconnect material such as copper the interconnect resistance-capacitance delay is decreased which, in turn, increases the integrated circuit (IC) speed. The intrinsic speed limit of an integrated circuit is determined by the frequency at which its transistors can be turned ON and OFF. Since smaller transistors have inherently higher clock frequencies, advances in IC speed historically, have been achieved by scaling of feature sizes. Though copper is carefully deposited by thermal and sputtering techniques, due to the high energy of the ions and atoms there is a strong possibility of impurity implantation into the substrates which will lower the device performance. To overcome this issue industry is looking towards the high purity electrochemical deposition of copper.

1.8. Types of substrates

There are four kinds of substrates used in this work to fabricate the nanostructures, conventional bulk silicon, silicon-on-insulator (SOI), silicon dioxide (SiO_2) and lithographically patterned substrates, as shown in **Scheme 1.2**. All these substrates have individual significance in their respective area of study as will be seen later. Silicon substrates have been traditionally used for the CMOS device fabrication. The formation of n-doped and p-doped regions in the surface region result in an electronic channel which current to be gated. The SOI substrates may play an important role in emerging semiconductor industries because the device layer is isolated from the bulk substrate by an insulator layer. This helps in fabricating novel silicon nanowire based devices which are physically and electrically isolated for better electrical performance.



Scheme 1.2. Schematic of different substrates. (a) SOI substrate, (b) SiO₂ substrate and (c) topographically patterned substrate.

SiO₂ substrates are widely used to fabricate metal nanowires using e.g. thermal evaporation technique as discussed in *Chapter 7*. The idea of using an insulating SiO₂ substrate is to allow scientist and fabrication technologists a crystalline bulk substrate while doing any electrical and electrochemical analysis. An example will be seen later in electrochemical sensing.

The nanowires fabricated using BCP lithography might have a range of applications in consumer electronics, medical industries, energy and environment, data storage and sensors. In this thesis, it is reported that the nanowires fabricated using the different BCP systems like PS-*b*-PMMA, PS-*b*-PDMS, have been used as supercapacitor and electrochemical sensor.

The data in the following chapters are organized in the following way. *Chapter 2* centres on pattern formation and control. *Chapters 3 & 4* describe how substrate features may be produced. Chapter 5 describe a process based around a BCP capable of producing very small feature size and other challenges in pattern transfer. *Chapters 6, 7 & 8* demonstrates technological applications. *Chapter 9* provides an overall summary of the work.

1.9. References

- [1] G. E. Moore, In *Proc. SPIE*. **1995**, 2440, 2.
- [2] M. Freebody, *Photonic Spectra* **2011**, 45, 45.
- [3] C.A. Mack, *IEEE Trans. Semicond. Manuf.* **2011**, 24, 202.

- [4] R. F. Pease, S. Y. Chou, *Proc. IEEE*. **2008**, 96, 248.
- [5] S. -J. Jeong, H. -S. Moon, J. Shin, B. H. Kim, D. O. Shin, J. Y. Kim, Y. -H. Lee, J. U. Kim, S. O. Kim, *Nano Lett.* **2010**, 10, 3500.
- [6] R. A. Farrell, T. G. Fitzgerald, D. Borah, J. D. Holmes, M. A. Morris, *J. Mol. Sci.* **2009**, 10, 3671.
- [7] T. Ito, S. Okazaki, *Nature* **2000**, **406**, 1027.
- [8] M. Wissen, N. Bogdanski, S. Moellenbeck, H. C. Scheer, *In Strategies for Hybrid Techniques of UV Lithography and Thermal Nanoimprint* **2008**.
- [9] S. Chung, J. R. Felts, D. Wang, W. P. King, J. J. De Yoreo, *Appl. Phys. Lett.* **2011**, 99, 193101.
- [10] L. Yang, D. H. Lee, H. Y. Chen, C. Y. Chang, S. D. Liu, C. C. Huang, *VLSI Symp. Tech. Dig.* **2004**, 196.
- [11] Z. Li, Y. Chen, X. Li, T. I. Kamins, K. Nauka, R. S. Williams, *Nano Lett.* **2004**, 4, 245.
- [12] Y. Hirai, S. Hafizovic, N. Matsuzuka, J. G. Korvink, O. Tabata, *J. Microelectromech. S.* **2006**, 15, 159.
- [13] D. Borah, M. T. Shaw, S. Rasappa, R. A. Farrell, C. T. O'Mahony, C. M. Faulkner, M. Bosea, P. Gleeson, J. D. Holmes, M. A. Morris, *J. Phys. D: Appl. Phys.* **2011**, 44, 202.
- [14] S. Banerjee, P. Elakkumanan, D. Chidambarao, J. Culp, M. Orshansky, *Proc. SPIE*. **2008**, 6925, 59250K.
- [15] I. W. Hamley, *Angew. Chem. Int. Edit.* **2003**, 42, 1692.
- [16] G. Riess, *Prog. Polym. Sci.* **2003**, 28, 1107.
- [17] B. C. Garcia, M. Kamperman, R. Ulrich, A. Jain, S. M. Gruner, U. Wiesner, *Chem. Mater.* **2009**, 21, 5397.
- [18] S. Rasappa, D. Borah, R. Senthamaraiannan, C. C. Faulkner, M. T. Shaw, P. Gleeson, J. D. Holmes, M. A. Morris, *Thin Solid Films* **2012**, 522, 318.
- [19] R. A. Farrell, N. Petkov, M. T. Shaw, V. Djara, J. D. Holmes, M. A. Morris, *Macromolecules* **2010**, 43, 8651.
- [20] P. Mansky, Y. Liu, E. Huang, T. P. Russell, C. Hawker, *Science* **1997**, 275, 1458.

[21] D. Borah, S. Rasappa, R. Senthamaraikannan, B. Kosmala, M. T. Shaw, J. D. Holmes, M. A. Morris, *ACS Appl. Mater. Interfaces* **2013**, 5, 88.

[22] D. Borah, S. Rassapa, M. T. Shaw, R. G. Hobbs, N. Petkov, M. Schmidt, J. D. Holmes, M. A. Morris, *J. Mater. Chem. C* **2013**, 1, 1192.

[23] B. E. Conway, *Electrochemical Supercapacitors: Scientific Fundamentals and Technological Applications* (Kluwer) **1999**.

2.1. Abstract

The use of hydroxyl-terminated random copolymer brushes (polystyrene-*r*-polymethylmethacrylate, HO-PS-*r*-PMMA) to ‘neutralise’ substrate surfaces and obtain perpendicular orientation of the microphase separated lamellae in symmetric PS-*b*-PMMA block copolymers (BCPs) is well known. However, less well known is how the brushes interact with both the substrate and the BCP and how this might change during thermal processing. A detailed study of changes in these films for different brush and diblock PS-*b*-PMMA molecular weights is reported in this chapter. In general, self-assembly and pattern formation is altered little and a range of brush molecular weights are seen to be effective. However, on extended anneal times the microphase separated films can undergo dimension changes and loss of order. This process is not related to any complex microphase separation dynamics but rather a degradation of methacrylate components in the film. The data suggest that care must be taken in interpretation of structural changes in these systems as the degradation of materials in these systems has been seldom reported.

2.2. Introduction

Block copolymer lithography based on microphase separation in thin films offers promise for the fabrication of nanopatterns of sub-20 nm scale features and has the potential to integrate into existing manufacturing processes [1]. Block copolymer (BCP) nanolithographic methods find industrial applications in the fabrication of nanowires [2], magnetic storage devices [3], nanoporous membranes [4], etc. Excellent control over pattern dimension and structure can be achieved in block copolymer systems through variation of the molecular weight (N), relative volume fraction (ϕ) and the segmental interaction parameter (χ) and a number of different morphological structures *viz.*, lamellar, cylindrical, spherical, gyroid, etc. [5, 6] can all be formed.

However, the use of BCP methods are a challenge because the interfacial interactions of the polymer blocks with the substrate and the environment influence pattern formation and as a result pattern orientation can be a challenge [7, 8]. In cylinder or lamellae forming BCP systems the microdomain orientation can be either parallel or vertical to the substrate surface plane depending on preferential interface

interactions or surface energy effects [9-11]. Very frequently, a perpendicular domain orientation in a thin film is desirable [12-14] for them to be used as effective templates or masks for substrate feature development [15, 16]. Literature reveals the use of a host of methods such as solvent annealing [17], thermal annealing [18], electric field application [19], homopolymer blending [14, 20], chemical modification of substrate [21-27], etc., to improve the wetting behaviour and to control the interfacial and surface energies [28, 29].

The concept of attaching random copolymers to a substrate surface as a 'brush' whereby surfaces neutral to both blocks can be created is well established [21]. Molecular grafting of HO-PS-*r*-PMMA to a substrate surface can result in a thin, uniform and non-preferential (i.e. chemically neutral to both blocks) brush layer that enables control of the wetting behaviour and interfacial interactions of the diblock copolymer components and the substrate thereby promoting perpendicular orientation [21]. For effective orientation control, the relative composition of the HO-PS-*r*-PMMA on the substrate is important [23, 25, 30-34].

Whilst authors have optimised the brush composition and molecular weight to properly define pattern orientation, there have been few systematic studies of the effect of the brush molecular weight on pattern control and thermal stability of thin BCP films. Andreozzi *et al.* [35] have studied brush effects on the dimensions and orientation of cylinder forming PS-*b*-PMMA noting strong cylinder diameter changes. Because the system has such relevance to the microelectronics industry as a potential alternative to conventional photolithography [36], it is of considerable interest, however, to understand the interaction and the effect of the polymer brush with the pattern forming BCP. This chapter reports the microdomain orientations of lamella-forming PS-*b*-PMMA of varying molecular weights using various HO-PS-*r*-PMMA brushes. It is demonstrated that brushes are effective over a wide range of molecular weights. However, there is limited and varying stability of the patterns formed because of reactions that occur between the brush, the substrate and BCP systems.

2.3. Materials and methods

2.3.1. Materials

Hydroxy-terminated random copolymers and lamella-forming polymers were purchased from Polymer Source, Inc., Canada and used as-received. Number-average molecular weight (M_n), and polydispersity (M_w/M_n) of the polymers are listed in **Table 2.1**. The BCPs are indicated as e.g. DB74 and the brushes as e.g. PB1 as shown in **Table 2.1** for brevity in the rest of this paper. The silicon substrates

Table 2.1. Characteristics of hydroxyl-terminated random copolymers and diblock copolymers composed of styrene and methylmethacrylate used for present study.

M_n / g mol ⁻¹	Designation	Polydispersity index, M_w/M_n	PS mole fraction, %
11,000	PB1	1.28	0.55
8,600	PB2	1.25	0.58
13,200	PB3	1.35	0.58
9,700	PB4	1.45	0.60
36,000	DB36	1.07	0.46
74,000	DB74	1.07	0.49
104,000	DB104	1.09	0.49
176,000	DB176	1.12	0.47

used were reclaimed 8" <100> orientated silicon wafers. The substrates had a native oxide layer of ~2 nm (by transmission electron microscopy). Sulfuric acid, hydrogen peroxide and toluene were purchased from Sigma-Aldrich and used without further purification unless otherwise stated. Deionised water was always used.

2.3.2. Preparation of anchored brush substrates

Prior to film casting, silicon substrates were laser diced into 2.0 cm² pieces and cleaned in a piranha solution (1:3 v/v 30% H₂O₂:H₂SO₄ - **CAUTION! May cause explosion in contact with organic material!**) at 90 °C for 60 min, rinsed with deionized water, and dried under N₂ flow. The contact angle data of as received

silicon and piranha cleaned silicon substrates (**Table 2.2**) show the significantly more hydrophilic nature of the acid cleaned surface consistent with an increased surface concentration of silanol groups. This step is key to producing effective brush layers. Hydroxy-terminated random copolymer brush solutions of 1.0 wt % in toluene were spin-coated onto silicon wafers at 3000 rpm for 30 s. Samples were annealed in a vacuum oven (Townson & Mercer EV018) at 170 °C under vacuum (~ 1 bar) for periods of 3-48 h (*see text for details*). This allows the end-functional hydroxyl groups of the random copolymers to react with substrate silanol groups and so provide effective chemical anchoring of the brush preventing removal on solvent exposure etc. Unbound polymers were removed by sonication (Cole-Palmer 8891 sonicator) and rinsing in toluene.

2.3.3. Deposition of the diblock copolymer and pattern formation

PS-*b*-PMMA solutions of 1.0 wt % in toluene were spin-coated onto the anchored brush at 3200 rpm for 30 s. Samples were annealed at 180 °C under vacuum (~ 1.0 bar) for 3-24 h (*see text for details*) to induce phase separation and remove solvent. The films were removed from the oven immediately after annealing. The film thickness developed was around 45 \pm 3 nm and largely invariant of the BCP molecular weight.

2.3.5. Characterisation

2.3.5.1. Contact angle measurements

Water contact angles were measured using a Data Physics Contact Angle (model: OCA15) tool. Contact angles were measured on the opposite edges of at least three drops and averaged. The values were reproducible to within 2.0°.

2.3.5.2. Film thickness measurements

Polymer film thickness was determined by ellipsometry (Plasmos SD2000 Ellipsometer). An average of three readings collected from different locations on a sample surface was reported as the film thickness result.

2.3.5.3. Atomic Force Microscope (AFM)

Direct polymer film imaging was carried out on an Atomic Force Microscope (DME 2452 DualScope Scanner DS AFM) operating in AC (tapping) mode under ambient conditions using silicon microcantilever probe tips with a force constant of 60,000 N m⁻¹ and a scanning force of 0.11 nN. Topographic and phase

images were recorded simultaneously. Fast Fourier Transforms (FFTs) of the topographic images was used to measure the degree of alignment and the presence of defects/non-regular patterns.

Table 2.2. Water contact angle and film thickness (ellipsometry) of hydroxyl-terminated random copolymers and diblock copolymer films on silicon substrates. Polymer concentration was 1.0 wt % in all cases. Before and after in the deposition column indicate prior to and after the anneal schedule, respectively.

Material	Deposition condition	Contact angle /°	Thickness /nm
Si substrate	as received	44.7±2	
Si substrate	piranha	29.5±2	
PB1	annealed/cleaned	78.9±2	5.17
PB2	annealed/cleaned	83.7±2	4.62
PB3	annealed/cleaned	83.2±2	5.75
PB4	annealed/cleaned	85.8±2	4.83
DB36	PB3 + DB36 (before)		41.1
	PB3 + DB36 (after)		44.3
DB74	PB3 + DB74 (before)		43.3
	PB3 + DB74(after)		45.5
DB104	PB3 + DB104 (before)		42.6
	PB3 + DB104 (after)		45.2
DB176	PB3 + DB176 (before)		44.7
	PB3 + DB176 (after)		47.8

2.3.5.4. FTIR measurements

A Nicolet Impact 6700 Fourier transform infrared (FTIR) spectrometer was used to verify the presence of oxygen containing (e.g., hydroxyl, carbonyl, etc.) functional groups in PS-*b*-PMMA. Samples for FTIR analysis were prepared under identical anneal conditions used for the diblock copolymer film. The measurements were carried out in the spectral range of 4000-400 cm⁻¹, with a resolution of 4 cm⁻¹ and 32 scans.

2.3.5.5. X-ray photoelectron spectroscopy (XPS)

XPS measurements were performed on Vacuum Science Workshop CLASS100 high performance hemispherical analyser using an Al K α (h ν = 1486.6 eV) x-ray source. Spectra were obtained at a take-off angle of 15 $^{\circ}$ (to the plane of the surface) to achieve good surface sensitivity.

2.3.5.6. Thermal gravimetric analysis (TGA)

TGA analysis was made using a METTLER TOLEDO TGA/DSC 1 STAR $^{\circ}$ System analyzer to investigate the degradation behaviour of both PS-*r*-PMMA and PS-*b*-PMMA under inert conditions. The samples (8-10 mg) were heated from 25 to 600 $^{\circ}$ C at a ramp rate of 10 $^{\circ}$ C min $^{-1}$ in platinum pans under a nitrogen atmosphere.

2.3.5.7. Scanning electron microscope (SEM)

Top-down and cross-sectional images of the PMMA etched samples were obtained by a high resolution (< 1 nm) Field Emission Zeiss Ultra Plus Scanning Electron Microscope (SEM) with a Gemini $^{\circ}$ column operating at an accelerating voltage of 5 kV.

2.3.5.8. Focused ion beam (FIB) and transmission electron microscope (TEM)

An FEI Strata 235-Focused Ion Beam (FIB) tool with resolution up to 10 nm and the SEM were used to image the cross-sectional samples. Platinum was e-beam deposited above the patterns followed by the ion-beam platinum deposition. The TEM lamella specimen were prepared by the Zeiss Auriga-Focused Ion Beam (FIB) with Cobra ion column having a unique 2.5 nm resolution and were analysed by FEI Titan-Transmission Electron Microscope operating at an accelerating voltage of 130 kV to obtain cross-sectional images.

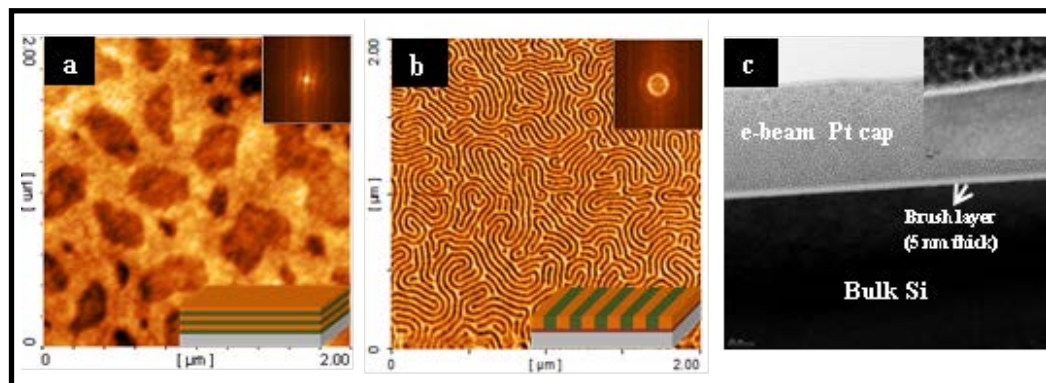
2.4. Results and discussions

2.4.1. Effect of polymer brush on BCP pattern formation

No ordered microphase separated features are observed following vacuum annealing for periods of 3 to 48 h in the absence of a brush layer. A typical image showing an island type structure is shown in **Figure 2.1(a)** for the DB74 BCP. The corresponding FFT image in **Figure 2.1(a) (inset)** is also featureless. The AFM shows significant surface roughness due, presumably, to poor film wetting characteristics. Since, these conditions do affect microphase separation, it is suggested that the film exists such that alternating PMMA and PS domains exist with

a parallel (to the surface plane). This might be expected because PMMA has greater affinity to the substrate surface because of the polar nature of the methacrylate moiety. The proposed structure is shown as a schematic in **Figure 2.1(a)**. Using a

Figure 2.1. 2D Tapping mode AFM topography images of DB74 deposited and annealed at 180



$^{\circ}\text{C}$ for 3 h on (a) bare and (b) PB3 polymer brush anchored substrates and annealed ($170^{\circ}\text{C}/6\text{ h}$). TEM cross-section image of the same brush layer is in **Figure 2.1(c)**. The inset is the TEM cross-section image of bare silicon substrate. The cartons inset in **Figures 2.1(a)** and **(b)** show the proposed lamella orientation in thin films. The PS (green) and PMMA (orange) microphase separate to form PS and PMMA lamellae. In the inset of **Figure 2.1(b)** the brush layer is also indicated.

substrate with a pre-deposited brush layer (PB3), the same polymer (DB74) and the same processing conditions yield a BCP microphase separated, nanoscale, striped (fingerprint) pattern (**Figure 2.1(b)** and **schematic**) with the lamellae oriented perpendicular to the surface plane (note we have shown that these patterns extend throughout the material and extends towards the substrate surface as discussed in **Chapter 3**. The FFT of the image in **Figure 2.1(b)** (**inset**), displays a ring structure indicating the random arrangement of the lamellae. The lamellae repeat distance or pitch (λ_L) is 42 nm as determined from the FFT as shown in **Figure 2.1(b)**. Note that for this BCP, the film thickness is very close to the λ_L value and this is optimum for vertical alignment of the lamellae [30-34]. However, it is clear that the most important effect is the ‘neutralisation’ of the surface by the brush.

2.4.2. Characterisation of the brush layer

It should be noted that the surface-preparation and brush adhesion processes are important in controlling the coverage and the thickness regularity of the BCP. The brushes investigated here were extremely uniform with close to 100% coverage

and AFM and SEM images (not shown) are invariant across large areas of substrate. For all systems, the AFM derived root-mean-square roughness of the brush films was in the range of 0.11-0.17 Å which is similar to literature values [25]. A typical TEM cross-section image of a PB2 layer is described in **Figure 2.1(c)** and this was typical of all the systems studied. The TEM image gives a brush layer thickness of ~5 nm (in reasonable agreement with an ellipsometry derived value of 5.17 nm) and this is consistent with an estimate of around 7 nm using a random coil assumption so that the random coil dimension, $\langle h^2 \rangle_0 = \text{molecular weight} * 0.425$ which is typical for these polymers [37]. The measured value might be a little lower than that estimated since some polymer strain/relaxation in the thin film is expected. The data, therefore, suggest that a layer of attached brush layers extend across the substrate following deposition. It should be noted that the brush layer showed no indication of any spectroscopic or structural changes on even the most extended heating periods (180 °C for 48 h).

The thicknesses of all the brush layers were measured by ellipsometry and are summarized in **Table 2.2**. As expected, the measured thickness scales with molecular weight. The variation in the thickness with molecular weight is consistent with formula given above suggesting the brush as a slightly compressed random coil structure. As might also be expected, the change in relative composition of PS: PMMA in the materials does have some effect on surface properties. This is seen in measurements of water contact angles (**Table 2.2**). The values of the contact angle increase as the relative fraction of PS increases and PS is more hydrophobic than PMMA, the trend is as expected [21].

2.4.3. Variation of the brush and effects on pattern formation

The four different brushes were investigated to assess any changes in structure, orientation, feature size, pattern persistence length and possible wetting-layer formation as well as the alignment direction. **Figure 2.2** shows the AFM topography (FFT data shown as insets) images of DB74 films developed on the various brush modified surfaces illustrating data for various properties of the brushes. In each case the total (BCP and brush) film thickness was ~45 nm thick. There is a small variation in thicknesses observed but this is likely to be due to experimental error in measurement and irreproducibility of the coating process. It

should be noted that all films show a slight expansion following annealing of the BCP. Typical data are reported in **Table 2.2** but all brushes and BCPs showed a

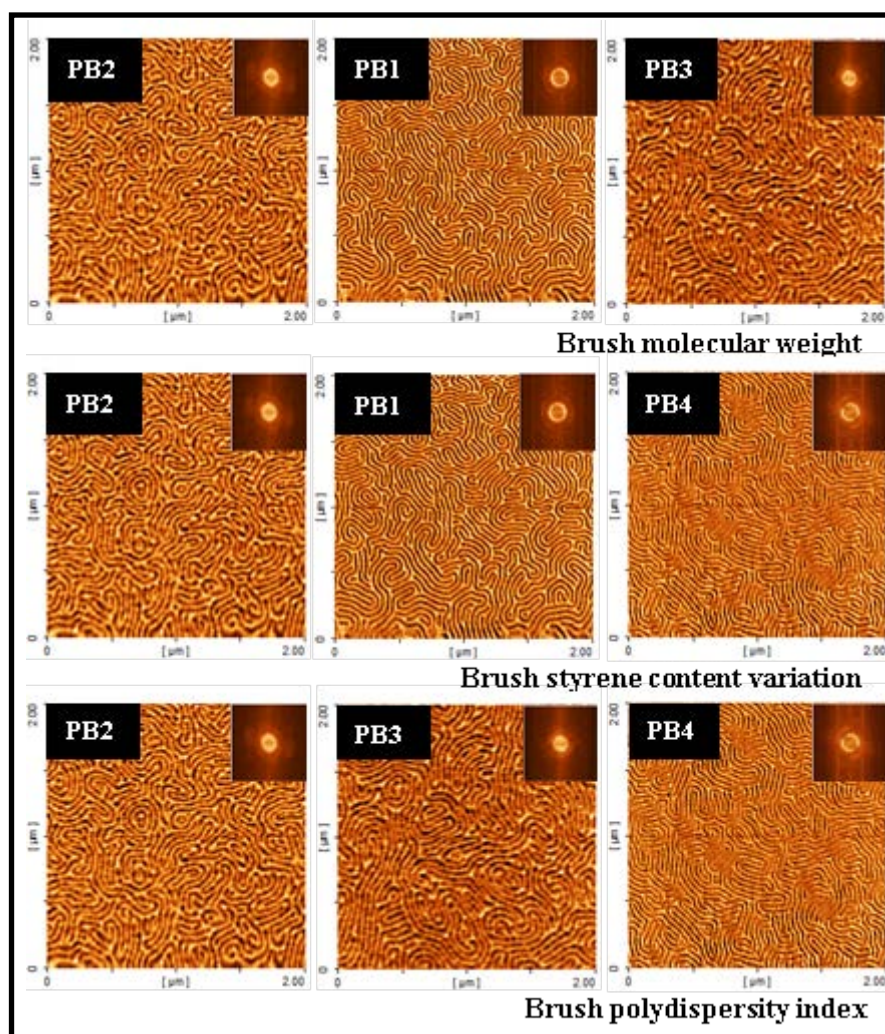


Figure 2.2. 2D Tapping mode AFM topography images of PS-*b*-PMMA thin films of DB74 (BCP was annealed at 180 °C for 3 h) in toluene deposited on various polymer brushes (all annealed at 170 °C for 6 h).

similar expansion of around 2-3 nm. We suggest that this expansion comes from changing inter-penetration of random and block copolymer chains. Before microphase separation there is little energetic difference between mixed and unmixed chains and, hence, there is an effective repulsion between the two types of polymer at their interface. This repulsion is likely to be manifest as increased free volume similar to that when different materials are introduced into a polymer matrix [38]. Free volume may also be created at the interface of the microphase separated

domains. It is this additional free volume that causes the film expansion observed on annealing. However, following microphase separation, the free energy difference between inter-penetration and no inter-penetration of the chains is significantly increased.

From the data in **Figure 2.2**, it is apparent that the patterns observed are largely independent of the brush properties and a similar ‘fingerprint’ pattern is observed in each case. There is no change in orientation of the BCP structure, consistent with data provided by Mansky *et al.* [39] who reported that HO-PS-*r*-PMMA brushes having of PS fraction between 0.50 and 0.65 conferred perpendicular orientation of lamellae. The quality of the image is different in each case but this is most probably due to different tip characteristics rather than any change in film structure, etc. SEM image data as described below support this suggestion. The FFT data are also similar and the ring like structure indicates the random alignment of the microphase separated structure. Similar consistency in the patterns formed was also seen for all the BCPs investigated and data are not reproduced for brevity. The molecular weight range of 8.6-13.2 kg mol⁻¹ had no measurable effect on the λ_L value in sharp contrast with the work Andreozzi *et al.* [35] in using similar brushes and a cylinder forming PS-*b*-PMMA. This may simply reflect the fact that vertically orientated cylinder forming systems would be under some interfacial strain because the brush composition is not ideally matched to the composition of the BCP at the interface.

2.4.4. Effect of brush anneal time on pattern formation

Variations in the length of the brush anneal (170 °C) time (from 6-48 h) were studied. Typical data are shown in **Figure 2.3** for PB3 but note that all brushes gave similar results. The DB74 BCP was deposited onto each brush modified substrate and annealed at 180 °C for 6 h in each case. All the systems produced very similar fingerprint patterns in each case (no significant change in repeat distance could be determined). Essentially similar data (not shown for brevity) were recorded when the brush anneal temperature was increased to 180 °C and the period of anneal varied in the same way. The similarity of results suggests that the brushes are largely

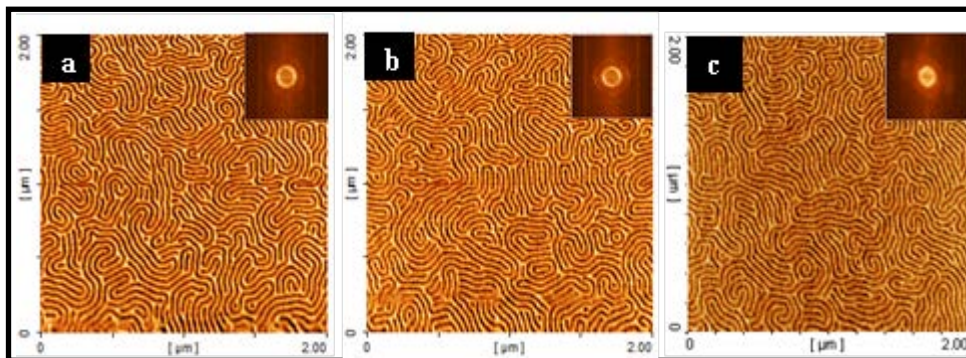


Figure 2.3. 2D Tapping mode AFM topography images of DB74 microphase separated films after annealing at 180 °C for 3 h) deposited on PB3 polymer brush layers. The polymer brush was annealed at 170 °C for (a) 6 h, (b) 24 h, and (c) 48 h.

unaffected by the thermal treatment and close to their thermodynamic equilibrium. There is no indication of polymer degradation and for convenience, a brush anneal time of 6 h was chosen as optimum.

2.4.5. Effect of BCP anneal time and molecular weight on pattern formation

Whilst, varying the time of the brush anneal period seemed to have little effect on the microphase separation of the diblock, variations were observed when the BCP anneal time was varied and a strong molecular weight effect was observed. The four diblock copolymer *viz.*, DB36, DB74, DB104 and DB176 were deposited on PB3 (following a 6 h 170 °C anneal) modified substrates and annealed for various period of 3-24 h at 180 °C. The BCP molecular weights used represent a range where reasonable microphase separation was observed. Outside this range, either none or poor pattern formation was observed. As expected the domain spacing increases with molecular weight as seen in **Table 2.3**. The effect of annealing on the BCP pattern dimensions can be seen directly by measurement of pitch sizes. **Figure 2.4** describes a series of AFM images as a function of anneal time and the measured pitch sizes are shown explicitly in **Table 2.3**. Generally, all the BCP patterns showed degradation in quality as the heating time increased. Qualitatively, the 3 and 6 h data were similar before marked changes occurred at 12 and 24 h. The changes in the images noted above are confirmed by the AFM derived pitch size (lamellar spacing) as given in **Table 2.3**. In all cases, there is a small expansion noted between 3 and 6 h. This increase is more marked at the 12 h heating period and can be clearly seen in the

images. For the two lowest molecular weight systems (DB36, DB74), heating for a period of 24 h results in an obvious reduction of the pitch size.

Table 2.3. Pitch and PS width of nanoscale PS templates developed by selective PMMA etch of self-assembled patterns of diblock copolymer films annealed at different times.

BCP	Anneal time/h	Pitch from AFM/h
DB36	3	23.0
	6	24.5
	12	25.8
	24	25.2
DB74	3	42.0
	6	43.4
	12	44.6
	24	43.9
DB104	3	54.0
	6	55.6
	12	59.9
	24	-
DB176	3	68.0
	6	68.1
	12	70.2
	24	-

For the higher molecular weight BCPs (DB102, DB176), the longest heating periods show complete loss of pattern. It is tempting to think that the pattern degradation is

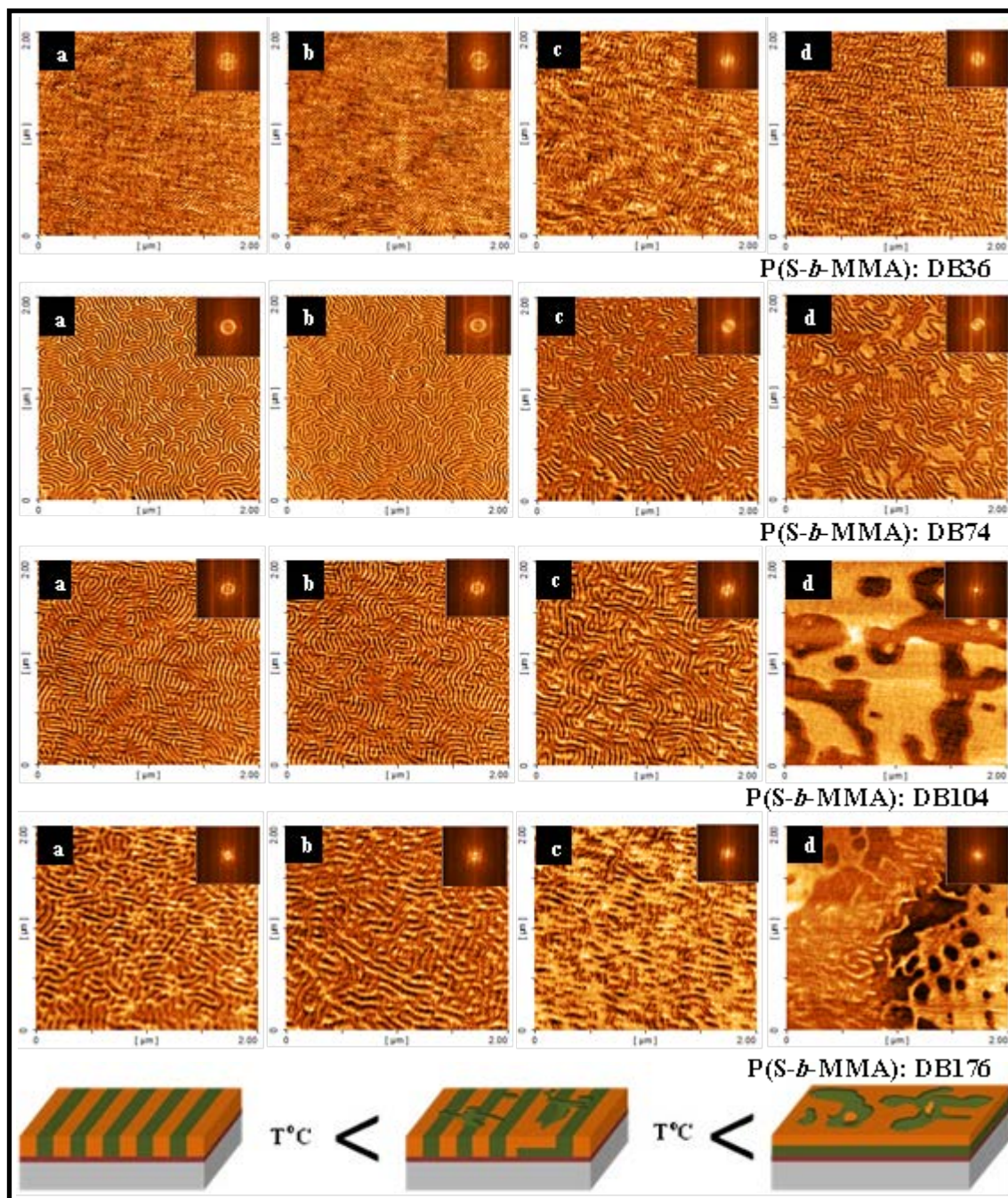


Figure 2.4. 2D Tapping mode AFM topography images of BCP films of various molecular weight (DB36, DB74, DB104 and DB176) in toluene deposited on PB3 polymer brush layer. The brush layer was annealed at 170 °C for 6 h whilst the BCP film was anchored annealed at 180 °C for (a) 3 h, (b) 6 h, (c) 12 h and (d) 24 h. The cartoons in **Figure 2.4** (below) show the proposed effect of increasing anneal time (left to right) on pattern formation: PS (green) and PMMA (orange).

occurring via brush failure and adsorption into the diblock film (causing expansion and eventual pattern loss). However, the data given above suggest that the brush is stable at the substrate surface for annealing periods of up to 48 h. In order to provide explanation detailed spectroscopic measurements were made.

2.4.6. FTIR, XPS and TGA analysis of the BCPs

Detailed investigation of the effects of annealing was carried out on the DB74 diblock polymer and the PB3 brush and data are reported here but note that other systems gave similar results. Typical FTIR data are shown in **Figure 2.5**. **Figure 2.5(a)** shows data from 500 to 4000 cm^{-1} and bands that are associated with both the polymer film and the substrate (marked in figure) can be observed. A doublet can be seen in **Figure 2.5(a)** for all samples at around 2855 and 2920 cm^{-1} which can be assigned to CH_2 and CH_3 stretches respectively. Typical data (sample annealed for 6 h) are shown as the inset to **Figure 2.5(a)**. Since these non-functional groups are unlikely to change significantly during thermal annealing, the peak area of these combined peaks is used to normalise the spectral intensity of the data sets. **Figure 2.5(b)** shows the most interesting part of the spectral range revealing peaks at 1105, 1445 and 1735 cm^{-1} which can be assigned to C-O-C stretch, C- CH_3 deformation and the carbonyl (C=O) stretch respectively and is consistent with previous work [40]. Note the decrease in signals of these PMMA related features during the longest annealing periods suggesting the concentration of PMMA within the analyte is decreasing on annealing for extended times.

Relative changes in the peak area intensity of the PMMA derived features (after normalisation to the CH_2 and CH_3 stretches) suggest that there are changes occurring in the BCP composition during the heating periods studied. Whilst the peak area intensity of the C- CH_3 deformation and the C=O stretch relative to the CH_2 and CH_3 stretches does not change within experimental error during annealing, the C-O-C peak shows a decreasing peak intensity relative to the other features with annealing period.

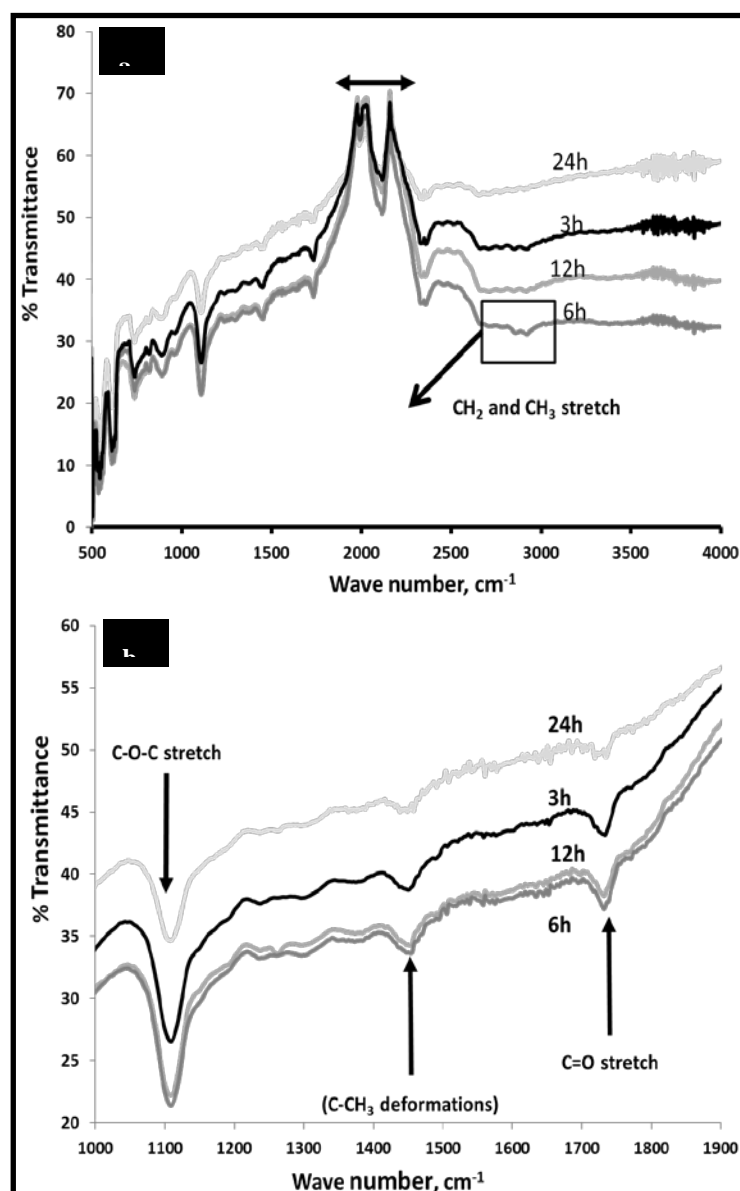


Figure 2.5. FTIR spectra of PS-*b*-PMMA (DB74) on brush (PB3) annealed at 180 °C for different times as shown. (a) and (b) are different spectral regions to show main features as indicated. The insert in (a) shows typical data of the peaks used for normalisation as described in the text.

This is explicitly shown in **Figure 2.5** and suggests that this part of the polymer molecule is undergoing conversion/reaction. Other authors have noted some changes in the FTIR spectra of PMMA films on substrates following heating [41]. These authors noted an increase in a peak at around 842 cm^{-1} and a new feature at 1269 cm^{-1} . They explained this due to the formation of Si-O-CH₃ species (842 cm^{-1}) and the presence of a carboxyl ion (COO⁻) at 1269 cm^{-1} , respectively.

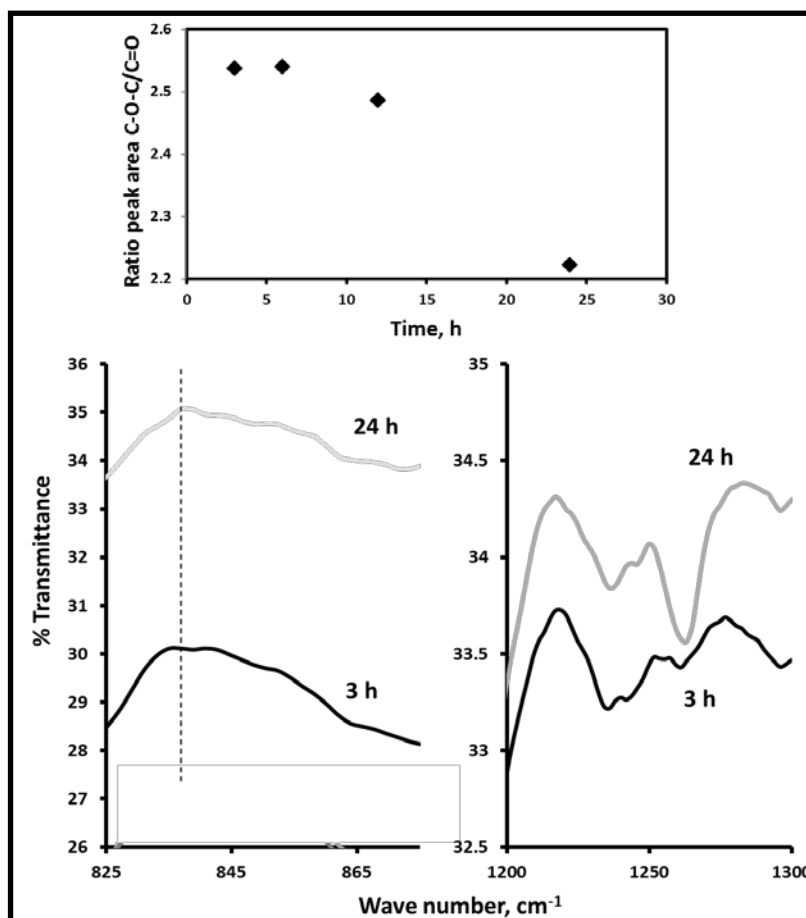


Figure 2.6. Further FTIR data as **Figure 2.5**. Top is quantitative analysis showing the relative decrease of the peak area of -C-O-C and the C=O stretching peak. Bottom left, figure showing the increase in a feature attributable to reaction of PMMA with the substrate as a function of heating period. Bottom right, the development of a band due to presence of formaldehyde type species at these longer heating times.

These changes were related to increased chemical adhesion of the polymer film to the silicon substrate surface. Similar features are observed here following extended heating (data are represented in **Figure 2.6** for materials after 3 and 24 h heating periods). The appearance of the feature at about 1270 cm^{-1} is marked here and suggests O-CH_3 scission of the methacrylate functionality. Unlike Bodas *et al.* [41] we suggest that the feature at 1270 cm^{-1} is probably due to formaldehyde (OCH_2) type species rather than methoxy as this is the frequency associated with CH_2 rocking modes in adsorbed or absorbed states of this molecule [42]. C1s XPS survey spectra of the DB74-PB3 combination following the same heating schedules

are presented in **Figure 2.7(a)** and these data provide strong confirmation of the FTIR data given above. XPS indicates the presence of C and O

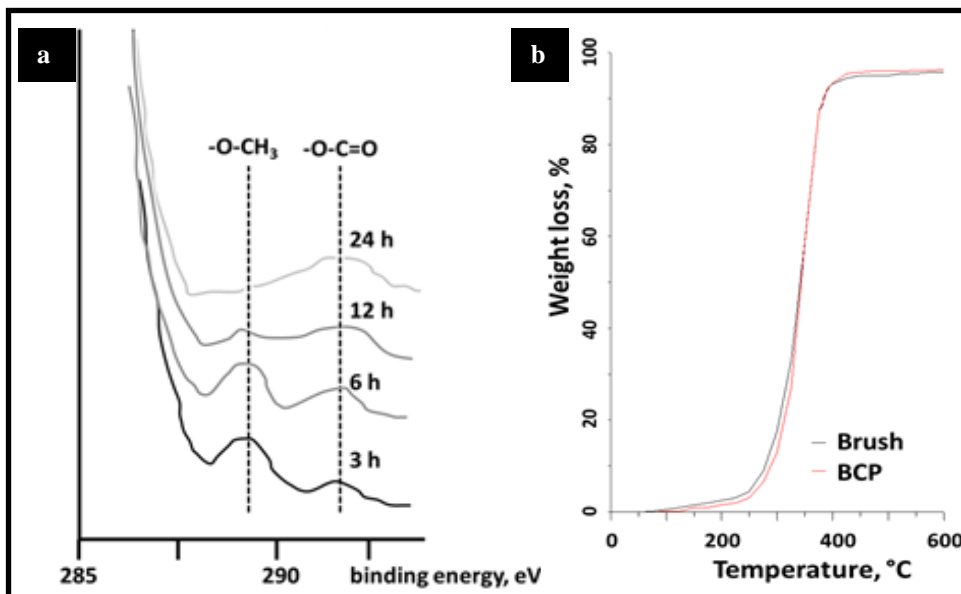


Figure 2.7. (a) C1s XPS spectra of the brush (PB3) and the BCP (DB74) at various heating times at 180 °C (as described in text). (b) TGA data the random copolymer brush (PB3) and diblock copolymer (DB74).

as expected. Although X-rays can catalyse decomposition of PMMA [43], exposure times were minimised and changes during the analysis period were within experimental error. The C1s peak contains three easily resolved features. There is a large feature at ~284.8 eV which can be assigned to aliphatic and aromatic carbon species [44] and further resolution was not possible here since pass energies were high to minimise scan times. Two smaller peaks can also be identified and can be identified [44] as carbon bound to a single oxygen atom (H₃C-O-) at ~289.0 eV and the carbon bound to two oxygen groups within the ester function (O-C=O) at 291.5 eV. On extended heating it can be seen that the H₃C-O- decreases relative to ester related signal and the peak at 291.5 eV appears to increase in peak area as a result of the extended heating. These data are expected from the FTIR analysis since -O-CH₃ bond scission would result in decreased signal at 289.0 eV. Note, however, that XPS suggests that complete loss of this PMMA component is seen not just a relative decrease as noted in the FTIR data. This is because of the XPS is a surface sensitive technique compared to FTIR. The increase in the 291.5 eV peak intensity noted could be due to the formaldehyde formation proposed above since the C1s peak

position is consistent with formaldehyde molecules adsorbed on surfaces [45]. The formation of formaldehyde is known from studies of PMMA thermal degradation [46]. Finally, it should be noted that the PMMA derived C1s signals decrease in intensity - compared to the largely PS derived signal at 284.8 eV - on increased annealing periods (about 60% between 3 and 24 h) suggesting an overall loss of PMMA from the surface region.

This was also noted in the FTIR analysis. The potential for PMMA decomposition at these relatively low temperatures on silica is shown by thermogravimetric analysis of HO-PS-*r*-PMMA (PB3) and PS-*b*-PMMA (DB74). Data are presented in **Figure 2.7(b)**. Rapid pyrolysis begins in the temperature range of 220-340 °C (the only major weight loss step). Both curves are similar within experimental error. It can be seen that decomposition is present at 180 °C and consistent with the changes seen by spectroscopic means.

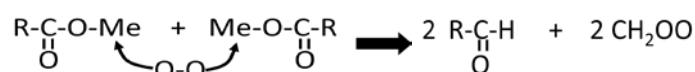
2.4.7. General discussion of the results

These data suggest that great care must be taken in using brushes with block copolymer systems and that complete ‘inertness’ of the system cannot be assumed. With block copolymer systems taking extended periods to reach equilibrium and, hence, achieve the lowest possible defect concentration [47], there is an obvious opportunity for changes in polymer composition and molecular structure to occur. As a result of this work, the work of authors such as Andreozzi *et al.* [35] must be questioned and we suggest that the strain effects observed by these authors may be due to the same degradation observed here.

Whilst the changes observed are clear, it is important to rationalise them in a consistent model. It is obvious that as the polymer degrades, the process is resulting in a change in feature size and domain spacing. Initially, the feature size shows an increase with annealing period before beginning to decrease. In the highest molecular weight system, all signs of microphase separated pattern are lost after extended heating periods. The surface becomes roughened with the appearance of an island structure. It is also clear from a comparison of the XPS and FTIR data that the process begins in the surface region and within the XPS defined analyte depth, the degradation of the PMMA polymer chains is significant. Results suggest that it is the BCP PMMA component that degrades rather than that of the brush.

We suggest the following model to explain these results. The brush is well-anchored to the surface and shows no indication of thermal degradation. TEM and AFM results show the brush layer to be very regular in thickness after even 24 h annealing periods. However, when the microphase separated BCP (on brush) is annealed for periods of 24 h, extensive degradation occurs with the liberation of formaldehyde type species. Since this is not observed in the brush, it is suggested that this occurs because of the presence of a large number of adjacent methacrylate groups.

A possible mechanism might be via oxidation by gas phase oxygen or water molecules:-



Here, R represents the polymer chain and Me the methyl linkage. We further suggest that formaldehyde groups and/or the reactive polymer species formed can react with surface oxygen groups displacing the brush. This type of reaction (and exact details are unknown) would explain both XPS and FTIR changes as well as explaining why the reaction proceeds more quickly at the gas interface. We believe that the increase pitch size seen results from ‘swelling’ of the BCP by displaced brush and by the formaldehyde type units. At the longest period anneals, we think that degradation in the surface regions is close to complete (as suggested by XPS data) and that formaldehyde type species are being desorbed causing pitch size reduction towards more usual values.

We asserted above that for the highest molecular weight systems (DB105 and DB176) that the orientation morphology ‘flipped’ from vertical to horizontal while no flipping is observed for the smaller diblocks (DB36 and DB74). We believe this is the result of sensitivity to thickness of the film. Examining **Table 2.2** and **Table 2.3** it can be seen that for DB105 and B176 that the film thickness is less than the domain spacing (pitch size). This is a non-favourable, thermodynamic arrangement [9-11]. It is only the neutral brush layer that confers vertical alignment and the structure is essentially metastable. On heating for extended periods, the brush is displaced leaving Si-O-CH₃ terminated surfaces which would be non-neutral and favour PS. As a result, the system undergoes rearrangement into a horizontal

orientation. The island structure is formed in order to achieve a minimum thickness of one domain spacing but the volume limitations ensures incomplete surface structure and the observed 'de-wetted' type structure. For diblocks DB36 and DB 74, the film thickness is, or closes to, one and two domain spacings, respectively. This confers additional thermodynamic stability on the vertical orientation and even though the BCP-brush interface changes, the thermodynamic driving force for structural inversion is not so great.

2.5. Conclusions

In conclusion, PS-*b*-PMMA block copolymers show some sensitivity to the brush used when the system is annealed for extended periods. This is not related to complex energetics, but rather due to degradation of the block copolymer. The degradation is manifest in gross change in lamellae orientation when the thickness of the BCP films is less than the domain spacing. All BCPs are swollen by the products of the degradation reaction and pitch sizes change during the annealing cycles. This sensitivity might limit the minimum defect concentration attainable during long annealing cycles.

2.6. References

- [1] C.T. Black, *ACS Nano* **2007**, *1*, 147.
- [2] T. Thurn-Albrecht, J. Schotter, G. A. Kastle, N. Emley, T. Shibauchi, L. Krusin Elbaum, K. Guarini, C. T. Black, M. T. Tuominen, T. P. Russell, *Science* **2000**, *290*, 2126.
- [3] T. Thurn-Albrecht, R. Steiner, J. DeRouchey, C. M. Stafford, E. Huang, M. Bal, M. Tuominen, C. J. Hawker, T. P. Russell, *Adv. Mater.* **2000**, *12*, 787.
- [4] S. Y. Yang, I. Ryu, H. Y. Kim, J. K. Kim, S. K. Jang, T. P. Russell, *Adv. Mater.* **2006**, *18*, 709.
- [5] G. Holden, N. R. Legge, H. E. Schroeder, R. P. Quirk, *Thermoplastic Elastomers*, Hanser: New York, **1987**.
- [6] I. W. Hamley, *The Physics of Block Copolymers*, Oxford University Press: New York, **1998**.

- [7] C. Singh, G. T. Pickett, E. Zhulina, A. C. Balazs, *J. Phys. Chem. B* **1997**, *101*, 10614.
- [8] M. J. Fasolka, P. Banerjee, A. M. Mayes, G. Pickett, A. C. Balazs, *Macromolecules* **2000**, *33*, 5702.
- [9] T. P. Russell, G. Coulon, V. R. Deline, D. C. Miller, *Macromolecules* **1989**, *22*, 4600.
- [10] G. T. Pickett, A. C. Balazs, *Macromolecules* **1997**, *30*, 3097.
- [11] V. Khanna, E. W. Cochran, A. Hexemer, G. E. Stein, G. H. Fredrickson, E. J. Kramer, X. Li, J. Wang, S. F. Hahn, *Macromolecules* **2006**, *39*, 9346.
- [12] U. Jeong, D. Y. Ryu, D. H. Kho, J. K. Kim, J. T. Goldbach, D. H. Kim, T. P. Russell, *Adv. Mater.* **2004**, *16*, 533.
- [13] H. Wang, A. B. Djurisic, M. H. Xie, W. K. Chan, O. Kutsay, *Thin Solid Films* **2005**, *488*, 329.
- [14] H. Kitano, S. Akasaka, T. Inoue, F. Chen, M. Takenaka, H. Hasegawa, H. Yoshida, H. Nagano, *Langmuir* **2007**, *23*, 6404.
- [15] E. Huang, L. Rockford, T. P. Russell, C. J. Hawker, *Nature* **1998**, *395*, 757.
- [16] S. O. Kim, H. H. Solak, M. P. Stoykovich, N. J. Ferrier, J. J. de Pablo, P. F. Nealey, *Nature* **2003**, *424*, 411.
- [17] J. Bang, S. H. Kim, E. Drockenmuller, M. J. Misner, T. P. Russell, C. J. Hawker, *J. Am. Chem. Soc.* **2006**, *128*, 7622.
- [18] E. Han, M. Leolukman, M. Kim, P. Gopalan, *ACS Nano* **2010**, *4*, 6527.
- [19] T. L. Morkved, M. Lu, A. M. Urbas, E. E. Ehrichs, H. M. Jaeger, P. Mansky, T. P. Russell, *Science* **1996**, *273*, 931.
- [20] F. Chen, S. Akasaka, T. Inoue, M. Takenaka, H. Hasegawa, H. Yoshida, *Macromol. Rapid Commun.* **2007**, *28*, 2137.
- [21] P. Mansky, Y. Liu, E. Huang, T. P. Russell, C. Hawker, *Science* **1997**, *275*, 1458.
- [22] R. D. Peters, X. M. Yang, T. K. Kim, P. F. Nealey, *Langmuir* **2000**, *16*, 9620.
- [23] D. Y. Ryu, K. Shin, E. Drockenmuller, C. J. Hawker, T. P. Russell, *Science* **2005**, *308*, 236.

- [24] S. Ludwigs, K. Schmidt, C. M. Stafford, E. J. Amis, M. J. Fasolka, A. Karim, R. Magerle, G. Krausch, *Macromolecules* **2005**, *38*, 1850.
- [25] I. In, Y. H. La, S. M. Park, P. F. Nealey, P. Gopalan, *Langmuir* **2006**, *22*, 7855.
- [26] J. Bang, J. Bae, P. Lowenhielm, C. Spiessberger, S. A. Given-Beck, T. P. Russell, C. J. Hawker, *Adv. Mater.* **2007**, *19*, 4552.
- [27] J. Y. Cheng, C. T. Rettner, D. P. Sanders, H. -C. Kim, W. D. Hinsberg, *Adv. Mater.* **2008**, *20*, 3155.
- [28] C. D. Bain, H. A. Biebuyck, G. M. Whitesides, *Langmuir* **1989**, *5*, 723.
- [29] R. D. Peters, X. M. Yang, T. K. Kim, B. H. Sohn, P. F. Nealey, *Langmuir* **2000**, *16*, 4625.
- [30] E. Han, I. In, S. M. Park, Y. H. La, Y. Wang, P. F. Nealey, P. Gopalan, *Adv. Mater.* **2007**, *19*, 4448.
- [31] D. Y. Ryu, J. Y. Wang, K. A. Lavery, E. Drockenmuller, S. K. Satija, C. J. Hawker, T. P. Russell, *Macromolecules* **2007**, *40*, 4296.
- [32] E. Huang, T. P. Russell, C. Harrison, P. M. Chaikin, R. A. Register, C. J. Hawker, J. Mays, *Macromolecules* **1998**, *31*, 7641.
- [33] S. Ji, C. -C. Liu, J. G. Son, K. Gotrik, S. W. C. Gordon, P. Gopalan, F. J. Himpsel, K. Char, P. F. Nealey, *Macromolecules* **2008**, *41*, 9098.
- [34] E. Han, H. Kang, C. -C. Liu, P. F. Nealey, P. Gopalan, *Adv. Mater.* **2010**, *22*, 4325.
- [35] A. Andreozzi, E. Poliani, G. Sequini, M. Perego, *Nanotech.* **2011**, *22*, 185304.
- [36] R. A. Farrell, T. G. Fitzgerald, D. Borah, J. D. Holmes, M. A. Morris, *J. Mol. Sci.* **2009**, *10*, 3671.
- [37] L. J. Fetters, D. J. Lohse, D. Richter, T. A. Witten, A. Zirkel, *Macromolecules* **1994**, *27*, 4639.
- [38] C. -L. Li, S. -H. Huang, W. -S. Hung, S. -T. Kao, D. -M. Wang, Y. C. Jean, K. -R. Lee, J. -Y. Lai, *J. Membr. Sci.* **2008**, *313*, 68.
- [39] P. Mansky, T. P. Russell, C. J. Hawker, M. Pitsikalis, J. Mays, *Macromolecules* **1997**, *30*, 6810.
- [40] D. Borah, S. Rasappa, R. Senthamaraiakanan, B. Kosmala, M. T. Shaw, J. D. Holmes, M. A. Morris, *ACS Appl. Mater. Interfaces*, **2013**, *5*, 88.

- [41] D. S. Bodas, S. K. Mahapatra, S. A. Gangal, *Sensor. Actuat. A- Phys.* **2005**, *120*, 582.
- [42] V. Lochañ, *Appl. Catal. A- Gen.* **2006**, *309*, 33.
- [43] D. Briggs, *In Surface Analysis of Polymers by XPS and Static SIMS*; D. R. Clarke, S. Suresh, I. M. Ward FRS, Eds., Cambridge University Press: Cambridge, **1998**.
- [44] G. Beamson, D. Briggs, *High Resolution XPS of Organic Polymers*, The Scienta ESCA300 Database, Wiley: Chichester, **1992**.
- [45] H. Bluhm, M. Hävecker, A. Knop-Gericke, E. Kleimenov, R. Schlögl, D. Teschner, V. I. Bukhtiyarov, D. F. Ogletree, M. Salmeron, *J. Phys. Chem. B.* **2004**, *108*, 14340.
- [46] J. Luche, T. Rogaume, F. Richard, E. Guillaume, *Fire Safety J.* **2011**, *46*, 451.
- [47] C. T. O'Mahony, R. A. Farrell, T. Ghoshal, J. D. Holmes, M. A. Morris, *Thermodynamics / Book 4*", ISBN 979-953-307-047-5, InTech Publications: **2011**.

3.1. Abstract

In *chapter 3* we discuss the complete pattern transfer of a BCP template derived from a selective PMMA etch of a PS-*b*-PMMA system to an underlying silicon substrate for nanowire fabrication by plasma etch technology. Scaling has been enabled by varying BCP molecular weights and the most important of the secondary processes is the plasma etch methodology whereby the pattern created by BCP template is ‘transferred’ to the surface via a selective etch to remove exposed material. However, plasma etch technologies face challenges as scaling continues. Maintaining absolute fidelity in pattern transfer at sub-16 nm dimensions will require advances in plasma technology (plasma sources, chamber design, etc) and chemistry (etch gases, flows, interactions with substrates, etc). In this chapter, we illustrate some of these challenges by discussing the formation of ultra-small device structures from the directed self-assembly of block copolymers (BCPs) where nanopatterns are formed from the micro-phase separation of the system. The polymer pattern is transferred by a double etch procedure where one block is selectively removed and the remaining block acts as a resist pattern for silicon pattern transfer. Data are presented which shows that highly regular nanowire patterns of feature size below 20 nm can be created using etch optimization techniques and in this chapter we demonstrate generation of crystalline silicon nanowire arrays with feature sizes below 8 nm. BCP techniques are demonstrated to be applicable from these ultra-small feature sizes to 40 nm dimensions. Etch profiles show rounding effects because etch selectivity in these nanoscale resist patterns is limited and the resist thickness rather low. The nanoscale nature of the topography generated also places high demands on developing new etch processes.

3.2. Introduction

It is true that Moore’s law has driven progress in microelectronics for over 40 years [1]. This scaling not only enables greater device densities and computing power but also decreases power usage and cost [2]. State-of-the-art integrated circuitry has feature sizes of 32 nm with around 1 billion transistors on a single die (chip) [3]. However, the industry is largely product demand driven and the need to

deliver higher performance-in, e.g., medical diagnostics such as MRI and personalized treatment, high-resolution video capture and storage, 3D video demands, improved graphics, data encryption as well as high-density storage will drive the processor industry towards 4 nm feature sizes and possibly less. Scaling has been achieved by photolithography, the process by which light passing through a patterned mask is incident on a photosensitive resist film at a substrate [4]. The incident light either stabilizes or destabilizes the resist (negative and positive tone resists) to a solvent so that by solution the mask pattern or its inverse is created in the resist film. In the simplest form of patterning, the patterned resist is used as an etch mask whilst exposed substrate is controllably removed to transfer the pattern to the substrate. Whilst originally wet chemistries were used as etches, the advantages of plasma etching, where chemically active radicals/ions were used to remove material, led to its exclusive use [5].

The advantages of inductively coupled plasma (ICP) and reactive-ion etching (RIE) methodologies in terms of anisotropy (i.e. etching in vertical direction only with little or no lateral etching), large-area and high-density at relatively low pressures have led to the adaption of these sources in industry [6]. Perhaps the greatest advantage of plasma techniques in modern integrated-circuit (IC) manufacture is the uniformity of the etch process which results in extremely uniform features [7]. Unless the etch is highly controlled, poor sidewall regularity is difficult to avoid. Ever decreasing dimension and the role of line-edge roughness (LER) on device variation [8] will necessitate the development of ever more specific, anisotropic plasma etches (for silicon, silica, gate dielectric and other materials). It is clear that implementing plasma techniques for surface etching will be a challenge as the nature of transistor devices changes. One potential method for extending the current scales achievable by 193 nm photolithography is the double exposure technique where, e.g., features are patterned into resist and a plasma exposure is used to isotropically etch these features to a smaller size [9]. A second application of resist and lithographic exposure then creates a resist pattern between the first set which are also isotropically etched to reduce feature size. A third etch is then used to transfer the resist pattern to a device layer. However, the ITRS clearly points to a

number of solutions to overcoming barriers to ultra-small (<16 nm) feature size [3]. One of these involves the use of directed self-assembly where chemical interactions between moieties results in the spontaneous formation of a regular pattern at a substrate surface. These patterns then act as a resist for transfer to a device layer [3]. This form of chemical patterning will be used to illustrate some of the more interesting challenges facing plasma etch methodologies in the next few years.

3.2.1. Plasma processing for development of nanoelectronics

A plasma is a partially ionized gas containing, ions, radicals and neutrals. The energy to create the plasma is obtained via the coupling of an external magnetic field to the plasma gas. Industrial IC manufacture has been realized by two plasma etching techniques; Reactive Ion Etching (RIE) and Inductively Coupled Plasma (ICP) methods. RIE has been summarized by, e.g., Jansen *et al* [10]. A RIE apparatus consists of a glow-discharge-generated plasma where gas molecules (e.g. SF₆ for silicon etching) are dissociated and ionized to create reactive species. Substrates are placed on a radio frequency (RF)-driven capacitively coupled electrode to generate a DC (Direct Current) bias at the sample. Reactive species, such as fluorine radicals and ions, impinge on the surface creating volatile silicon species. In most practical processes, RIE is actually a combination of the reactive species reactions that are highly species selective and ion bombardment where the reaction is a physical process caused by kinetic energy transfer. Radical etching (or true plasma etching) is limited to neutral radicals and the plasma is normally excited by microwaves. These plasma etches are chemical in nature and can have very high selectivity and impart little damage. They are in essence 'isotropic'. This type of selective etch is used to remove photoresist after pattern transfer. In silicon technologies, selectivity or contrast between the removal rate for the resist and the exposed substrate allows a pattern transfer process to take place generating sharp-edged substrate features with high aspect ratios. As feature sizes decrease, the critical dimension (CD, the regularity of feature size) becomes ever more important because of the need to reproduce devices with similar characteristics [11]. Thus, one of the main challenges will be how to produce topographic features in a substrate with high fidelity and low roughness when mask materials may not be of ideal composition or

thickness (see below for examples). High aspect ratio (depth/feature size) features require ‘anisotropic’ etches and is achieved using plasmas that generate both radicals (i.e. chemical selectivity) and ions (physical removal of substrate species) and is described by the generic term RIE. In RIE, plasma exposure develops a negative charge at the substrate from electrons produced in the plasma. This charge accelerates positive ions towards the surface in a direction normal to the surface plane. This ion bombardment occurs causing accelerated substrate removal as well as roughening the surface to create more reactive surfaces. In order to achieve higher ion bombardment rates the RIE plasmas are characterized by low plasma potentials (<100 V) and high Radio Frequency (RF) biases (>500 V) compared with plasma etching where there is only low sample bias (<10 V).

Sidewalls of features are largely unaffected by the bombardment process and so the sidewalls etch at a much lower rate than the substrate base allowing high aspect ratio features to be generated with vertical sidewalls and little change in resist feature size and spacing [12]. It is important to note that RIE is a true combinatorial technique in that etch rates for RIE are higher than the total etch rate that might be achieved by ion beam and chemical etching separately [13]. Etch directionality in RIE can be achieved in two main ways. The first of these is simple ion-induced RIE where ion modification of the exposed surface leads to enhanced removal [14]. Typical examples are Cl_2 sponsored etching of Si and O_2 etching of polymers. The most common technique in the microelectronics industry is ion-inhibition RIE where the as-created sidewalls are coated with a passive film that resists etching [10]. This film can be created by the use of gases that, e.g., stable non-volatile carbon halogen materials [15], trapping volatile silicon products at the trench walls by cryogenic cooling [16], using gases (e.g. C_4F_8) that form polymeric barrier layers [17] and erosion/re-deposition of mask materials such as metal halogens. Typical examples are chlorine- and bromine-based silicon etches, whilst SF_6 – O_2 -based plasmas can also be used as anisotropic etches. An ever more important issue in RIE is aspect ratio-dependent etching (ARDE) [18, 19]. This has been important in micromachining for some time as high-aspect-ratio features are required. However, as device feature size reduces, this is becoming a general problem in nanocircuitry

generation. Aspect ratio dependent etching (ARDE) describes the loss of fidelity that occurs in small feature sizes where feature width is comparable to or less than the feature depth. ARDE is a result of several issues, e.g. deflection via ion scattering of ions towards the sidewall, diffusion effects in reactants/product reaching/leaving the base of the feature and diverging electric fields in the feature. The ICP technique can achieve much higher etch rates than RIE etching as they can operate at high plasma densities [20]. In comparison with RIE tools where the RF frequency is capacitively coupled to the plasma gas, in an ICP etcher power is input inductively.

ICP etchers have their impedance matched to the plasma and consequently achieve high coupling efficiency between the plasma electrons and the applied field. Further, the plasma is much more controllably contained in ICP tools which further improve efficiency. ICP tools operate at low pressures (<20 mT) and this has important consequences. The general principles of plasma etching described above (such as etch chemistry, etch anisotropy and sidewall modification) for RIE are maintained for ICP systems but there are proven advantages of the ICP technique. The low pressure improves diffusion of reactive species into small features enhancing the rather low etch rates achieved by RIE in very small feature sizes. It also reduces ion scattering and so improves the anisotropy of an etch. There are also distinct disadvantages of the ICP etch process.

The low pressure reduces selectivity of the etch process and so results in mask damage and removal. The use of thick etch masks limits feature depth. For these reasons, combination ICP–RIE etch tools are frequently used to achieve optimum results. The following will describe how very small feature sizes can be achieved at silicon substrates using block copolymer (BCP) nanolithography. The use of BCPs for generating highly regular patterns at surfaces is now well established and has been ear-marked as a possible solution for achieving ultra-small features for silicon and related materials [21, 22]. These systems form ordered patterns by a process of micro-phase separation [21, 22]. However, the need to achieve pattern transfer of the very small features realized by these methods via plasma etching methods is a serious challenge [23].

3. 3. Materials and methods

Self-assembled PS-*b*-PMMA (polystyrene-*b*- polymethyl-methacrylate) BCP patterns are used for nanolithography-pattern transfer of the substrate to silicon substrates. A selective ion etch is used to selectively remove the more reactive PMMA leaving a topographic PS pattern over the silicon surface. The PS is then used as a mask to protect underlying silicon from silicon ICP etch.

3.3.1. Plasma etching

PMMA dry etch removal was performed with an Oxford Instruments OIPT Plasmalab System100 ICP180 etch tool using various oxygen (O₂) and argon (Ar) mixtures at a pressure of 15 mTorr at 20 ° C. For homopolymer etching, both PS and PMMA films were loaded within the same etch sequence to ensure both films were exposed to identical processing. Silicon pattern transfer procedures was achieved using a combination of silicon hexafluoride (SF₆) and trifluoromethane (CHF₃) gases in the ICP-RIE mode at a pressure of 15 mTorr at 10 °C. The flow rates were 80 sccm and 15 sccm for CHF₃ and SF₆, respectively, and the etch time was 9 s at an ICP power of 1200 W and RIE power of 30 W. A third oxygen plasma etch was used to remove residual PS after pattern transfer. This PS strip was centred on a 2000 W ICP etch at a pressure of 10 mT with an O₂ flow of 30 sccm for a time of 10 s.

The etch conditions to provide maximum selectivity to PMMA were found by studies of PS and PMMA homopolymer samples which allowed etch contrast between the blocks to be carefully optimized. The ICP etch uses a combination of oxygen and argon sources since the addition of oxygen dramatically increases the production of argon ions and increasing etch anisotropy whilst enhancing selectivity to the oxygen containing PMMA block. In the ICP etch SF₆ acts as the source of ion and radical fluoride species whilst the CHF₃ forms a polymeric layer at the sidewalls allowing high etch anisotropy and relatively deep feature sizes (i.e. high aspect ratio) to be produced.

3.3.2. BCP polymer development

Symmetric PS-*b*-PMMA copolymers with molecular weights of approximately 85-91, 52-52, 37-37 and 18-18 kg mol⁻¹ (the polymers are indicated as e.g. PS-*b*-PMMA 37k-37k throughout the text in this chapter) and a neutral

polystyrene-*random*-polymethylacrylate (HO-PS-*r*-PMMA) with a PS content of 58% were purchased from Polymersource of Canada. For this study, BCP polymer template development of different molecular weights were examined with random copolymer as discussed in material and methods sections 2.3.1, 2.3.2 and 2.3.3 in *Chapter 2*.

3.3.3. Film characterization

Polymer film thickness was determined by ellipsometry (Plasmos SD2000 Ellipsometer). An average of three readings collected from different locations on a sample surface was reported as the film thickness result.

3.3.4. Scanning electron microscope (SEM)

Top-down and cross-sectional images of the PMMA etched samples were obtained by a high resolution (< 1 nm) Field Emission Zeiss Ultra Plus Scanning Electron Microscope (SEM) with a Gemini[®] column operating at an accelerating voltage of 5 kV.

3.3.5. Focused ion beam (FIB) and transmission electron microscope (TEM)

An FEI Strata 235-Focused Ion Beam (FIB) tool with resolution up to 10 nm and the SEM were used to image the cross-sectional samples. Platinum was e-beam deposited above the patterns followed by the ion-beam platinum deposition. The TEM lamella specimen were prepared using a Zeiss Auriga-Focused Ion Beam (FIB) with Cobra ion column having a unique 2.5 nm resolution and were analysed by an FEI Titan-Transmission Electron Microscope operating at an accelerating voltage of 130 kV to obtain cross-sectional images.

3.4. Results and discussions

As outlined above, to estimate the etch rate of the individual PS and PMMA blocks and, more importantly, to establish the ideal conditions for achieving etch selectivity (etch contrast) between the PS and PMMA blocks, etch rates of homopolymer films were investigated in a similar manner to methods outlined elsewhere [24]. Since PMMA contains an ether linkage and PS is an aromatic hydrocarbon, etch contrast between the two polymers is possible. Using the homopolymer films, the ICP gas flows were adjusted to provide the highest PMMA

etch rates and minimum PS etch rates. Data are provided in **Table 3.1** which shows the process flow for a detailed etch rate detection of PMMA also to measure etch selectivity of PS to PMMA. **Table 3.2** provides the gas flow rates for argon (Ar) and oxygen (O₂) mixtures, homopolymer film thickness, resultant etch rates per minute and PS to PMMA selectivity for a series of ICP etches. We emphasize of course, that these values are provided as a guide for other researchers but it is noted these will generally not be transferable to other equipment as etching is reliant on plasma properties and, hence, experimental configuration, etc and these values represent optimum performance for the apparatus used here.

We do note that gas flow rates did have considerable effect on the etch profile of the nanostructures generated. This is in itself an unusual observation and we suggest this may be related to etch product removal rate variation which is critical in these ultra-small topographies generated. Careful process control through flow rate control allows etch selectivity optimization. It was found that an ICP using Ar/O₂ with the following flow rates of 5 sccm/20 sccm provided a PMMA etch rate of 377.7 nm min⁻¹ but more importantly a reduced etch rate for PS of 123.8 nm min⁻¹ over the same time window. This represented an etch selectivity of PS to

Table 3.1. Taguchi Matrix System for OIPT 100 ICP 180 Plasma lab system for PMMA etch rate detection. Constant parameters- total gas flow Ar+O₂ is 25sccm, Etch time 6 s, Temperature-20°C and He backside 5 Torr.

Run	O ₂ (Sccm)	Pre (mT)	ICP (W)	RIE (W)
1	10	10	200	20
2	10	14	300	40
3	10	18	400	60
4	15	10	300	60
5	15	14	400	20
6	15	18	200	40
7	20	10	400	40
8	20	14	200	60
9	20	18	300	20

PMMA of 3:1 for the PS and PMMA homopolymer films. Using the data shown in **Table 3.2** an optimum etch condition for a selective etch of PMMA was obtained as with the design flow shown in **Table 3.1**. The gas flow rates are then optimised to 15 sccm and 5 sccm for Ar and O₂ gases with an ICP power of 400 W and 40 W RIE power at a temperature 10 °C with 12mT pressure for 6 s. This optimised etch

Table 3.2. Measured data of PS and PMMA film thickness post Ar +O₂ plasma etch at different flow rates of argon+oxygen and PS to PMMA etch selectivity for 2 wt% PS and 4 wt% PMMA homopolymer films after etching.

Run	E _{pmma} nm/min	E _{ps} nm/min	Selectivity S _{ps:pmma}	DC (V)
1	238.3	114.5	2.1	122
2	451.9	242.2	1.9	181
3	607.8	303.9	2	229
4	745.7	272.6	2.7	236
5	384	177.4	2.2	100
6	241.8	86.7	2.8	199
7	679.7	300	2.3	158
8	377.7	123.8	3.1	259
9	198	109.8	1.8	131

condition are applied to the samples imaged in **Chapter 2** as shown in **Figure 2.5** for selective PMMA etch and the corresponding SEM images are shown **Figure 3.1**. Pitch sizes were measured by both AFM as shown in **Chapter 2** and SEM in **Figure 3.1** (following PMMA removal) to ensure accuracy and were in reasonable agreement. The AFM data were used for comparison because it was believed that the FFT used to derive the information gave a better average value than SEM and this was important because there was considerable lateral variation in the patterns on extended heating. Generally, all the BCPs showed degradation in the AFM image quality as shown in **Figure 2.5** as the heating time increased. Qualitatively, the 3 and 6 h data were similar before marked changes occurred at 12 and 24 h. The SEM data

in **Figure 3.1** were slightly different showing reasonable quality images from 3 to 12 h and only data at 24 h heating periods showed very significant changes in pattern quality. Both techniques showed complete loss of microphase separated patterns at

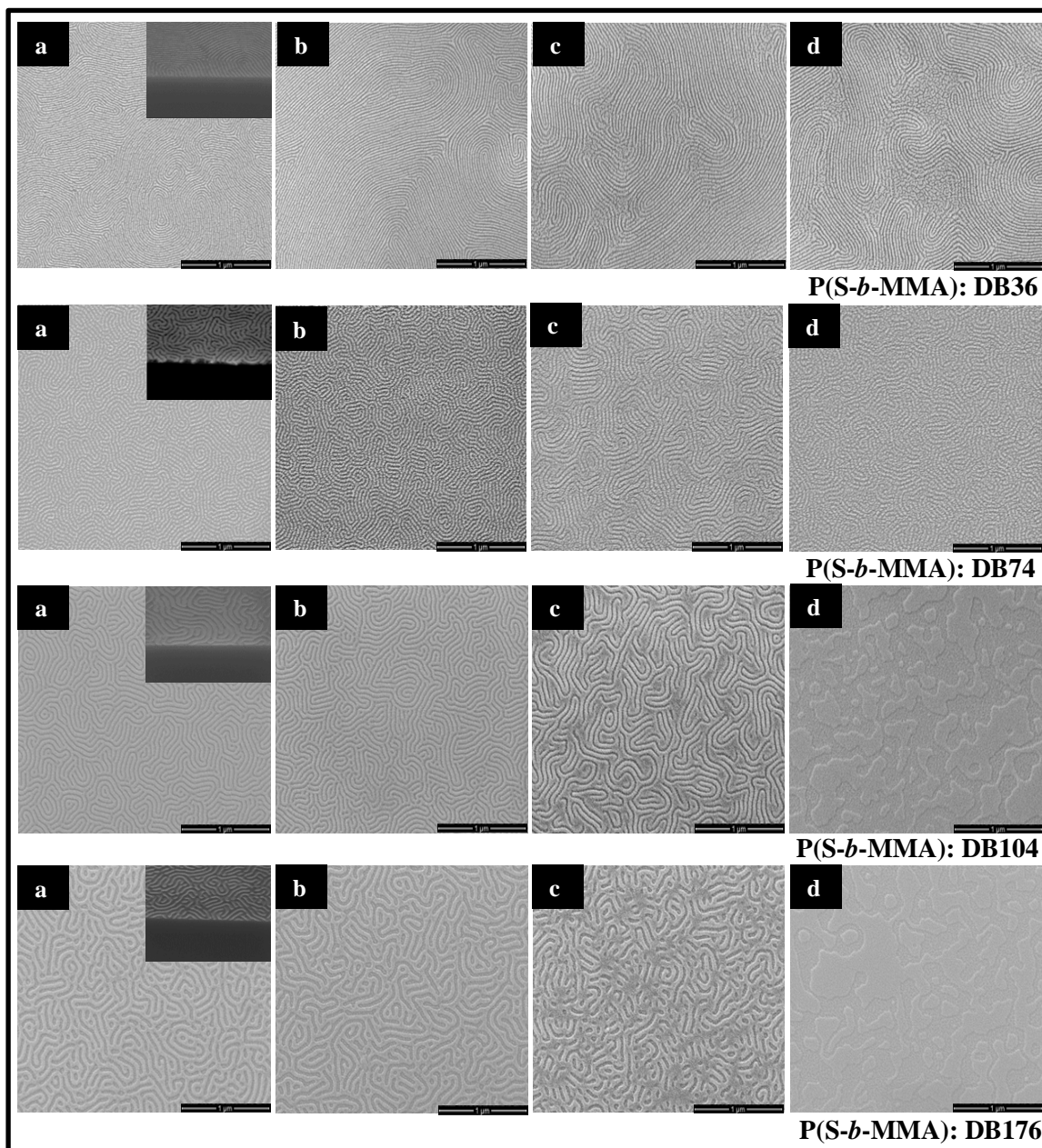


Figure 3.1. Top-down SEM images after selective PMMA etch of BCP films of various molecular weight (DB36, DB74, DB104 and DB176) in toluene deposited on PB3 as shown in **Table 2.2.** polymer brush layer. The brush layer was annealed at 170 °C for 6 h whilst the BCP film was anchored annealed at 180 °C for (a) 3 h, (b) 6 h, (c) 12 h and (d) 24 h.

24 h heating for the higher molecular weight systems (DB104 and DB176) and an island type structure can be clearly seen for both of these BCPs. Since the 3 h anneal time gives reasonable BCP patterns for all the molecular weights, PMMA selective etching was performed in PS-*b*-PMMA thin films for molecular weights 18k-18k, 37k-37k, 52k-52k and 85k-91k. **Figure 3.2** represents the SEM study of various molecular weights for the PMMA removal step for 6 s annealed for 3 h at 180 °C. It can be seen that the plasma etch does not damage the pattern and the finger print pattern is maintained. However, it is close to what might be expected if the PMMA

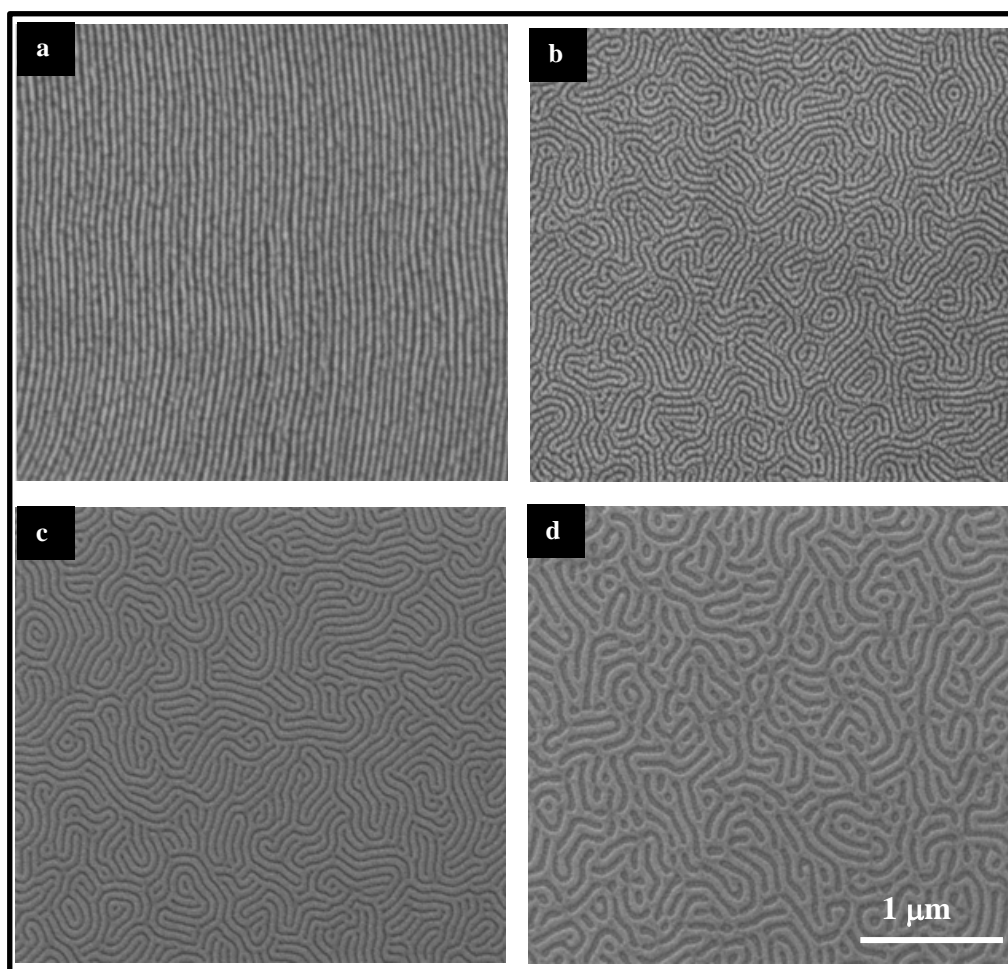


Figure 3.2. SEM images of PS-*b*-PMMA after selective PMMA etch, for 6 s after annealed for 3 h for 180 °C (a) 18k-18k, (b) 37k-37k, (c) 52k-52k and (d) 85k-91k.

is removed with an etch selectivity of 3:1. The removal of PMMA can be confirmed by SEM etch contrast as shown in **Figure 3.2**. Since PS-*b*-PMMA 37k-37k is an approximate intermediate BCP polymer system from 18k-18k to 85k-91k further

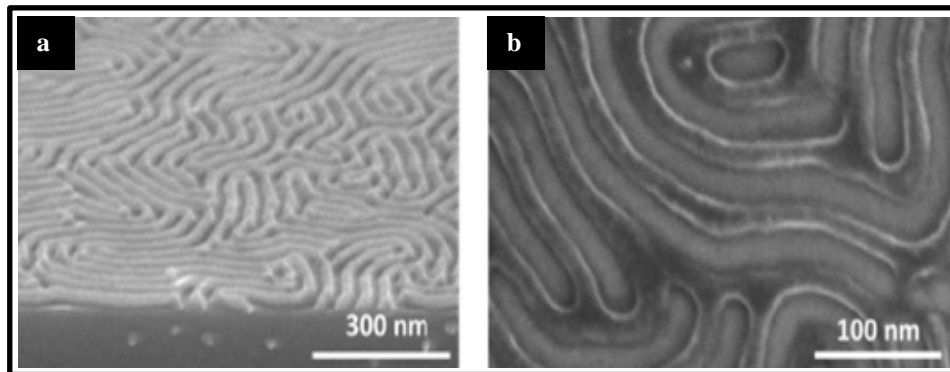


Figure 3.3. SEM images of PS-*b*-PMMA film after 120 s PMMA etch period. (a) Tilt image indicating PS removal and (b) higher resolution top down image.

more quantitative etch analysis of 37k-37k BCP system will be quite useful to understand the etch profiles. In **Figure 3.3(a)** a 70° tilt cross SEM image displays the PS structure of a PS-*b*-PMMA film after 6 s PMMA selective etch by ICP.

Figure 3.3(b) shows a higher resolution SEM image where the average size of the PS features can be estimated as about 19–20 nm. The ability to selectively etch these structures is a precursor to pattern transfer to the substrate as the PS structure will form a resist during silicon removal in an ICP etch as described in detail below. It also allows direct (secondary) electron microscopy imaging of the self-assembled polymer structures. The ability to pattern over a range of BCP molecular weights is shown in **Figure 3.4**. As can be seen, the molecular weight of the blocks determines the feature size. Analysis of the images shows that the variation in feature size is 44 nm (90k–85k), 32 nm (52k–52k), 20 nm (37k–37k) and 11 nm (18k–18k). It should be noted that the PS-*b*-PMMA (18k–18k) system provided almost ideal straight line patterns using normal procedures. This was found to be highly reproducible. It appears that at these small polymers chain lengths the random coil structure of the blocks is becoming highly extended allowing more ordered arrangements of the micro-phase separated structures. **Figure 3.5(a&b)** shows SEM and TEM images of a fully pattern-transferred surface following the silicon plasma etch process and

etch process and residual PS strip. PMMA had been completely removed using normal etch conditions for 6 secs. From the 70° tilt SEM image **Figure 3.4(a)** it can be readily seen that the etch process has facilitated good pattern transfer. The fidelity of the pattern transfer can be more directly observed using TEM cross-section as can be seen in **Figure 3.4(b)**. Etch selectivity is high as the 14 nm PS feature remaining

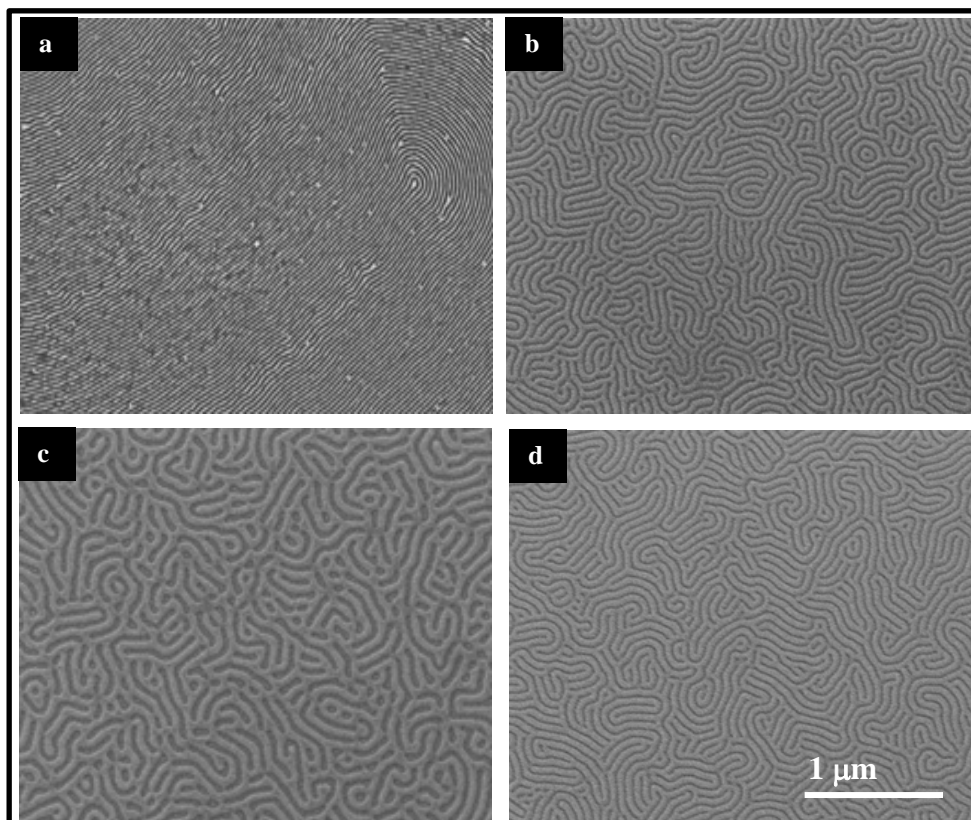


Figure 3.4. Top down SEM images of BCP patterns of various molecular weight PS-*b*-PMMA films on silicon substrates. Molecular weights as indicated in figures. All scale bars 1 μ m.

from the PMMA removal has resulted with a feature depth of around 32 nm. However, the silicon line features are not as regular as might be hoped. Both the base of the features and the top of the silicon lines are rounded somewhat. The rounding of the features at the base of the silicon lines produced probably reflects the rounding seen in the PMMA removed samples (**Figure 3.3(a&b)**). The rounding of the silicon lines probably results from the rounded PS features seen in **Figure 3.3(a)** as well as only limited etch anisotropy. As discussed more extensively below, the rounding is a

result of several processes. Certainly etch selectivity and anisotropy contributes as film thickness variation does. However, dimension and pattern regularity are important as they can determine product removal and re-deposition. The problems associated with using relatively soft resists such as PS at these nanometre dimensions are clear. It should be stressed that although these features have become

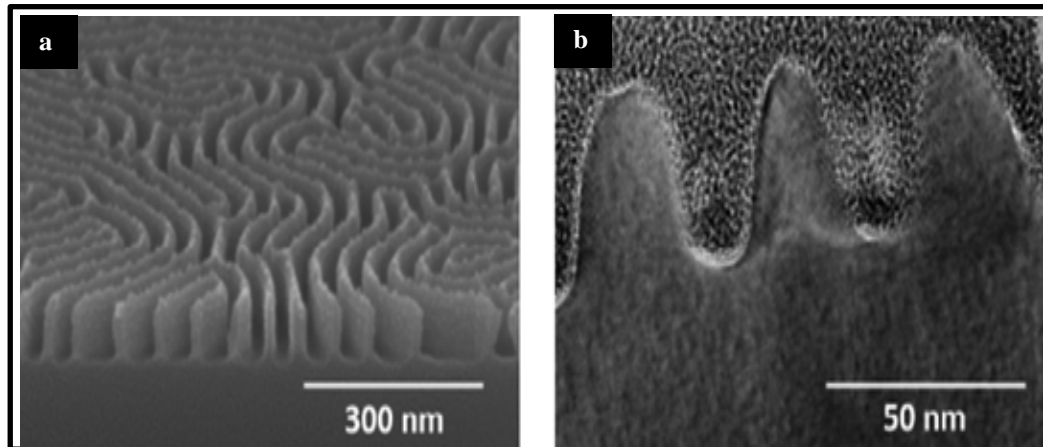


Figure 3.5. (a) SEM tilt image of pattern transferred polymer pattern. (b) TEM cross-section of the same.

rounded, dimension control through the silicon pattern transfer has been maintained. The features have an average base width of 19–20 nm in close agreement with the PS feature size noted above. The same pattern transfer treatment was used to look at the various polymer molecular weights used (85k–91k through to 18k–18k) and the data are described in **Figure 3.6(a–d)**. From all the TEM images that the crystallinity of the silicon is maintained and there is no indication of amorphization following the etch processes. This is true of even the smallest features even at the narrowest points of the lines suggesting this is a well optimized process. Two further points may also be noted. For the largest feature size, rounding at the base and the silicon lines is the smallest observed. This suggests that our proposed mechanism of diffusion limitations leading to product re-deposition is probably correct. The other point that is important is that rounding appears reduced for the 18k–18k small features. This is again consistent with our mechanism as these straight line features should allow easier gas transport. These data suggest that as feature size is reduced in

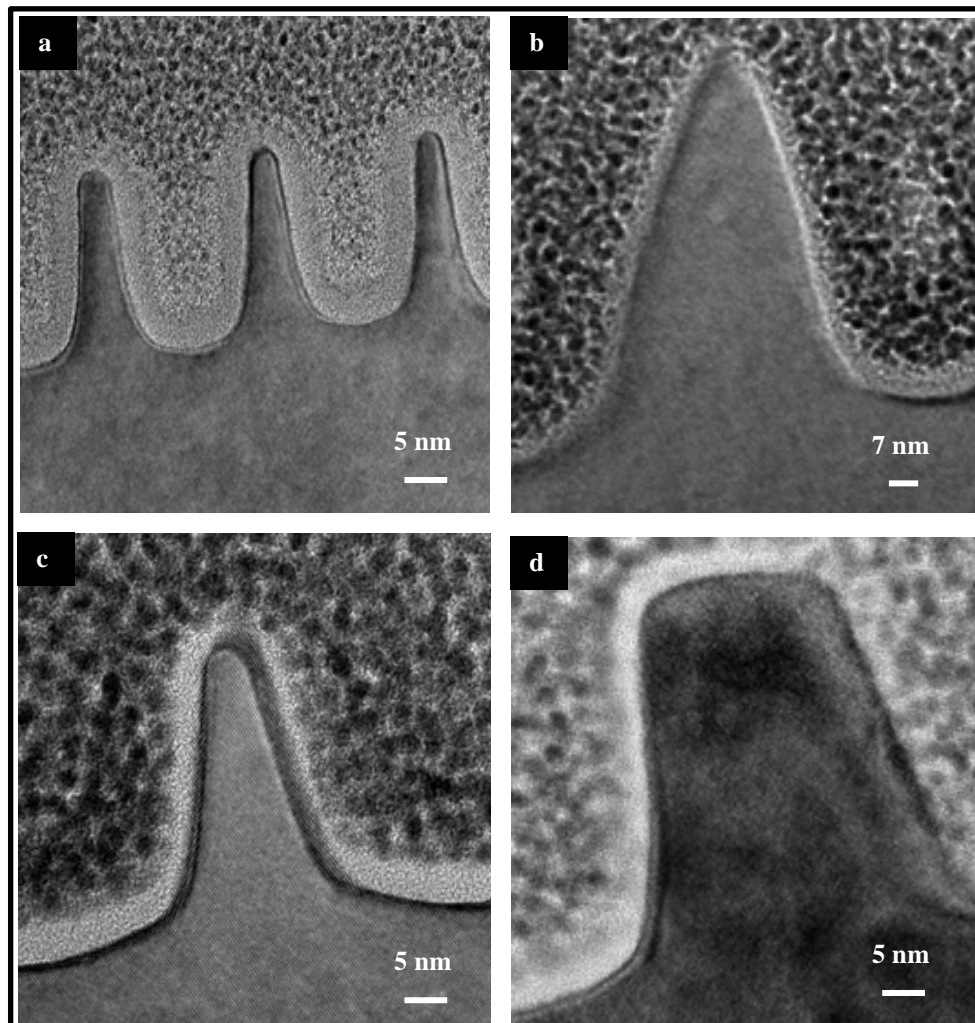


Figure 3.6. Cross-section TEM images of silicon lines formed via BCP pattern transfer. (a) PS-*b*-PMMA 85k–91k, (b) PS-*b*-PMMA 52k–52k, (c) PS-*b*-PMMA 37k–37k, (d) PS-*b*-PMMA 18k–18k.

microprocessors that complex designs will become progressively harder to maintain. Overall, the regularity of the BCP structure has resulted in dramatic improvement of the etch process. This work has shown that very small features can be produced in silicon using BCP lithography.

3.5 Conclusions

The use of self-assembled patterns to generate circuitry is in its infancy and it is clear that block copolymers are showing some promise. This work has shown that very small feature size silicon nanowire structures can be created from conventional

plasma etch methods and etches can be developed that are reasonably reproducible and reliable. In order to achieve the required etch selectivities and anisotropies, plasma conditions and apparatus will require careful attention to achieve required shape/size regularity. This chapter reports the feature size control of transistor by varying the molecular weight of BCPs.

3.6. References

- [1] G. E. Moore, In *Proc. SPIE*. **1995**, 2440, 2.
- [2] R. F. Pease, S. Y. Chou, *Proc. IEEE*. **2008**, 96, 248.
- [3] *International Technology Roadmap for Semiconductors* (ITRS) Edition Lithography ITRS, **2009**.
- [4] T. Ito, S. Okazaki, *Nature* **2000**, **406**, 1027.
- [5] R. G. Poulsen, *J. Vac. Sci. Technol.* **1977**, **14**, 266.
- [6] J. Hopwood, *Plasma Sources Sci. Technol.* **1992**, **1**, 109.
- [7] R. A. Gottscho, C. W. Jurgensen, D. J. Vitkavage, *J. Vac. Sci. Technol. B*. **1992**, **10**, 2133.
- [8] S. Banerjee, P. Elakkumanan, D. Chidambarao, J. Culp, M. Orshansky, *Proc. SPIE*. **2008**, 6925, 59250K.
- [9] D. Shamiryan, V. Paraschiv, W. Boullart, M. R. Baklanov, *High Energy Chem.* **2009**, **43**, 204.
- [10] H. Jansen, H. Gardeniers, M. De. Boor, M. Elwenspoek, *J. Micromech. Microeng.* **1996**, **6**, 14.
- [11] C. Bencher, H. Dai, Y. Chen, *Proc. SPIE*. **2001**, 7274, 72740G.
- [12] Y. Tzeng, T. H. Lin, J. Waddell, *J. Electrochem. Soc.* **1990**, **137**, 2612.
- [13] H. F. Winters, J. W. Coburn, *Surf. Sci. Rep.* **1992**, **14**, 161.
- [14] G. S. Oehrlein, *Handbook of plasma processing technology* ed S M Rossnagel (Park Ridge, NJ: William Andrew Publishing). **1990**, 196.

- [15] R. Legtenberg, H. Jansen, M. de Boer, M. Elwenspoek, *J. Electrochem. Soc.* **1995**, *142*, 2020.
- [16] S. Aachboun, P. Ranson, C. Hilbert, M. Boufnichel, *J. Vac. Sci. Technol. A.* **2000**, *18*, 1848.
- [17] L. Kenoyer, R. Oxford R, A. Moll, *Proc. 15th Biennial University/Government/Industry Microelectronics Symp. (Boise, ID)*. **2003**, 338.
- [18] J. Yeom, Y. Wu, M. A. Shannon, *Transducers '03 The 12th Int. Conf. on Solid State Sensors, Actuators and Microsystems (Boston, MA)*. **2003**, 1631.
- [19] S. L. Lai, D. Johnson, R. Westerman, *J. Vac. Sci. Technol.* **2006**, *24*, 1283.
- [20] S. A. McAuley, H. Ashraf, L. Atabo, A. Chambers, S. Hall, J. Hopkins, G. Nicholls, *J. Phys. D: Appl. Phys.* **2001**, *34*, 2769.
- [21] R. A. Farrell, T. G. Fitzgerald, D. Borah, J. D. Holmes, M. A. Morris, *J. Mol. Sci.* **2009**, *10*, 3671.
- [22] R. A. Farrell, N. Petkov, , M. A. Morris, J. D. Holmes, *J. Colloid Interface Sci.* **2010**, *349*, 449.
- [23] R. A. Farrell, N. Petkov, M. T. Shaw, V. Djara V, J. D. Holmes, M. A. Morris, *Macromolecules*. **2010**, *43*, 8651.
- [24] K. Asakawa K, T. Hiraoka T. *Japan. J. Appl. Phys. Part 1*. **2002**, *41*, 6112.

4.1. Abstract

Block copolymer lithography based on block copolymer (BCP) self-assembly can be used to develop soft mask nanoscale templates for subsequent pattern transfer to generate substrate features. Self-assembly of lamellar polystyrene-*b*-polymethylmethacrylate BCP of varying molecular weights from PS-*b*-PMMA (85k-91k) to (18k-18k) to generate silicon nanoscale features with fixed plasma etch conditions are reported in *Chapter 3*. It has been demonstrated that the feature size can also be controlled by a plasma over-etch process and it is discussed in detail in this chapter.

4.2. Introduction

Device miniaturization, as described by Moore's Law, has driven the semiconductor industry for several decades [1, 2]. The increase of transistor density seen over the last forty years has been largely achieved by ultra-violet photolithography but other patterning techniques are becoming potentially important as transistor sizes reach deep into the nanoscale [3]. In recent years, an emerging form of lithography based on the self-assembly (*via* microphase separation) of block copolymers (BCPs) has been investigated as a means to generate sub- 10 nm feature sizes at relatively low cost avoiding the use of highly expensive light sources [4-6]. Substrate features are formed via either a templating mechanism (selective filling/replacement of one block) [7] or where the BCP pattern is transferred to the substrate by means of etch techniques [3, 8-11]. Pattern transfer involves a selective etch to remove one block and subsequently using the remaining polymer as an etch mask in a second etch process as discussed in *Chapter3* [11]. Although, recent efforts have shown that the methodology can be integrated into a device fabrication manufacturing process [12], this work is its infancy and little critical assessment of the pattern transfer process has been made. This chapter seeks to provide data in properly validating the pattern transfer methodology and centres on the challenge of creating sub- 10 nm feature size patterns [6, 9, 13, 14]. Feature size in these systems is defined by the polymer chain length but below a critical dimension, the enthalpic driving force is not high enough to counter the entropic resistance to pattern formation and, in effect, each BCP system has a limiting lower feature size [9, 13,

15]. Further, the enthalpic force needs to be as large as possible to maintain low defect densities which are necessary for use in device fabrication.

This chapter deals with the use of nanoscale BCP patterns of polystyrene-*b*-polymethylmethacrylate (PS-*b*-PMMA) as soft masks using 85k-91k and 18k-18k. These systems have been subjected to an over-etch technique for the generation of substrate features. Control of feature size is shown and also that an ‘over-etch process’ can be used to generate feature sizes below that of the original polymer patterns. This work emphasises that whilst BCP nanolithography is promising, there are significant barriers to be overcome if this is to be a patterning technique for industrial application.

4.3. Materials and methods

4.3.1. Materials

Hydroxy-terminated random copolymer composed of styrene (S) and methyl methacrylate (MMA), denoted as HO-PS-*r*-PMMA, and the lamella-forming PS-*b*-PMMA diblock copolymers with Φ_{PS} of 0.50 were purchased from Polymer Source, Inc., Canada, and used as received. Number-average molecular weight (M_n) and polydispersity (M_w/M_n) of HO-PS-*r*-PMMA and PS-*b*-PMMA are listed in **Table 4.1**. The substrates used were reclaimed 8” silicon <100> wafers with a

Table 4.1. Characteristics of hydroxyl-terminated random copolymer and diblock copolymers composed of styrene and methylmethacrylate. M_w is the molecular weight.

M_w g mol ⁻¹	Designation	Polydispersity M_w/M_n	Mole fraction PS %	Pitch size nm	Si feature size nm
12,400	HO-PS- <i>r</i> -PMMA	1.25	0.58	-	-
36,000	18k-18k	1.07	0.46	29.5	7.5
74,000	37k-37k	1.07	0.49	51	17
104,000	52k-52k	1.09	0.49	65	27
176,000	85k-91k	1.12	0.47	89	35

native oxide layer. No attempt was taken to remove the native oxide of a few nm depth. Sulfuric acid, hydrogen peroxide and toluene were purchased from Sigma-Aldrich and used without further purification unless otherwise stated. Deionised water was used wherever necessary.

4.3.2. Polymer brush deposition and BCP thin film preparation

Silicon wafers were cleaned in a piranha solution (90 °C/60 h), rinsed with deionized water and dried under N₂. A hydroxy-terminated random copolymer brush (HO-PS-*r*-PMMA, ex-Polymer Source, Inc., Canada) solution of 1.0 wt % in toluene was spin-coated onto silicon wafers at 3000 rpm for 30 s. The substrates were annealed in vacuum at 170 °C. Unbound polymers were removed by sonication in toluene. Subsequently, PS-*b*-PMMA solutions of 1.0 wt % in toluene were similarly spin-coated onto the brush anchored surfaces before annealing at 180 °C under vacuum for 4 h to induce microphase separation as discussed in materials and methods section 2.3.2 and 2.3.3 in *Chapter 2*.

4.3.3. Soft mask template preparation and pattern transfer

Pattern transfer was achieved in three etch steps (using an OIPT Plasmalab System100 ICP 180 etch tool). Selective PMMA removal was achieved using an Ar/O₂ etch recipe at 10 mTorr and 100 W with O₂ (15 sccm) and Ar (5 sccm) for 6 s. An inductively coupled plasma silicon etch was then carried out at 15 mTorr and 500 W with SF₆ (15 sccm) and CHF₃ (80 sccm) for various periods to transfer the PS structure to the substrate. Remaining PS was removed using an O₂ ash recipe at 15 mTorr and 2000 W with 30 sccm O₂ for 10 s as discussed in results and discussion section of 3.4 in *Chapter 3*.

4.3.4. Characterization of materials

Polymer film thickness was determined by ellipsometry (Plasmos SD2000 Ellipsometer). The measurements were performed at 65° incidence angle with spectral range from 400-800 nm and the thickness data were obtained from least square fits to the spectral data of the ellipsometer. Top down scanning electron microscope (SEM) images were collected using a Field Emission Zeiss Ultra Plus-Scanning instrument with a Gemini® column at an accelerating voltage of 5 kV. SEM cross-sections were prepared using a FEI Strata 235-Focused Ion Beam (FIB) tool. Platinum was e-beam deposited at the substrates during milling. A Zeiss

Ultra Plus-SEM was used for imaging. Transmission electron microscope (TEM) lamella specimens were prepared by the Zeiss Auriga-Focused Ion Beam system and were analysed by an FEI Titan-Transmission Electron Microscope operating at an accelerating voltage of 130 kV.

4.4. Results and discussions

4.4.1. Polymer brush and BCP self-assembly

Vertical alignment of the PS and PMMA blocks can only be achieved after deposition of a ‘neutral’ brush layer that ensures that both blocks interact equally with the surface [8, 16]. Neutrality is achieved using a random copolymer brush (HO-PS-*r*-PMMA) with terminal hydroxyl groups to allow chemical bonding to the silicon substrate surface (*via* terminal silanol groups). A TEM cross-section image shown in **Figure 4.1a (insert)** shows the good uniformity and coverage (~ 100% of the substrate surface) of the film using the methodology used here. The brush layer thickness was measured at 5-6 nm. Polystyrene and polymethylmethacrylate adopt a random coil structure and can be modelled by $\langle h^2 \rangle_0 = M_w * 0.43$ and $\langle h^2 \rangle_0 = M_w * 0.42$ respectively, where $\langle h^2 \rangle_0$ is the mean-square end-to-end distance of the polymer coil and M_w is the molecular weight [17]. The random coil size can be estimated at about 7 nm which is in reasonable agreement with the measured brush layer thickness since some surface strain/relaxation in the thin film is expected. This would suggest that a complete monolayer of polymer molecules is formed from the brush procedure used here and provides an excellent surface for BCP deposition.

Deposition of the various symmetric PS-*b*-PMMA BCPs (**Table 4.1**) and vacuum annealing produces well defined lamellar structures over the entire substrate surface as also shown in **Figure 4.1(a-d)**. Polymers are indicated using the designation “molecular weight (PS) -molecular weight (PMMA)” so 18k-18k is a symmetric system with both blocks having a molecular weight of 18,000 g mol⁻¹.

The polymers are described in **Table 4.1** with 18k-18k representing the polymer giving the smallest feature size and this is around the minimum value expected for a PS-*b*-PMMA BCP [18]. The patterns formed here are similar to previous reports [3, 18]. The top down SEM images provided are after a brief

selective PMMA etch to provide image contrast. The decrease in domain size as a function of molecular weight is clear and is described in **Figure 4.1** and **Table 4.1**.

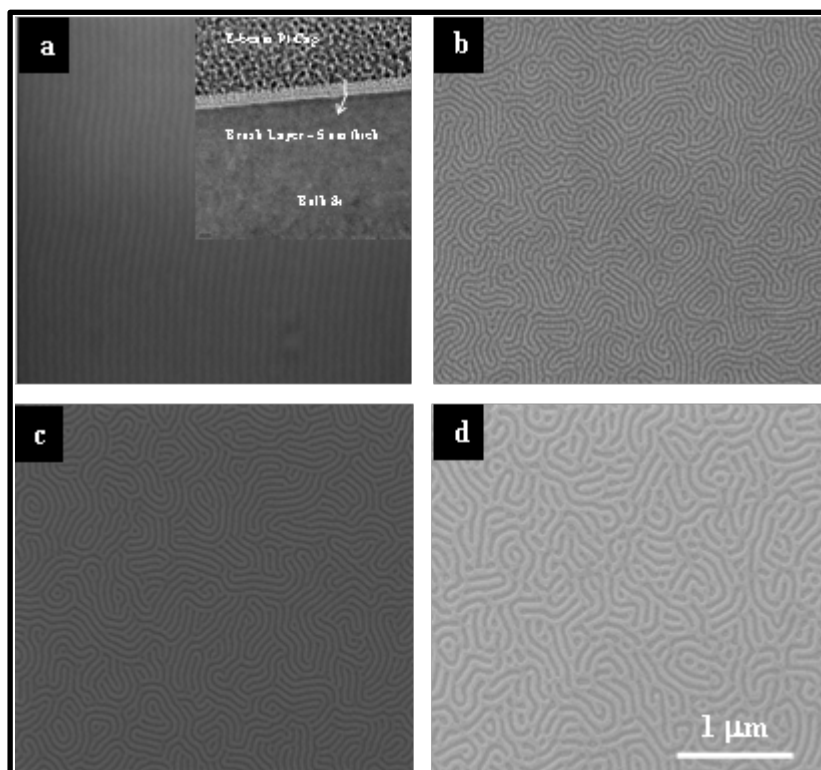


Figure 4.1. Top-down SEM data for various PS-*b*-PMMA BCPs. (a) 18k-18k, (b) 37k-37k, (c) 52k-52k and (d) 85k-91k. The scale bar shown in each one is 200 nm. The insert to **Figure 4.1a** is a TEM cross-section revealing the homogeneity of the brush layer. The lower layer is bulk silicon and the upper layer is evaporated Pt to protect the polymer film.

Domain (or pitch) size here is taken as the distance between two similar blocks in the pattern whilst feature size is the width of a single line. In **Figure 4.2** the pitch size is plotted as $(M_w)^{0.65}$ and good agreement is found between measured data and that calculated from pitch size = $0.36 M_w^{0.65}$ in accordance with expectations for Gaussian chain statistics and suggests a random coil structure within the blocks [19]. Note that pitch sizes are estimated from centre-to-centre distances and are averaged over 10 domain spacings. It should be noted that there is a distinct difference in the 18k-18k system and that of the other BCP systems, with much greater unidirectional alignment of the pattern for the lower molecular weight system. This was routinely

observed and is contrary to what might be expected in terms of the decreased interaction parameter expected at lower molecular weight. We tentatively suggest

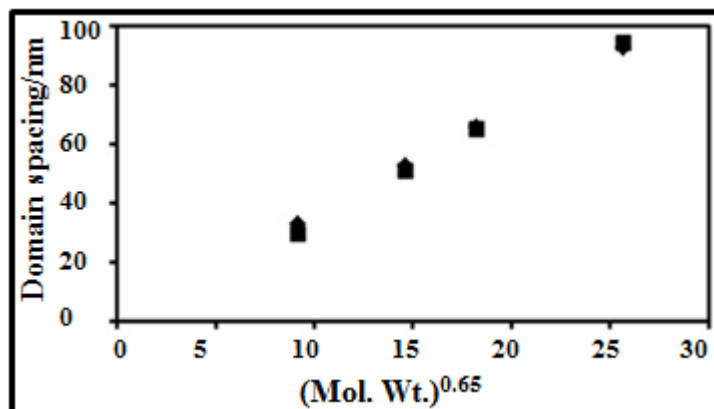


Figure 4.2. Calculated (▲) and measured (■) domain (or pitch size) as a function of molecular weight.

the additional ordering may be due to greater molecular motion predicted for lower molecular weight systems, which may allow the minimum energy conformation to be achieved during annealing.

4.4.2. Feature size control by plasma over-etch

These nanoscale templates can be used as soft masks to transfer the pattern to the underlying silicon and provide nanowire structures at the substrate surface as detailed in *chapter 3*. The selective PMMA etch recipe has been optimised by using PS and PMMA homopolymers having molecular weights corresponding to the molecular weights of the PS and PMMA blocks of the diblock copolymers as reported elsewhere [3, 8]. The feature size of the PS lines generated in this way are about half that of the domain size at 46, 34, 27 and 11.5 nm (see **Table 4.1** for explicit comparison) from the 85k-91k through the 18k-18k system, respectively. A silicon etch is then used to transfer the line pattern to the substrate. Illustrative data are provided for the 85k-91k and the 18k-18k (**Figure 4.3** and **Figure 4.4**, respectively). For all systems, an etch time of about 9 s was found to be optimum for pattern transfer providing best quality features (i.e. images show little sign of damage and the aspect ratio of the silicon nanowires formed is the highest possible value). Note in particular in these Figures that the silicon features obtained by etching show high crystallinity and lattice planes observed that extend continuously from the substrate into the feature. In this way, there is no evidence of defect

inclusion or amorphous region production as a result of the pattern transfer process. The nanowire size should be around that of the PS line width (since this is about half the pitch size) assuming ideal pattern transfer. This was not observed, and the actual

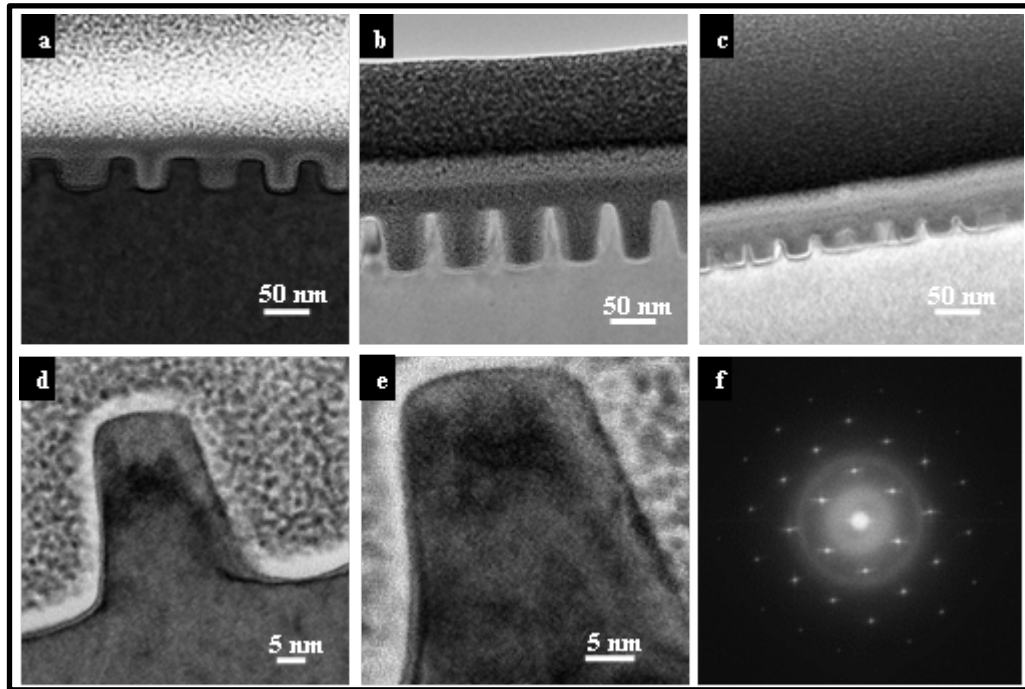


Figure 4.3. Cross-section TEM of silicon nanowires formed by pattern transfer of PS-*b*-PMMA nanopattern transferred into the substrate. (a), (b), (c) show features formed after a silicon etch for periods of 9, 17 and 21 s respectively. (d) is an expansion of the data shown in (a) and (e) is a high resolution image of same showing the silicon lattice planes present in these features. (f) is a small area electron diffraction pattern of a single nanowire feature also illustrating the crystallinity of the etched materials.

size of the nanowires produced was always less than half pitch as shown in **Table 4.1**. Note, that all widths are measured as a full-width at half-maximum-height and an average of 10 nanowires. The degree of isotropic etching appears to increase as the molecular weight of the BCP increases and hence, the feature size is reduced compared to the original polymer pattern. This can be seen directly in **Table 4.1** from the ratio of the measured silicon width to that calculated from the difference between the pitch and the PS width. This ratio varies from ~ 0.9 (85k-91k) to 0.33 (18k-18k) across the systems investigated here. This appears to be largely geometrical in nature and derives from the shape of the PS features that remain after

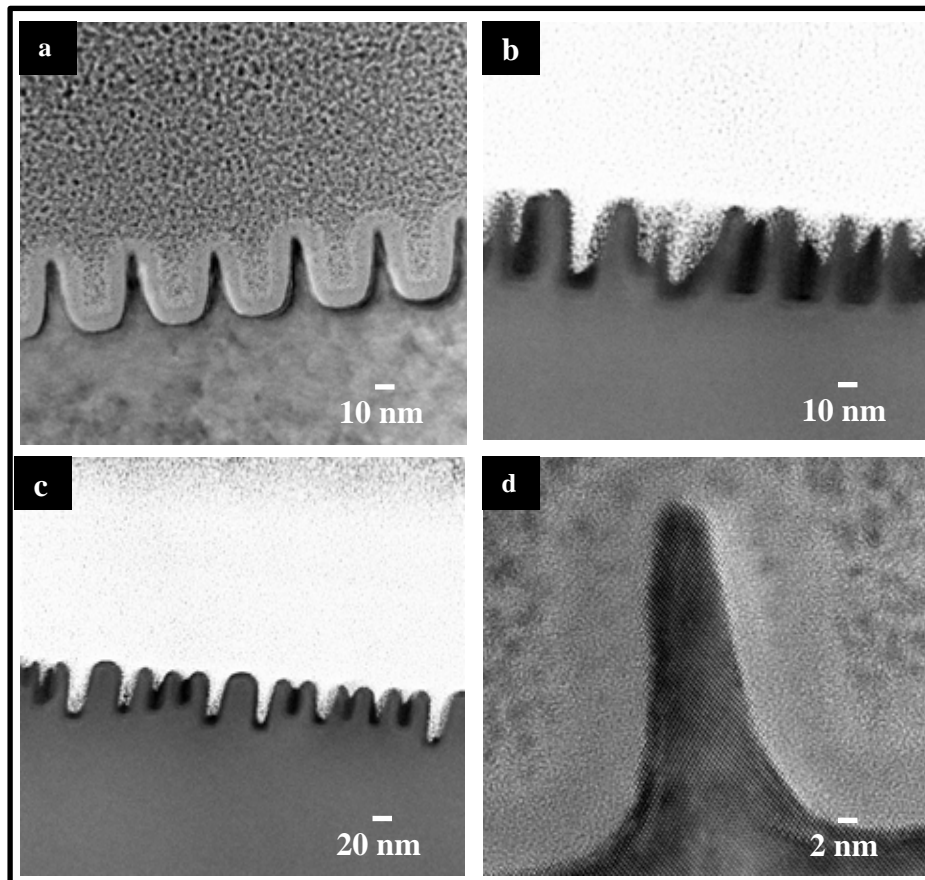


Figure 4.4. Cross-section TEM of silicon nanowires formed by pattern transfer of PS-*b*-PMMA nanopattern transferred into the substrate. (a), (b), (c) show features formed after a silicon etch for periods of 9, 17 and 21 s respectively. (d) is a high resolution image of same showing the silicon lattice planes present in these features. Note the triangular feature shape compared to that shown in **Figure 4.3**. The sidewall slope is approximately the same for a pattern sizes suggesting similar etch process and material variables.

PMMA removal. Typical examples of the PS mask line shapes that result from a selective PMMA etch are shown in **Figure 4.5(a) to 4.5(c)**. The PS line shapes are rounded with sloping edges and this resist mask shape is effectively transferred to the substrate during silicon etching and this has a more dramatic effect on narrow structures forming proportionally larger gaps between structures and more obviously non-rectangular feature cross-sections. This is illustrated schematically in **Figure 4.5(d) and 4.5(e)**. One of the major limitations of this sort of block copolymer lithography is that the feature size is determined by the molecular weight of the polymer blocks. Below a critical molecular weight (as detailed above), microphase

separation into well-ordered patterns cannot occur and, effectively, a minimum feature size exists [20]. For the PS-*b*-PMMA system, phase separation at molecular

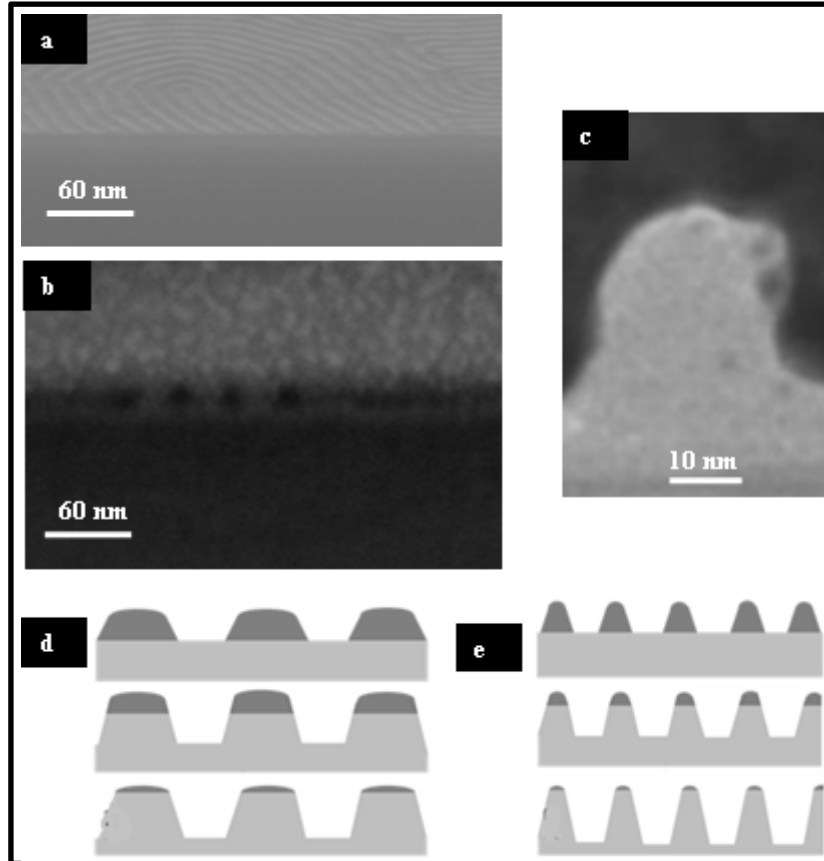


Figure 4.5. Details on the PS mask left after a selective PMMA etch. In all cases, SEM (a) and TEM (b and c) reveal the presence of rounded PS features. Data are shown for 18k-18k PS-*b*-PMMA. (d) and (e) are schematics showing how these mask profiles are transferred to silicon to produce the line edge profiles described in **Figures 4.3 and 4.4**.

weights significantly less than 18k-18k has not been observed and so features sizes much less than 10 nm are not realisable without polymer engineering. Note, that other BCP systems may generate smaller features sizes [21] but may lack the integratability of the PS-*b*-PMMA system where both polymers are well-known resists in conventional UV-lithography. An alternative methodology to reduce feature size might be realised by using etch conditions that allow isotropic etching of the silicon features. This form of over-etching was explored here. Illustrative examples of such over-etching are displayed in **Figure 4.6(a-d)** (top-down SEM) and

Figures 4.3 and 4.4 (cross-section TEM data). **Figure 4.6(e)** is a plot of the measured silicon feature size as a function of the etch time estimated from TEM

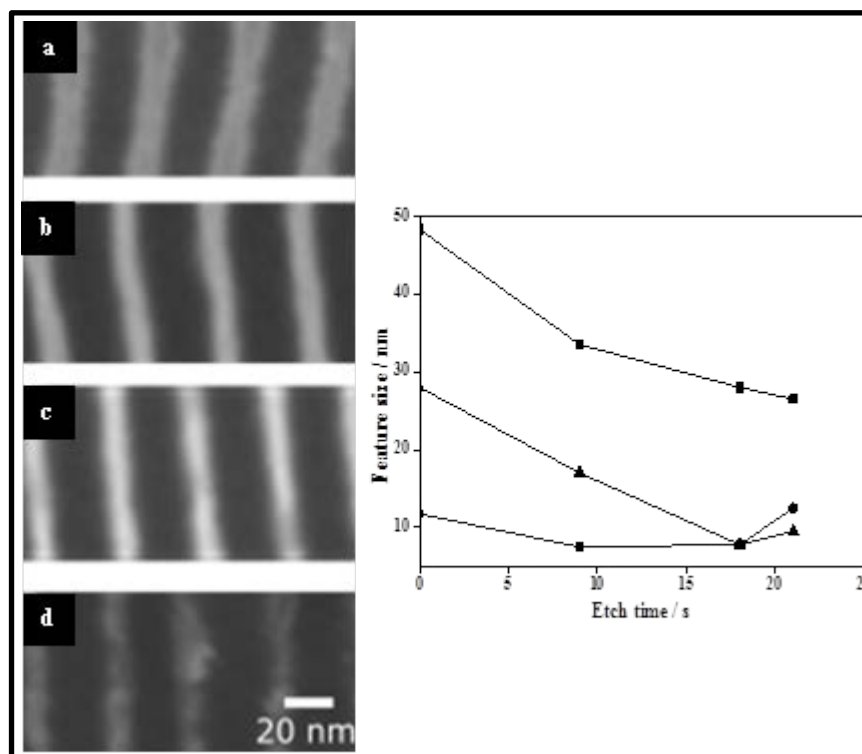


Figure 4.6. (a-d) SEM top-down images of silicon nanowires produced by pattern transfer using PS-*b*-PMMA 37k-37k at various silicon etch times of 9, 17, 21 and 30s. The graphical image shows the variation in feature size versus etch time for the 85k-91k (■), 37k-37k (▲) and 18k-18k (●) systems.

cross-sections (an average of at least 8 individual features). The exception is the data at 0 seconds which was estimated from Atomic Force Microscope images (the PS line width). It can be seen that even the 9 s etch period considerably reduces the feature size below that of the PS line width confirming the suggestion made above that the etching has a significant anisotropic component. For further etching (17s), the silicon lines or nanowires prepared via pattern transfer from larger molecular weight block copolymers (85k-91k to 37k-37k) reduce in dimension but, with the exception of the 85k-91k system, further etching does not reduce the feature size below a limiting value of about 7-9 nm and indeed the feature size apparently increase at the longest etch periods. The reason for the limiting value of feature size can be seen in **Figures 4.3 and 4.4**. At larger widths, the over etch process

apparently progressively decreases feature width as well as feature height and this is because the feature has approximately perpendicular sidewalls with the feature width at the top and bottom having a similar value. However, for the lower molecular weight systems (see **Figure 4.4**), the silicon features have a Gaussian like profile and as the features decrease in height, the width at half-maximum-height will tend to increase. The thinning of the sample height with etch can be clearly seen in **Figure 4.6(d)** where the wire is becoming so thin that contrast is becoming less clear. This rapid reduction in feature height can be clearly seen in **Figures 4.3** and **4.4** using cross-section TEM. What is also apparent is that the thinnest features are prone to significant damage (**Figure 4.4**) with features collapsing, partially collapsing and even merging. In all instances, including highly damaged systems such as shown in **Figure 4.3**, the etched features are revealed to be well-ordered single crystals. This suggests that the mechanical damage is caused by the fragility of the nanofeatures and/or low adhesion to the substrate. The mechanical fragility may be related to the cross sectional shape (and, hence, inherent strain) of these wires which is a direct result of the etching procedures and the mask shape resulting from development of the BCP mask by the selective polymer etch, etc. Whilst we suggest that the rounded shape of the smaller features is probably due strain from the inherent stress of the nanoscale features, we cannot rule out contributions from the plasma processing. It is likely that there are differential pressure differences exists for different feature sizes and gas composition may be altered. This will have effects on etch rates and hence the isotropic/anisotropic nature of the etch [3]. However, since the etch chemistry and conditions were carefully tuned this is most probably a minor contribution.

4.5. Conclusions

This work shows that extending the size of features formed by block copolymer lithography is possible using controlled isotropic etching. However, the results also suggest that there may be a limiting size that can be achieved. This limiting size may be related to the intrinsic mechanical properties of low diameter features or to their shape that is imposed on them through the pattern transfer techniques used. In this work, the non-ideal shape of the polystyrene mask formed by selective removal of the polymethylmethacrylate component results from the low

etch contrast of two similar polymers or the strength of the polymer features. This shape is transferred to silicon because the patterned PS polymer is not an ideal mask material (i.e. does not have a very high etch contrast compared to silicon). It is clear that the etch methods used here will require very significant optimisation to allow more ideal feature shapes (i.e. perpendicular side-walls) to be formed and this is also a necessity for proper device operation. It is also apparent, that the PS-*b*-PMMA system is unlikely to achieve the dimensions needed for continued miniaturisation of silicon based devices beyond the 8 nm (feature size) node. Fabrication-friendly, small feature size more etch compatible polymers require development and processing for ultra-small (sub 8 nm feature size) components and for the extended use of BCP-based methods in transistor technologies.

4.6. References

- [1] M. Freebody, *Photonic Spectra* **2011**, 45, 45.
- [2] C.A. Mack, *IEEE Trans. Semicond. Manuf.* **2011**, 24, 202.
- [3] D. Borah, M. T. Shaw, S. Rasappa, R. A. Farrell, C. T. O'Mahony, C. M. Faulkner, M. Bosea, P. Gleeson, J. D. Holmes, M. A. Morris, *J. Phys. D: Appl. Phys.* **2011**, 44, 202.
- [4] S. -J. Jeong, H. -S. Moon, J. Shin, B. H. Kim, D. O. Shin, J. Y. Kim, Y. -H. Lee, J. U. Kim, S. O. Kim, *Nano Lett.* **2010**, 10, 3500.
- [5] M. P. Stoykovich, H. Kang, K. C. Daoulas, G. Liu, C. -C. Liu, J. J. de Pablo, M. Mueller, P. F. Nealey, *ACS Nano* **2007**, 1, 168.
- [6] Y. S. Jung, J. H. Lee, J. Y. Lee, C. A. Ross, *Nano Lett.* **2010**, 10, 3722.
- [7] J. Chai, J. M. Buriak, *ACS Nano* **2008**, 2, 489.
- [8] R. A. Farrell, N. Petkov, M. T. Shaw, V. Djara, J. D. Holmes, M. A. Morris, *Macromolecules* **2010**, 43, 8651.
- [9] R. A. Farrell, T. G. Fitzgerald, D. Borah, J. D. Holmes, M. A. Morris, *Int. J. Mol. Sci.* **2009**, 10, 3671.
- [10] C. -C. Chao, T. -C. Wang, R. -M. Ho, P. Georgopoulos, A. Avgeropoulos, E. L. Thomas, *ACS Nano* **2010**, 4, 2088.
- [11] Y. Qiao, D. Wang, J. M. Buriak, *Nano Lett.* **2007**, 7, 464.

- [12] R. A. Farrell, N. T. Kinahan, S. Hansel, K. O. Stuen, N. Petkov, M. T. Shaw, L. E. West, V. Djara, R. J. Dunne, O. G. Varona, P. G. Gleeson, S. -J. Jung, H. -Y. Kim, M. M. Kolesnik, T. Lutz, C. P. Murray, J. D. Holmes, P. F. Nealey, G. S. Duesberg, V. K. Krstić, M. A. Morris, *Nanoscale* **2012**, 4, 3228.
- [13] C. Tsitsilianis, G. Staikos, *Macromolecules* **1992**, 25, 910.
- [14] P. Mokarian-Tabari, T. W. Collins, J. D. Holmes, M. A. Morris, *ACS Nano* **2011**, 5, 4617.
- [15] C. T. O'Mahony, R. A. Farrell, T. Goshal, J. D. Holmes, M. A. Morris, The thermodynamics of defect formation in self-assembled systems, Thermodynamics/Book 4", ISBN 979-953-307-047-5, InTech Publications.
- [16] E. Han, K. O. Stuen, Y. -H. La, P. F. Nealey, P. Gopalan, *Macromolecules* **2008**, 41, 9090.
- [17] L. J. Fetters, D. J. Lohse, D. Richter, T. A. Witten, A. Zirkel, *Macromolecules* **1994**, 27, 4639.
- [18] E. Sivaniah, Y. Hayashi, S. Matsubara, S. Kiyono, T. Hashimoto, K. Kukunaga, E. J. Kramer, T. Mates, *Macromolecules* **2005**, 38, 1837.
- [19] Y. Matsushita, K. Mori, R. Saguchi, Y. Nakao, I. Noda, M. Nagasawa, *Macromolecules* **1990**, 23, 4313.
- [20] J. Bang, S. H. Kim, E. Drockenmuller, M. J. Misner, T. P. Russell, C. J. Hawker, *J. Am. Chem. Soc.* **2006**, 128, 7622.
- [21] S. Park, D. H. Lee, J. Xu, B. Kim, S. W. Hong, U. Jeong, T. Xu, T. P. Russell, *Science* **2009**, 323, 1030.

5.1. Abstract

The directed self-assembly (DSA) of block copolymers (BCPs) thin films could enable a scalable, bottom-up, alternative to photolithography for the generation of substrate features at surfaces. The PS-*b*-PDMS (polystyrene-*b*-polydimethylsiloxane) system is attractive as it can be extended towards very small feature sizes (unlike the PS-*b*-PMMA system as discussed in *chapters 2,3&4*) as well as it having two blocks can be readily differentiated during pattern transfer. However, PS-*b*-PDMS offers a considerable challenge because of the chemical differences in the blocks which leads to poor surface-wetting, poor pattern orientation control and structural instabilities. These challenges can be mitigated by careful definition of the interface chemistry between the substrate and the BCP. This chapter reports controlled pattern formation in cylinder forming PS-*b*-PDMS system by use of a carefully controlled PDMS brush. Control of the brush was achieved using exposure to UV-O₃ for varying time. It is demonstrated that this treatment enhances surface wetting and coverage of the BCP. The modified brushes also enable DSA of the BCP on topographically patterned substrates. UV-O₃ exposure as used to reveal the BCP structure and provide an *in-situ* ‘hard mask’ for pattern transfer to the substrate.

5.2. Introduction

Increases in the performance of semiconductor devices have been largely determined by reduced device dimensions realized by increased resolution of the UV lithographic process (Moore's Law [1]) and feature sizes are reducing to sub 10 nm dimensions [2]. The development of logic and memory circuitry requires the fabrication of nanosized structures with high precision (structural regularity and position relative to defined locations and directions) and “top-down” UV lithography is used to manufacture transistors with sizes of 16 nm [3]. Various other top-down methodologies are being examined that might allow silicon based devices to reach their ultimate feature size and performance [3-7]. In parallel to the physical engineering of substrate features, the “bottom-up” approach based on hierarchical self-assembly of structures ranging from molecular building blocks through to nanoparticulates and macromolecular structures is the subject of intense research [8].

There are advantages and drawbacks in both approaches. In top-down methodologies further progress is critically related to source design, material interactions and thermal management [1-3]. On the other hand, it is highly challenging to achieve long-range translational order and robustness of systems fabricated with bottom-up approaches [9-11].

The directed self-assembly (DSA) of BCPs in topographically patterned substrates (graphoepitaxy) is a complementary technique that exploits both approaches [12-15]. The confinement of BCP structures within narrow topography can align BCP patterns into directional registry and was first reported by Li *et al.* for polystyrene-*block*-polymethylmetacrylate (PS-*b*-PMMA) [16]. Many authors have subsequently studied this system since it is compatible with established resist technologies [17, 18]. However, PS-*b*-PMMA has a relatively low Flory-Huggins parameter (χ) and this results in minimum feature size dimensions that are above that of the established UV-lithography method. Other polymers can exhibit lower minimum feature size including polystyrene-*block*-polyethyleneoxide (PS-*b*-PEO), with a reported 25 nm pitch size [19]. More recently, polystyrene-*block*-polyactide (PS-*b*-PLA) was systems have been developed that promise decreased feature sizes [20]. Polystyrene-*block*-polydimethylsiloxane (PS-*b*-PDMS) BCPs are also attracting much research effort. This BCP is very promising since its Flory-Huggins parameter ($\chi = 68/T - 0.037$) is relatively high allowing sub- 10 nm feature size scaling [21] as demonstrated for line forming non-symmetric PS-*b*-PDMS using a nanoimprint lithography (NIL)-assisted DSA approach [22]. A further attractive feature of this system is the chemistry and composition that allows it to be relatively easily processed into an on-chip etch mask that can be used for pattern transfer by selective etch methods [23].

However, in the PS-*b*-PDMS system two major issues arise: strong surface dewetting due to high its' hydrophobicity and difficulties in controlling feature orientation particularly for definition of parallel versus vertical cylinder alignment. To overcome these limitations, a surface pre-treatment with a PDMS brush is usually required [23]. However, it should be noted that whilst the use of a PDMS brush can improve the BCP thin films, dewetting, the BCP coverage at the substrate and regions of irregular thickness can remain problematical as reported here and

elsewhere [24-26]. However, despite the imperfect nature of these potentially important films, reports of methods of tuning the surface chemistry of PDMS brush in an effort to improve the BCP film and control orientation is scant [23, 24]. In order improve the brush chemistry using simple, reproducible and facile processing a method has been developed using UV-O₃ exposure to facilitate highly regular self-assembly of this system over large substrate areas. Results are described below as well as demonstration of the ability of the technique to yield an “on-chip mask” for etch transfer to the substrate surface.

5.3. Materials and methods

5.3.1. Materials

The planar substrates used were polished, test grade reclaimed 8” silicon <100> wafers (B doped, *p*- type, thickness 650 μm , and resistivity 6-14 $\Omega\cdot\text{cm}$) with a native oxide layer of ~ 2 nm. No attempt was made to remove the native oxide. The

Table 5.1. Details of polymer characteristics used in the present study.

Molecular weight, (M_n), g/mol	Polydispersity index, M_w/M_n	Mole fraction of PS, %	Volume fraction of PDMS, ϕ_{PDMS}	Description and designation
5,000	1.07	-	-	hydroxy-terminated PDMS and DS
45,500	1.15	0.60	0.34	cylindrical PS- <i>b</i> -PDMS and DC

topographically patterned substrates were etched silicon <100> and processed by means of conventional photolithography, mask and etch techniques. The channel width and depth were 450 nm and 50 nm, respectively. A hydroxy-terminated polydimethylsiloxane (PDMS) homopolymer and a cylinder-forming PS-*b*-PDMS diblock copolymer were purchased from Polymer Source, Inc., Canada, and used as received. Detailed properties of the polymers are summarized in **Table 5.1**. Toluene (99.8%, anhydrous), sulphuric acid (98%) and hydrogen peroxide (30%) were purchased from Sigma-Aldrich and used without further purification unless otherwise stated. De-ionized water was used wherever necessary.

5.3.2. Polymer brush deposition

Silicon substrates (planar and patterned) were cleaned in a piranha solution (1:3 v/v 30% H₂O₂:H₂SO₄) at 90 °C for 60 min, rinsed with deionized water (resistivity ≥ 18 M Ω /cm) several times and were blown dry with N₂. This piranha activation step removes any organic contamination and creates a high density of hydroxyl groups on the silicon substrates. An hydroxy-terminated polymer brush solution of 1.0 wt % in toluene was spin-coated onto the substrates at 3000 rpm for 30 s. Samples were annealed in a vacuum oven (Townson & Mercer EV018) at 170 °C under vacuum (-100 kPa) for 6 h. This allows the end-functional hydroxyl groups of the polymer brush to diffuse into the substrate and react with the substrate hydroxyl groups via surface condensation, resulting in polymer chain brushes chemically anchored to the substrate. Any unbound polymers were removed by sonication (Cole-Palmer 8891 sonicator) and rinsing in toluene. The brushes were ‘tuned’ by exposure to UV-O₃ for various times as detailed below.

5.3.3. BCP thin film preparation

Thin films of PS-*b*-PDMS were prepared by depositing a solution of 1.0 wt % BCP in toluene onto the polymer brush anchored substrates by spin coating at 3200 rpm for 30 s. This concentration was used because the thickness of the film obtained is consistent with the formation of a film containing a single row of PDMS cylinders parallel to the surface plane (described as a monolayer). As-cast films were solvent annealed in glass jars under saturated toluene environment at room temperature (~ 15 °C) for 3 h unless otherwise stated. Samples were removed from the glass jars after the desired anneal time and any excess solvent was evaporated in ambient conditions.

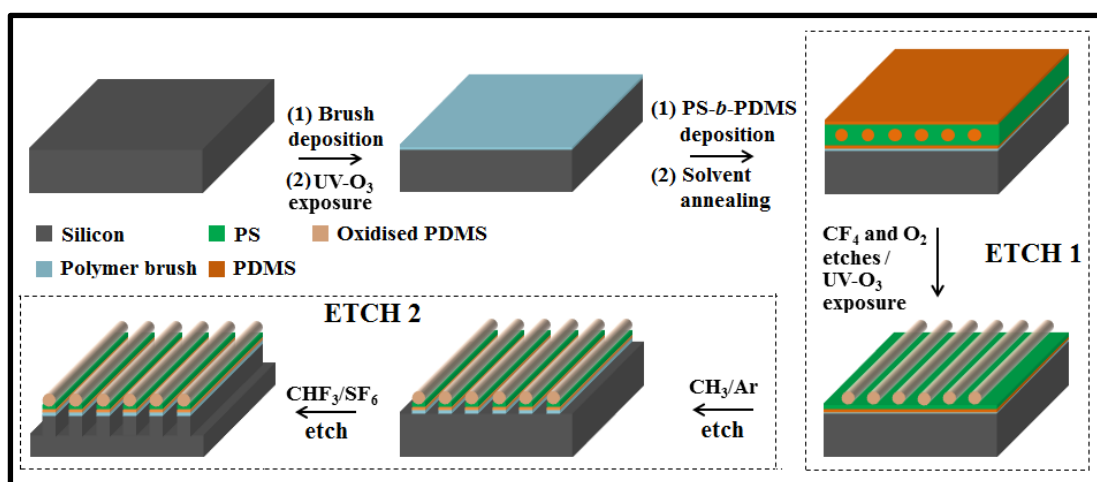
5.3.4. Ultraviolet-ozone (UV-O₃) treatment

All UV-O₃ treatments was performed in a PSD Pro Series Digital UV Ozone System; Novascan Technologies, Inc., USA. The UV source is two low-pressure mercury vapour grid lamps. Both lamps have an output current of 0.8-0.95 A and power of 65-100 W, as reported by the manufacturer, and have strong emissions at both wavelengths of UV radiation (184.9 nm and 253.7 nm). Samples were placed at a distance of about 4 mm from the UV source and exposed to UV irradiation. The system produces highly reactive ozone gas from oxygen that is

present within the chamber. The PDMS brush coated silicon substrates before and after cleaning i.e., removing the unbound polymer brush molecules (*as detailed in chapter 2*) were exposed to UV-O₃ for periods of 5-15 min. Solvent annealed PS-*b*-PDMS films (before and after CF₄ and O₂ etch) were also treated with UV-O₃ under similar conditions for 5-30 min. The PS phase was removed and the PDMS phase was oxidized into inorganic silicon oxide through this process.

5.3.5. Plasma etching of BCP thin films

Following, BCP film formation, atomic force microscopy cannot readily show the microphase separated structure because of the presence of a surface wetting layer of PDMS which must be removed to reveal the BCP arrangement [23]. The solvent annealed PS-*b*-PDMS films were first treated with a CF₄ (15 sccm) plasma for 5 s to remove any surface PDMS layer followed by an O₂ (30 sccm) plasma for 10 s with an ICP and RIE powers of 1200 W and 30 W, respectively, at 2.0 Pa with a helium backside cooling pressure of 666.6 Pa. These steps follow similar methodology developed by Ross *et al.* [23] and is described as ETCH 1. The process removes the PS component and forms an oxidized PDMS on the substrate. The sequential etching process was accomplished in an OIPT Plasmalab System100 ICP180 etch tool. Oxidized PDMS cylinders were then used as an etch mask for pattern transfer. A CHF₃ (80 sccm) and Ar (30 sccm) plasma for 5 s with an ICP and RIE powers of 400 W and 30 W, respectively, at 1.6 Pa was used to remove any residual PDMS wetting layer at the substrate surface. Milder etching conditions with CHF₃ was applied based on the assumption of having a very thin PDMS layer left after the pre-etch process. This was followed by the selective silicon etch using CHF₃ (80 sccm) and SF₆ (15 sccm) gases for 15 s with an ICP and RIE powers of 1200 W and 30 W, respectively, at 2.0 Pa with a helium backside cooling pressure of 1333.2 Pa to transfer the patterns into the underlying substrate. This pattern transfer process is known as ETCH 2. The detailed self-assembly steps starting with PDMS brush grafting, resultant structure formation and sequential etching steps are shown in Scheme 5.1.



Scheme 5.1. Schematic of PS-*b*-PDMS self-assembly on PDMS brush anchored substrates and subsequent etching steps.

5.3.6. Characterization of materials

5.3.6.1. Contact angle measurements

Advancing contact angles (θ_a) of deionized water was measured on the various substrate surfaces at ambient temperature using a Data Physics Contact Angle (model: OCA15) goniometer. Contact angles were measured on the opposite edges of at least three drops and averaged. The values were reproducible to within 2°.

5.3.6.2. Film thickness measurements

Film thickness was measured by ellipsometry (Plasmos SD2000 Ellipsometer). An average of three readings collected from different locations on a sample surface was reported as the film thickness result.

5.3.6.3. FTIR measurements

An IR660, Varian infrared spectrometer was used to record the FTIR spectra. The measurements were performed in the spectral range of 4000-500 cm⁻¹, with a resolution of 4 cm⁻¹ and data averaged over 32 scans.

5.3.6.4. Scanning electron microscope (SEM)

Top-down and cross-sectional scanning electron microscope (SEM) images were obtained by a high resolution (< 1 nm) Field Emission Zeiss Ultra Plus-Scanning Electron Microscope with a Gemini® column operating at an accelerating voltage of 5 kV. An FEI Strata 235-Focused Ion Beam (FIB) tool was used to generate FIB lamellae cross-sections. E-beam produced platinum was deposited at

the substrate followed by the ion-beam deposited platinum. Milling and polishing of the samples were carried out at the lower aperture size and the specimen was imaged under the higher resolution Zeiss Ultra Plus-SEM.

5.4. Results and discussion

5.4.1. BCP self-assembly on PDMS brush

The PDMS brush (thickness ~ 4.3 nm as measured by ellipsometry) facilitates self-assembly in PS-*b*-PDMS BCP films, but a wetting PDMS layer is formed at the gas-BCP and substrate-BCP interfaces of the patterns as reported by Ross *et al.* [23]. This is as expected since the PDMS block is likely to preferentially segregate at the air/polymer interface [27] because of lower surface tension of PDMS ($\gamma = 19.9$ mN m⁻¹) as compared to PS ($\gamma = 40.7$ mN m⁻¹) [28]. Further, at the substrate-BCP interface, formation of a PDMS wetting layer is expected because of the favourable interactions of the brush and the PDMS block. The formation of this sandwich structure leads to cylinders parallel to the surface plane [23]. **Figure 5.1(a, b)** shows the arrangement of the PDMS cylinders obtained for the microphase separated PS-*b*-PDMS films deposited on PDMS brush as revealed by the etch plasma treatment, ETCH 1, as described above. The oxidation of the PDMS cylinders during ETCH 1 is confirmed by FTIR with the detection of a Si-O-Si signal at 1098 cm⁻¹ [29] as shown in **Figure 5.1(c)**. The inset cross-section SEM images in **Figure 5.1(a, b)** clearly show the development of substrate areas with different BCP film thickness and regions containing monolayer (i.e. a single PDMS cylinder) and multilayers (multiple layers of cylinders) can be seen. Further, the images illustrate at least partial removal of the PS matrix exposing empty spaces in the PDMS template. The schematics of monolayer and multilayers of PDMS cylinders are provided in insets in **Figure 5.1(a, b)**. It is evident that good ordering and correlation length of PDMS cylinders are observed on a macroscopic scale (in microns). The mean PDMS cylinder spacing, L_0 , and line width, $\langle d \rangle$, are found to be 33.4 nm and 16.2 nm, respectively. The varying BCP film thickness derives from poor film wetting characteristics and, as discussed above, is a major issue with this

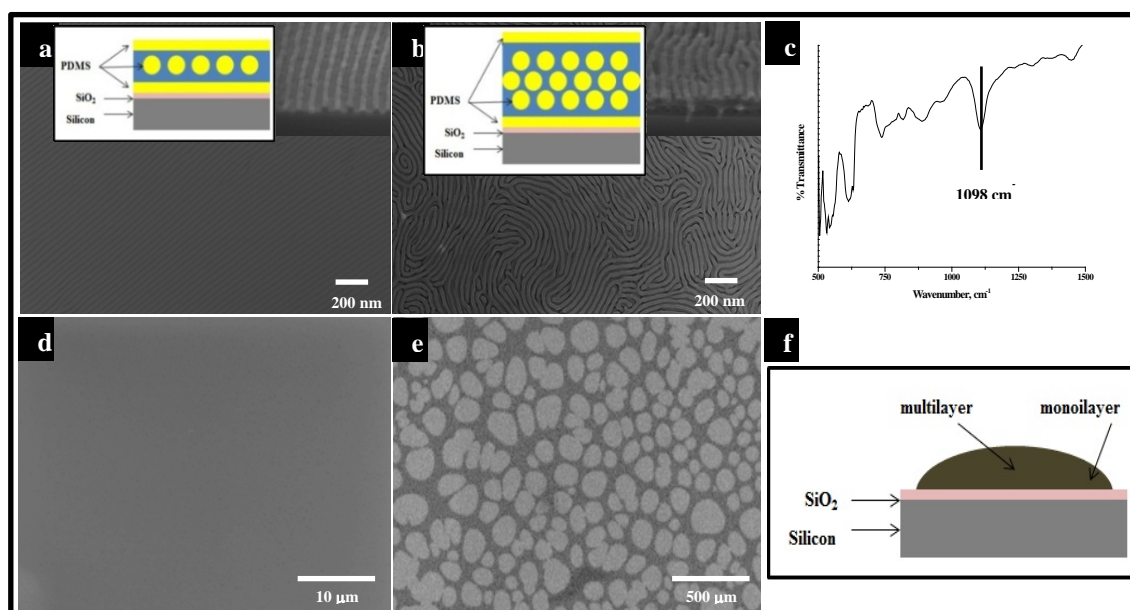


Figure 5.1. Top-down SEM images of *in-plane* PDMS cylinders on planar silicon substrates after a sequential CF_4 and O_2 plasma etches of microphase separated PS-*b*-PDMS films. The substrates were anchored with PDMS brush to get microphase separation of PS-*b*-PDMS film by solvent annealing in a saturated toluene environment for 3 h. Monolayer and multilayers of *in-plane* PDMS cylinders are shown in (a) and (b), respectively. Insets in (a) and (b) are the cross-section SEM images showing monolayer and multilayers of PDMS cylinders and respective schematics. (c) is the FTIR spectrum of the oxidized PDMS cylinders after CF_4 and O_2 plasma etches of microphase separated PS-*b*-PDMS film. The SEM images of PDMS brush anchored planar silicon substrates after cleaning and microphase separation of PS-*b*-PDMS are shown in (d) and (e), respectively. The schematic showing the monolayer and multilayers of PDMS cylinders in dewetted regions is given in (f).

system and leads to the multilayer pattern formation seen even when the amount of material should form a simple cylinder monolayer (as here). As shown in **Figure 5.1(e)**, the coverage obtained for the PDMS brush appears to be ~60% of the overall area even though the brush layer (**Figure 5.1(d)**) appears to be very homogeneous without any island formation/defect sites. The oval/round shaped areas (islands) in **Figure 5.1(e)** are dewetted regions of BCPs that have a dome-like structure as illustrated in **Figure 5.1(f)**.

5.4.2. Dewetting and UV- O_3 exposure of PDMS brush

The poor wetting behaviour noted above using a PDMS brush can be improved by exposing the PDMS brush to UV- O_3 and can be assessed with water contact angle as summarized in **Table 5.2**. The brush coated annealed samples were

exposed to UV-O₃ for different times before and after cleaning i.e., removing the unbound polymer brush molecules as mentioned in the experimental section and the

Table 5.2. Water contact angle and film thickness data of polymer brush and diblock copolymer films on silicon substrates.

Material designation	Deposition condition	Contact angle/ ^o	Film thickness/nm
SiO ₂ /Si	as received	44.7 ±2	-
SiO ₂ /Si	piranha cleaned	29.5 ±2	-
DS00AC	as cleaned	112.6 ±2	4.3
DS05AC	UV-O ₃ = 5 min	88.5 ±2	4.5
DS10AC	UV-O ₃ = 10 min	67.3 ±2	4.6
DS15AC	UV-O ₃ = 15 min	39.0 ±2	4.9
DS05BC	UV-O ₃ = 5 min	103.8 ±2	4.2
DS10BC	UV-O ₃ = 10 min	74.9 ±2	4.7
DS15BC	UV-O ₃ = 15 min	61.2 ±2	4.6
BCP + DS00AC	diblock on modified substrate		31.6
BCP + DS05AC	ibid		32.1
BCP + DS10AC	ibid		32.5
BCP + DS15AC	ibid		32.6
BCP + DS05BC	ibid		33.0
BCP + DS10BC	ibid		31.3
BCP + DS15BC	ibid		33.2

Note: Samples designated as DSXXAC or DSXXBC. DS = PDMS brush, BCP = the PS-*b*-PDMS diblock, AC= after cleaning, BC= before cleaning. XX is the UV-O₃ time.

water contact angle was measured. The static water contact angle of as-received silicon substrate was found to be 45° which is reduced significantly to 30° after piranha treatment. The lower contact angle is consistent with hydroxylation of the surface. For the cleaned surfaces, the attachment of the PDMS brush results in a surface having a contact angle of 112° as might be expected from a monolayer of the hydrophobic molecule. (**Table 5.2**). The gradual decrease in water contact angle with the increase of UV- O_3 exposure time is consistent with the oxidation of the PDMS to SiO_2 type moieties and suggests the properties of the substrate could be altered to provide more effective surfaces for BCP coating. The samples that had not been cleaned show a similar trend but in all cases the contact angle is slightly higher than that measured on the cleaned surfaces. This is probably related to a lower surface coverage of the brush at the non-cleaned surfaces since there are fewer hydroxyl sites and UV-exposure results in less hydrophobic moieties deriving from oxidation of PDMS. The brush modified surfaces at cleaned and non-cleaned surfaces after various UV- O_3 treatments were imaged and top-down SEM data are presented in **Figure 5.2**.

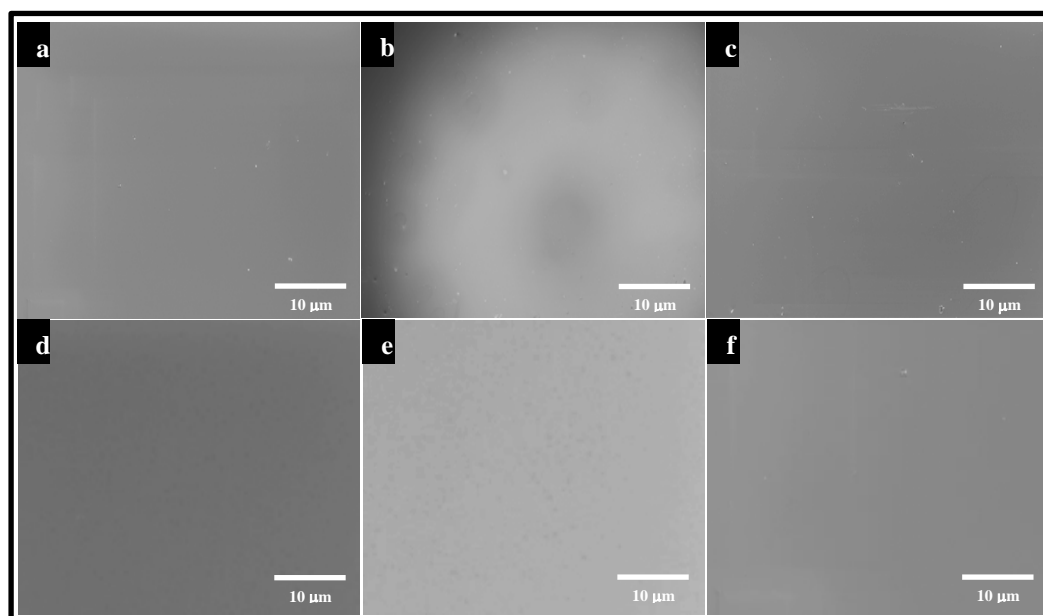


Figure 5.2. Top-down SEM images of PDMS brush anchored planar silicon substrates after cleaning, exposed to UV- O_3 for 5 min (**a**), 10 min (**b**) and 15 min (**c**). The images before cleaning are given in (**d**), (**e**) and (**f**) for 5 min, 10 min and 15 min, respectively.

The surface chemistry of the PDMS brush coated substrates changed significantly upon UV-O₃ treatment. There is a gradual decrease in contact angle with the increase in exposure time irrespective of the brush cleaning conditions. These images reveal a uniformly smooth surface for the various treatments. There are small white dots visible after the UV-O₃ treatment and these are thought to derive from local over oxidation and formation of SiO₂ particles. The brush surfaces were further characterized using ellipsometry and the results are presented in **Table 5.2**. The thickness of the brush layers after cleaning and without UV-O₃ treatment was found to be ~4 nm which is slightly higher (4.5-4.9 nm) in the UV-O₃ treated samples. This minor increase in thickness is consistent with oxidation of the PDMS which results in a volume expansion of the polymer.

5.4.3. FTIR study of the PDMS brush

The FTIR measurements of UV-O₃ exposed and unexposed PDMS brush anchored silicon substrates are shown in **Figure 5.3**. The IR spectra of the brush coated substrates show a well-resolved Si-O-Si vibration band near 1098 cm⁻¹ indicative of silica materials [29].

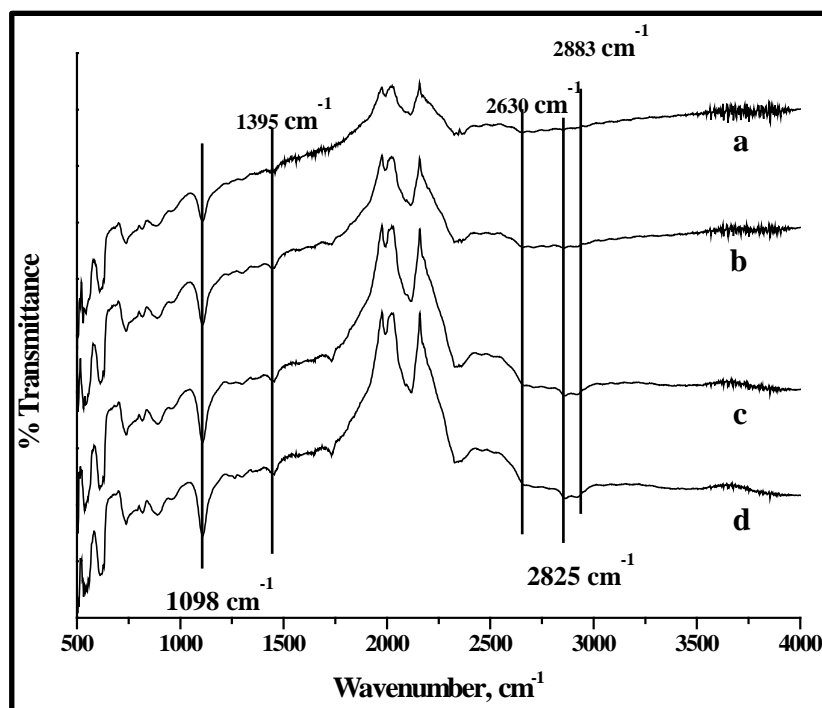


Figure 5.3. FTIR spectra of PDMS brush anchored planar silicon substrates after cleaning exposed to UV-O₃ for 0 min (a), 5 min (b), 10 min (c) and 15 min (d).

The intensity of this band increases with the increase in UV-O₃ exposure time. This could be associated with the oxidation of the PDMS with UV-O₃ and formation of silica type species. It should be noted that the silicon content of the polymer brush is ~36% based on its molecular weight which could form a significant amount of SiO₂ on oxidation. However, there may be a minor contribution from the native oxide layer of the silicon substrate which is exposed with the increase of UV-O₃ exposure time. The FTIR spectra of the brush layers also show a strong OH valence vibration band near 2630 cm⁻¹ and, like the Si-O-Si bands, this OH band increases with increasing exposure. The presence of the OH band is probably due to hydroxylation and attached water through hydrogen bonding. The peaks observed at 1395, 2825 and 2883 cm⁻¹ can be assigned to CH₃, CH₂ and CH stretching vibrations [30], respectively.

5.4.4. BCP self-assembly on UV-O₃ exposed polymer brush

Thin films of PS-*b*-PDMS deposited on UV-O₃ exposed PDMS brushes show considerable improvement in the wetting properties of the substrate towards the BCP. The coverage of the BCP is improved from 60 % in to around 90 % on casting the BCP onto the UV-O₃ exposed PDMS coated surfaces. This increase in wetting of the BCP at the UV-O₃ treated brush amended substrate can be clearly seen in **Figure 5.4(A)**. It could be the case that the oxidised PDMS-OH surface facilitates the PDMS (brush)-PDMS (BCP) interaction and improves the wetting property of the BCP. It can be noted that the decrease in dewetting also ensures a commensurate decrease in thickness variation and an increased probability of forming a regular film containing only a single layer of PDMS cylinders. The results of the sequential CF₄ and O₂ etch to reveal the PDMS cylinder structure is presented in **Figure 5.4(B)**. SEM images were taken at different locations on the substrate and show that the orientation is homogeneous over the entire surface. It is also apparent that the film consists of a single layer of PDMS cylinders. The degree of ordering and correlation length of PDMS cylinders is very good on a macroscopic scale irrespective of the UV-O₃ exposure time. The top-down and cross-section SEM images (**Figure 5.4(B)**) of the etched films confirm the removal of upper wetting PDMS layer as well as removal of the majority of the PS matrix. The average L_0 and $\langle d \rangle$ values were measured at 33.5 nm and 15.8 nm respectively. These are similar to those measured

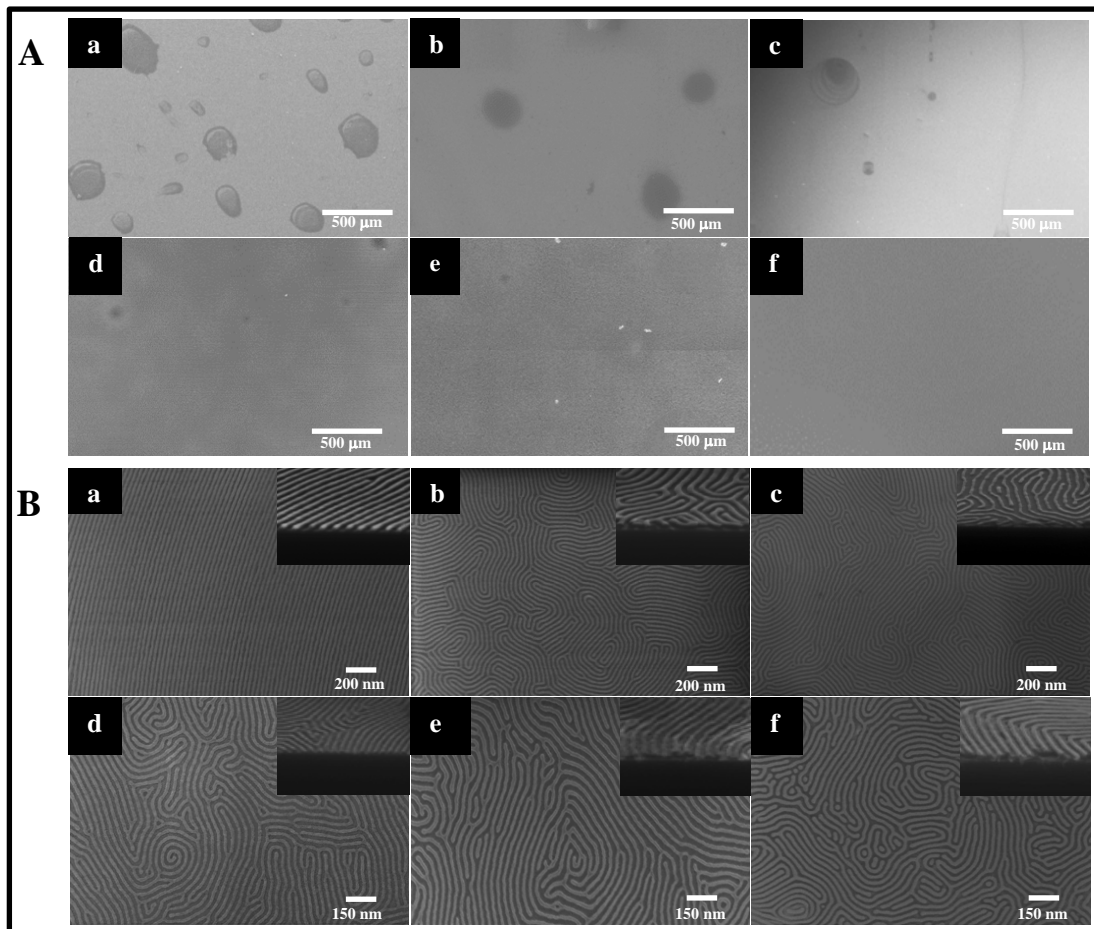


Figure 5.4. (A) Top-down SEM images showing the coverage and extent of dewetting of microphase separated PS-*b*-PDMS films. The PDMS brush anchored substrates after cleaning were exposed to UV-O₃ for 5 min (a), 10 min (b) and 15 min (c). SEM images of PS-*b*-PDMS film coverage on PDMS brush anchored substrates prior to cleaning, exposed to UV-O₃ for 5 min, 10 min and 15 min are shown in (d), (e) and (f), respectively. (B) Top-down SEM images of *in-plane* PDMS cylinders on planner silicon substrates after a sequential CF₄ and O₂ plasma etches of microphase separated PS-*b*-PDMS films. The substrates were anchored with PDMS brush to get microphase separation of PS-*b*-PDMS film by solvent annealing in a saturated toluene environment for 3 h. SEM images of *in-plane* PDMS cylinders on PDMS brush anchored substrates after cleaning and exposing to UV-O₃ for 5 min, 10 min and 15 min are shown in (a), (b) and (c), respectively. Insets in (a), (b) and (c) are the cross-section SEM images. The *in-plane* PDMS cylinders on PDMS brush anchored substrates prior to cleaning, exposed to UV-O₃ for 5 min, 10 min and 15 min are shown in (d), (e) and (f), respectively. Insets in (d), (e) and (f) are the cross-section SEM images.

on the non-modified brush surface and suggest no changes in structure exist. It can be seen from the cross-section images that the oxidized PDMS domains have become rounded during the etch process indicating that it is partially isotropic. It

should be noted that the L_0 measured from these images is somewhat less than that expected from the polymer molecular weight and composition. The BCP with a PDMS volume of 34.0% should ideally give L_0 of 35 nm [31]. This reduction is consistent with the CF_4 and O_2 plasma oxidizing the PDMS moieties to silica type species and reduction of the volume and ‘hence’ size. Further, it might be expected that cross-linking the PS matrix could be induced by the oxygen plasma treatment [32] and this could result in volume contraction of the polymeric film and consequently the observed decrease of the line width.

5.4.5. Directed self-assembly by graphoepitaxy

As discussed earlier, surface treatment with polymer brushes facilitates self-assembly, short-range domain ordering, defect minimization, and improves the surface wetting of the BCP. However, to achieve long-range pattern ordering, this surface treatment must be consistent with the graphoepitaxy technique to facilitate the alignment of the pattern and facilitate directed self-assembly of the BCP [23, 24, 33]. Ideally, the brush layer should have preferential chemistry to the PS which prevents PDMS forming at the channel wall and which then ensures alignment of the cylinders to the channel wall. To study the effect of the UV- O_3 tuned surface chemistry on graphoepitaxial alignment, the patterned substrates pre-coated with polymer brush were exposed to UV- O_3 for 5-15 min prior to BCP deposition.

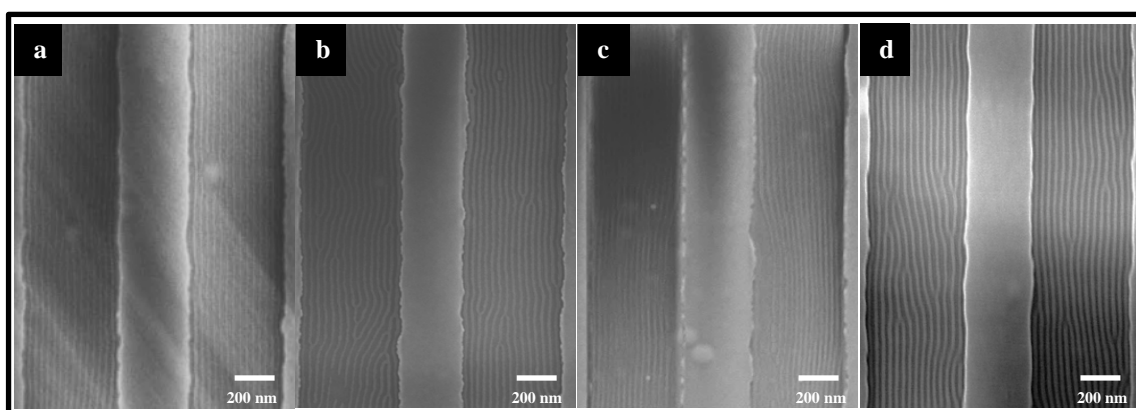


Figure 5.5. Top-down SEM images of *in-plane* PDMS cylinders on patterned silicon substrates after a sequential CF_4 and O_2 plasma etches of microphase separated PS-*b*-PDMS films. The substrates were anchored with PDMS brush to get microphase separation of PS-*b*-PDMS film by solvent annealing in a saturated toluene environment for 3 h. The PDMS brush anchored substrates after cleaning were exposed to UV- O_3 for 0 min (a), 5 min (b), 15 min (c) and 30 min (d) as detailed in the experimental section.

Figure 5.5 shows the *in-plane* PDMS cylindrical pattern formed in the topography as revealed by ETCH 1. It can be seen that the confining topography is highly effective in ordaining directed self-assembly and the PDMS domains are orientating parallel to the trench base with excellent translational alignment to the channel sidewall.

The translational alignment of PDMS cylinders on unmodified PDMS brush anchored substrates is excellent with correlation lengths of several micrometres. The results of UV-O₃ exposed polymer brushes appear to indicate slightly less well-ordered than the pristine brush surfaces with increased numbers of defects and disclinations visible. However, may be somewhat difficult to quantify as most defects in this system appear to arise because of defects in the topography and roughness of the sidewall as the pattern cannot compensate for an effective variation in the channel width. The effects of silica-like particulates precipitating the defects/disclinations can also not be ruled out.

5.4.6. UV-O₃ exposure of microphase separated PS-*b*-PDMS films

The need for the ETCH1 process to reveal the BCP nanopattern is inconvenient, lengthy and expensive. It was considered worthwhile investigating if the UV-O₃ process could be used for the same purpose. The microphase separated PS-*b*-PDMS films were exposed to UV-O₃ for varying time and the results are presented in **Figure 5.6(A)** and **Figure 5.6(B)**, for planar and patterned substrates, respectively. Note that for these studies, the PDMS brush used was not treated with UV-O₃ before BCP deposition. It can be seen in the figures that UV-O₃ exposure is successful in exposing the PDMS cylinder structure whilst removing the PS matrix. This proven by the cross-section SEM images in the inset to **Figure 5.6(A)**. Note that the exposed, oxidised PDMS cylinders became rough after a 30 min UV-O₃ treatment as can be seen in **Figure 5.6(B)**. This roughness is probably the result of almost complete oxidation to silica and under the treatment, the silica-type moieties nucleate into particulates. In this way, the results demonstrate that UV-O₃ can be used as an alternative to the standard sequential CF₄ and O₂ plasma etches to reveal the surface structure but it may not be the optimum technique of homogeneous structures are required for e.g. pattern transfer.

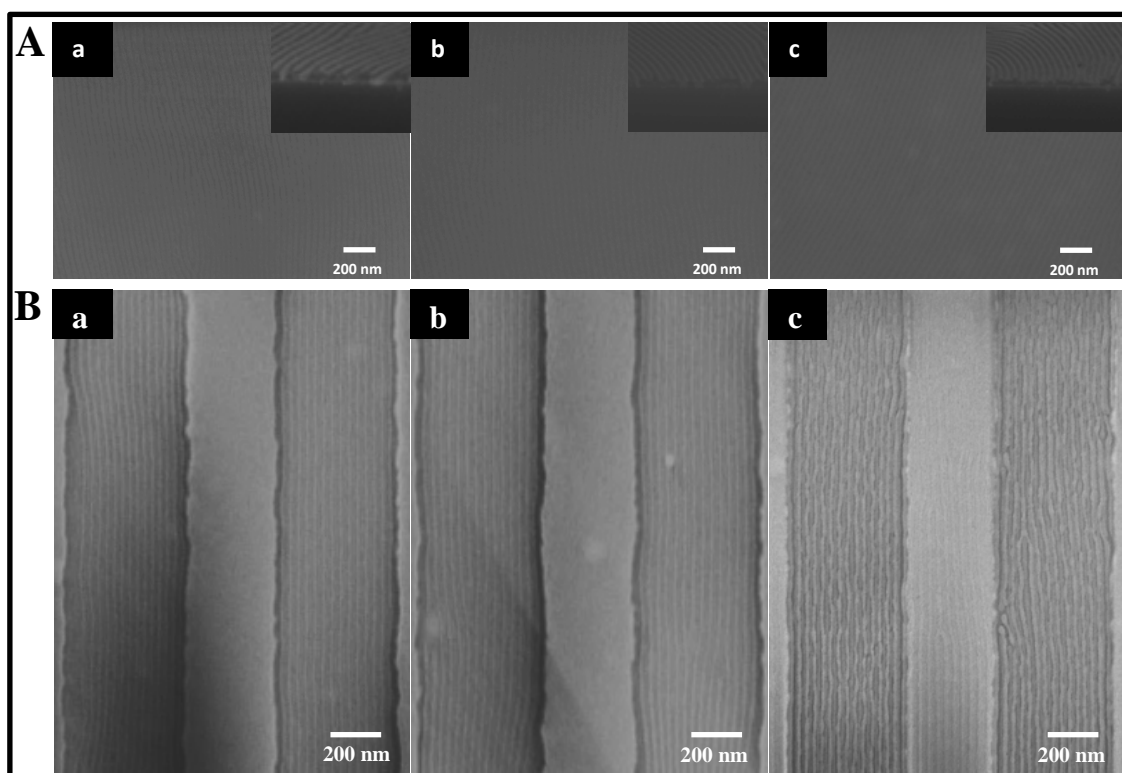


Figure 5.6. Top-down SEM images of *in-plane* PDMS cylinders on planar silicon substrates (**A**) and on patterned silicon substrates (**B**). The substrate was anchored with PDMS brush to get microphase separation of PS-*b*-PDMS film by solvent annealing in a saturated toluene environment for 3 h. The microphase separated PS-*b*-PDMS films were exposed to UV-O₃ for 5 min (**a**), 15 min (**b**) and 30 min (**c**) as an alternative to sequential CF₄ and O₂ plasma etches as detailed in the experimental section.

5.4.7. Pattern transfer to underlying substrate

In order to demonstrate the usefulness of the PS-*b*-PDMS system to generate substrate patterns an etch procedure for pattern transfer was developed (ETCH 2). The pattern transfer of PS-*b*-PDMS diblock copolymer to the substrate is not a straight forward process unlike the well-established polymer systems e.g., PS-*b*-PMMA [34, 35], PS-*b*-PEO [36], etc. This is because of the complex morphology of the PS-*b*-PDMS self-assembled patterns as described in the schematic in **Scheme 5.1**. The sequential pattern transfer process starts with the initial sequential CF₄ and O₂ plasma etches to remove the upper wetting PDMS layer and the PS matrix as well as oxidize the PDMS cylinders. These PDMS patterns now form silica-type structures which could act as a hard mask [34, 36]. Note that during the O₂ etch special care is required to minimize the undercut of the PDMS cylinders which can lead to poor quality pattern transfer. The pattern produced by the ETCH1

process was then treated with a CHF_3 and Ar plasma for 5 s in order to remove silica at the substrate surface and expose elemental silicon. This is a crucial process as an

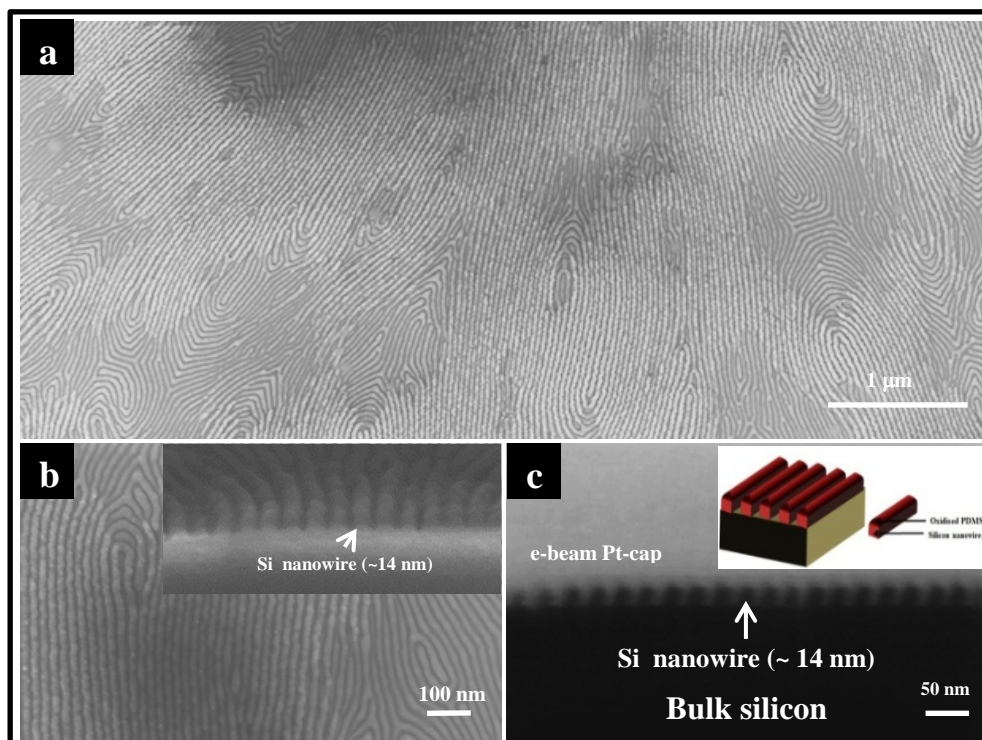


Figure 5.7. (a) Low resolution and (b) high resolution top-down SEM images of PDMS cylindrical patterns transferred to underlying planar silicon substrate (inset, (b) is the cross-section SEM image). (c) Focused Ion Beam (FIB)- cross-section SEM image of PDMS cylindrical patterns transferred to underlying silicon substrate (inset is the schematic showing oxidized PDMS cylinders on silicon nanowires). The pattern transfer was performed with a sequential CF_4 , O_2 , CHF_3/Ar and CHF_3/SF_6 plasma etches as detailed in the experimental section. The substrate was anchored with PDMS brush to get microphase separation of *PS-*b*-PDMS* film by solvent annealing in a saturated toluene environment for 3 h.

over-etch can compromise the structure of the silica produces from the PDMS structure. The silicon etch is performed for 15 s with CHF_3 and SF_6 gases to transfer the final BCP-derived pattern into the substrate. **Figure 5.7(a, b)** shows the top-down and cross-section SEM images of the silicon nanowires on planar silicon substrate obtained after the sequential etches. The cross-section SEM image shows the silicon nanowire structure that is produced via this complex etch procedure, has a feature size of ~ 14 nm with a feature height of ~ 26 nm. The FIB cross-section SEM image shown in **Figure 5.7(c)** gives a more detailed view of the fabricated silicon

nanowires and the schematic in inset, **Figure 5.7(c)** gives a simple representation of the structure. The nanoscale silicon features on the substrate surface are slightly narrower in width than that of the initial oxidized PDMS cylinders due to a partly isotropic etch process. The aspect ratio of the features was ~ 1.3 . The top-down and cross-section SEM images of the silicon nanowires on the topographically patterned silicon substrates obtained after pattern transfer are shown in **Figure 5.8(a, b)**.

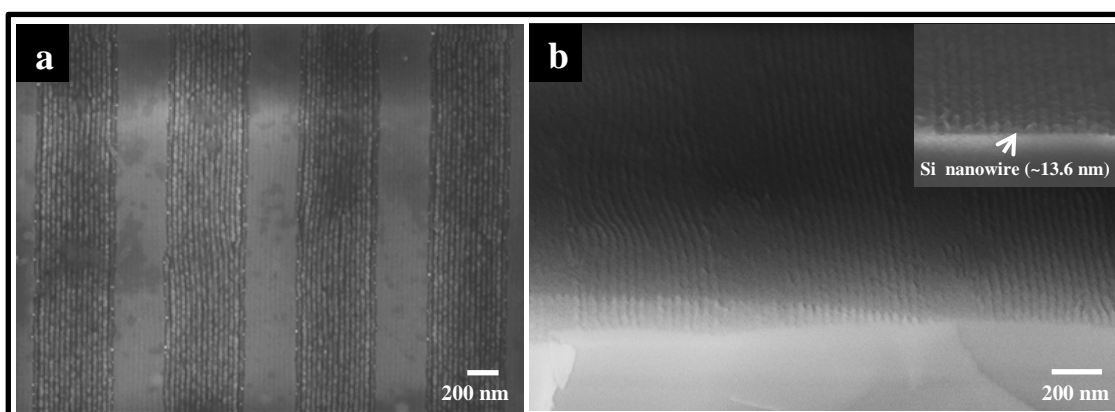


Figure 5.8. (a) Top-down low resolution and (b) tilted SEM images of PDMS cylindrical patterns transferred to underlying patterned silicon substrate (inset, (b) is the cross-section SEM image). The substrate was anchored with PDMS brush to get microphase separation of PS-*b*-PDMS film by solvent annealing in a saturated toluene environment for 3 h. The pattern transfer was performed with a sequential CF_4 , O_2 , CHF_3/Ar and CHF_3/SF_6 plasma etches as detailed in the experimental section.

The silicon nanowires are highly aligned within the channel and appear to be smooth. The cross-section SEM images (**Figure 5.8(b)** and **inset image**) show that the pattern transfer process is successful in the patterned substrates with line width of ~ 13.6 nm and a pattern depth of ~ 25.3 nm- consistent with the results of planar substrate.

5.5. Conclusions

A simple process for producing BCP films of uniform thickness across macroscopic distances is described. It allows these highly uniform films to be produced over substrates in macroscopic scale and could be applicable to wafer production. It is shown that the surface chemistry tuning also allows directed self-assembly with good degree of translation alignment of the PDMS domains. The average PDMS cylinder spacing, L_0 , and line width, $\langle d \rangle$, are found to be 33.4 nm

and 16.2 nm, respectively. The in-plane PDMS cylinders were used as etch mask to transfer the BCP pattern into underlying silicon with silicon nanowire line width of ~ 14.0 nm and a pattern depth of ~ 26.0 nm

5.6. References

- [1] C. A. Mack, *IEEE T Semiconduct M.* **2011**, 24, 202.
- [2] M. Freebody, *Photon Spectra* **2011**, 45, 45.
- [3] M. Wissen, N. Bogdanski, S. Moellenbeck, H. C. Scheer, *In Strategies for Hybrid Techniques of UV Lithography and Thermal Nanoimprint* **2008**.
- [4] S. Chung, J. R. Felts, D. Wang, W. P. King, J. J. De Yoreo, *Appl. Phys. Lett.* **2011**, 99, 193101.
- [5] A. E. Grigorescu, C. W. Hagen, *Nanotechnology* **2009**, 20, 292001.
- [6] H. Namatsu, Y. Watanabe, K. Yamazaki, T. Yamaguchi, M. Nagase, Y. Ono, A. Fujiwara, S. Horiguchi, *J. Vac. Sci. Technol. B* **2003**, 21, 1.
- [7] Y. Hirai, S. Hafizovic, N. Matsuzuka, J. G. Korvink, O. Tabata, *J. Microelectromech. S.* **2006**, 15, 159.
- [8] I. W. Hamley, *Angew. Chem. Int. Edit.* **2003**, 42, 1692.
- [9] P. Kumar, *Nanoscale Res. Lett.* **2010**, 5, 1367.
- [10] K. Ariga, J. P. Hill, M. V. Lee, A. Vinu, R. Charvet, S. Acharya, *Sci. Technol. Adv. Mater.* **2008**, 9, 014109.
- [11] C. J. Hawker, T. P. Russell, *MRS Bull.* **2005**, 30, 952.
- [12] L. J. Guo, *Adv. Mater.* **2007**, 19, 495.
- [13] B. D. Gates, Q. Xu, M. Stewart, D. Ryan, C. G. Willson, G. M. Whitesides, *Chem. Rev.* **2005**, 105, 1171.
- [14] T. Mårtensson, P. Carlberg, M. Borgström, L. Montelius, W. Seifert, L. Samuelson *Nano Lett.* **2004**, 4, 699.
- [15] S. Y. Chou, P. R. Krauss, P. J. Renstrom, *Appl. Phys. Lett.* **1995**, 67, 3114.
- [16] H. -W. Li, W. T. S. Huck, *Nano Lett.* **2004**, 4, 1633.

- [17] R. A. Farrell, N. Kehagias, M. T. Shaw, V. Reboud, M. Zelsmann, J. D. Holmes, C. M. Sotomayor Torres, M. A. Morris, *ACS Nano* **2011**, 5, 1073.
- [18] M. Salaün, N. Kehagias, B. Salhi, T. Baron, J. Boussey, C. M. Sotomayor Torres, M. Zelsmann, *J. Vac. Sci. Technol. B* **2011**, 29, 06F208.
- [19] T. H. Kim, J. Hwang, H. Acharya, C. Park, *J. Nanosci. Nanotechnol.* **2010**, 10, 6883.
- [20] M. Vayer, M. A. Hillmyer, M. Dirany, G. Thevenin, R. Erre, C. Sinturel, *Thin Solid Films* **2010**, 518, 3710.
- [21] N. Politakos, E. Ntoukas, A. Avgeropoulos, V. Krikorian, B. D. Pate, E. L. Thomas, R. M. Hill, *J. Poly. Sci. Part B Polym. Phys.* **2009**, 47, 2419.
- [22] S. M. Park, X. Liang, B. D. Harteneck, T. E. Pick, N. Hiroshiba, Y. Wu, B. A. Helms, D. L. Olynick, *ACS Nano* **2011**, 5, 8523.
- [23] Y. S. Jung, C. A. Ross, *Nano Lett.* **2007**, 7, 2046.
- [24] V. S. D. Voet, T. E. Pick, S. -M. Park, M. Moritz, A. T. Hammack, J. J. Urban, D. F. Ogletree, D. L. Olynick, B. A. Helms, *J. Am. Chem. Soc.* **2011**, 133, 2812.
- [25] D. Gentili, G. Foschi, F. Valle, M. Cavallini, F. Biscarini, *Chem. Soc. Rev.* **2012**, 41, 4430.
- [26] R. Mukherjee, M. Gonuguntla, A. Sharma, *J. Nanosci. Nanotechnol.* **2007**, 7, 2069.
- [27] T. H. Andersen, S. Tougaard, N. B. Larsen, K. Almdal, I. Johannsen, *J. Electron Spectrosc. Relat. Phenom.* **2001**, 121, 93.
- [28] C. M. Chan, *Polymer Surface Modification and Characterization*, 1st ed., Hanser Publishers: Munich, **1994**.
- [29] C. T. Kirk, *Physical Review B*. **1998**, 38, 1255.
- [30] K. V. Bernaerts, F. E. Du Prez, *Polymer* **2005**, 46, 8469.
- [31] Y. S. Jung, W. C. Jung, H. L. Tuller, C. A. Ross, *Nano Lett.* **2008**, 8, 3776.
- [32] A. Andreozzi, E. Poliani, G. Seguni, M. Perego, *Nanotechnology* **2011**, 22, 185304.
- [33] J. W. Jeong, W. I. Park, L. -M. Do, J. -H. Park, T. -H. Kim, G. Chae, Y. S. Jung, *Adv. Mater.* **2012**, 24, 3526.

-
- [34] D. Borah, M. T. Shaw, S. Rasappa, R. A. Farrell, C. T. O'Mahony, C. M. Faulkner, M. Bosea, P. Gleeson, J. D. Holmes, M. A. Morris, *J. Phys. D: Appl. Phys.* **2011**, *44*, 174012.
- [35] R. A. Farrell, N. Petkov, M. T. Shaw, V. Djara, J. D. Holmes, M. A. Morris, *Macromolecules* **2010**, *43*, 8651.
- [36] T. Ghoshal, T. Maity, J. F. Godsell, S. Roy, M. A. Morris, *Adv. Mater.* **2012**, *24*, 2390.

6.1. Abstract

Chapter 6 deals with the fabrication of ultrathin silicon nanowires (SiNWs) on a silicon-on-insulator (SOI) substrate as an electrode for the electro-oxidation and sensing of ethanol. The nanowire surfaces were prepared by a block copolymer (BCP) nanolithographic technique using low molecular weight symmetric poly(styrene)-*block*-poly(methyl methacrylate) (PS-*b*-PMMA) to create a nanopattern which was transferred to the substrate using plasma etching. The BCP orientation was controlled using a hydroxyl-terminated random polymer brush of poly(styrene)-random-poly(methyl methacrylate) (HO-PS-*r*-PMMA) as discussed in **Chapter 2**. TEM cross-sections of the resultant SiNWs indicate an anisotropic etch process with nanowires of sub-10 nm feature size. The SiNWs obtained by etching show high crystallinity and there is no evidence of defect inclusion or amorphous region production as a result of the pattern transfer process. The high density of SiNWs at the substrate surface allowed the fabrication of a sensor for cyclic voltammetric detection of ethanol. The sensor shows better sensitivity to ethanol and faster response time compared to widely used polymer nanocomposite based sensors.

6.2. Introduction

Semiconductor nanowires are currently attracting much attention as components for various nanoelectronic applications including field effect transistors [1], photonic and optoelectronic devices [2] and as chemical or biological sensors [3-5]. The high surface area to volume ratio of *1-D* semiconductor nanowires makes them excellent candidates for sensing applications, since a high surface to volume ratio improves detection sensitivity and response time due to increased reaction area per volume and reduced diffusion time [6, 7]. The operating principle of nanowire based chemical sensors is the detection of low molecular concentrations by measuring changes in the electrical conductance of nanowires produced by the adsorption or reaction of the chemical species. The cyclic voltammetry (CV) method extensively used in sensor design offers detection with high sensitivity and selectivity with relative ease, which derives

intrinsically from the species-dependent redox potentials.

Materials (biocompatible materials, gases and chemicals etc.) used for sensing purposes are generally polymer nanocomposites into which are incorporated conducting or semiconducting materials such as carbon nanotubes [8-10], metal nanoparticles [11, 12] and conducting polymer films [13, 14]. Silicon nanowires (SiNWs) have a very high surface area to volume ratio that enhances the efficiency of electrocatalytic reactions that can occur at the surface [15]. Thus, the fabrication of arrays of SiNWs has potential for the development of high sensitivity electrochemical sensors and they have become the subject of intense research. Lieber *et al.* reported the first application of SiNWs in this area [3]. Whilst silicon wires are promising, their manufacture by UV or other lithographies is expensive for low cost sensor applications and researchers are using different methods for synthesizing ultra-high density 1-D SiNWs cost-effectively. Ideally, the synthesis process should be compatible with established Si technology. This allows the integration of a SiNW based sensor into a single package for detection and signal processing.

SiNWs prepared by “top-down approaches” using various advanced methods such as X-ray [16], UV [17], and e-beam [5], based lithography has the advantage of strict dimension and structure control but at high cost. “Bottom-up approaches” of synthesizing SiNWs usually employ metal assisted catalytic growth (e.g. VLS (Vapor-Liquid-Solid) methods [18]) but using this methodology is challenging in terms of defining regular nanowire arrays that maximize surface area and provide robust structures. However, the bottom-up approach of block copolymer (BCP) lithography based on self-assembly is a potential method for the fabrication of SiNW arrays [19, 20] and could be used to develop sub-10 nm nanowire diameters. Since this technique involves low-cost processing and generate regular or semi-regular structures that can be onward processed relatively easily, they might provide a simple fabrication method for generating groups of individually addressable nanowire sensor arrays on a die and so enable the a single device to sense a range of chemicals. This chapter illustrates the potential of this approach.

6.3. Materials and methods

6.3.1. Materials

A hydroxyl-terminated random copolymer composed of styrene (S) and methyl methacrylate (MMA), denoted as HO-PS-*r*-PMMA and a lamellae-forming PS-*b*-PMMA BCP with Φ_{PS} of 0.50 were purchased from Polymer Source, Inc., Canada, and used as received. Their detailed characteristics are compiled in **Table 6.1**. The substrates were highly *p*-doped silicon-on-insulator (SOI) samples with resistivity, $\rho = 1\text{--}4 \text{ } \Omega \text{ cm}$ and a 20 nm device silicon layer separated by a 120 nm thick buried oxide (SiO₂) layer from the bulk silicon. Sulfuric acid, hydrogen peroxide, ethanol, acetone, iso-propanol (IPA) and toluene were purchased from Sigma-Aldrich and used without further purification unless otherwise stated. De-ionised (DI) water was used wherever necessary.

Table 6.1. Characteristics of polymers used for present study.

$M_n / \text{g mol}^{-1}$	Designation	Polydispersity index, M_w/M_n	PS mole fraction, %
12,400	HO-PS- <i>r</i> -PMMA	1.25	0.58
36,000	PS- <i>b</i> -PMMA	1.07	0.46

6.3.2. Polymer brush deposition

Substrates were cut into 2.0 cm² pieces and then degreased by ultrasonication in acetone and IPA solutions for 5 min each, dried in flowing N₂ gas and baked for 2 min at 393 K in an ambient atmosphere to remove any residual IPA. This was followed by cleaning in a piranha solution (1:3 v/v 30% H₂O₂:H₂SO₄ - **CAUTION! May cause explosion in contact with organic material!**) at 363 K for 60 min, rinsed with DI water, acetone, ethanol and dried under N₂ flow. A hydroxyl-terminated polymer brush solution of 1.0 wt. % in toluene was spin-coated (P6700 Series Spin-coater, Speciality Coating Systems, Inc., USA) onto substrates at 3000 rpm for 30 s. Samples were annealed in a vacuum oven (Townson & Mercer EV018) at 443 K under vacuum (-100 kPa) for 6 h. This allows the end-functional hydroxyl groups of the polymer brushes to react via

condensation with silanol groups at the silicon native oxide layer, resulting in polymer chain brushes anchored on the substrate. These methods have been described in detail by us earlier [19, 20]. Unbound polymers were removed by sonication (Cole-Palmer 8891 sonicator) and rinsing in toluene.

6.3.3. BCP film deposition

A BCP (PS-*b*-PMMA) solution of 1.0 wt. % in toluene was spin-coated onto the brush anchored surfaces at 3200 rpm for 30 s. Samples were annealed at 453 K under vacuum (-100 kPa) for 3 h, to induce phase separation and evaporate any remaining solvent. Thin films were removed from the oven immediately after annealing and allowed to cool naturally in ambient. This process and the products are described elsewhere [19, 20].

6.3.4. On-chip mask development and pattern transfer

Selective removal of PMMA block from the annealed PS-*b*-PMMA thin films on neutral polymer bushes was accomplished by inductively coupled plasma (ICP) etching in a OIPT Plasmalab System 100 ICP180 with an Ar/O₂ etch recipe of Ar (5 sccm) and O₂ (15 sccm) at 1.3 Pa and 100 W for 6 s to generate PS on-chip masks by selective removal of the PMMA block. An SF₆/CHF₃ ICP etch was then used to transfer the template structure to underlying substrate by selective removal of the silicon. Conditions were a 2.0 Pa pressure, 500 W SF₆ (15 sccm) and CHF₃ (80 sccm) etch for 9 s. Remaining PS was removed using an O₂ ash recipe at 2.0 Pa and 2000 W with 30 sccm O₂ for 10 s. Full details are given elsewhere [19-21].

6.3.5. Characterization of materials

BCP film thickness was measured by spectroscopic ellipsometry (Plasmos SD2000 Ellipsometer). An average of three readings collected from different locations on a sample surface was reported as the film thickness. An Atomic Force Microscope (DME 2452 DualScope Scanner DS AFM) was operated in AC (tapping) mode under ambient conditions using silicon microcantilever probe tips with a force constant of 60,000 N m⁻¹ and a scanning force of 0.11 nN. Topographic and phase images were recorded simultaneously. Fast Fourier Transforms (FFT) of the topographic images was used to measure the degree of

alignment and the presence of defects/non-regular patterns. Top-down and cross-sectional electron microscope images were obtained by a high resolution (< 1 nm) Field Emission Zeiss Ultra Plus- Scanning Electron Microscope (SEM) with a Gemini[®] column operating at an accelerating voltage of 5 kV. An FEI Strata 235-Focused Ion Beam (FIB) tool with resolution up to 10 nm was used for cross-sectional analysis. E-beam platinum was deposited above the nanowire patterns followed by the ion-beam platinum. Milling and polishing of the protective coatings were performed at the lower aperture size and then the specimen was imaged under the higher resolution Zeiss Ultra Plus- SEM. The transmission electron microscope (TEM) lamella specimens were prepared by the Zeiss Auriga-Focused Ion Beam with a Cobra ion column having a 2.5 nm resolution and were analysed by an FEI Titan-TEM operating at an accelerating voltage of 130 kV to obtain cross-sectional images of the silicon nanowires. Energy filtered TEM cross-section images of SiNWs for carbon, oxygen and silicon elemental distribution were also recorded.

6.3.6. Electro-oxidation of ethanol by the SiNW structure

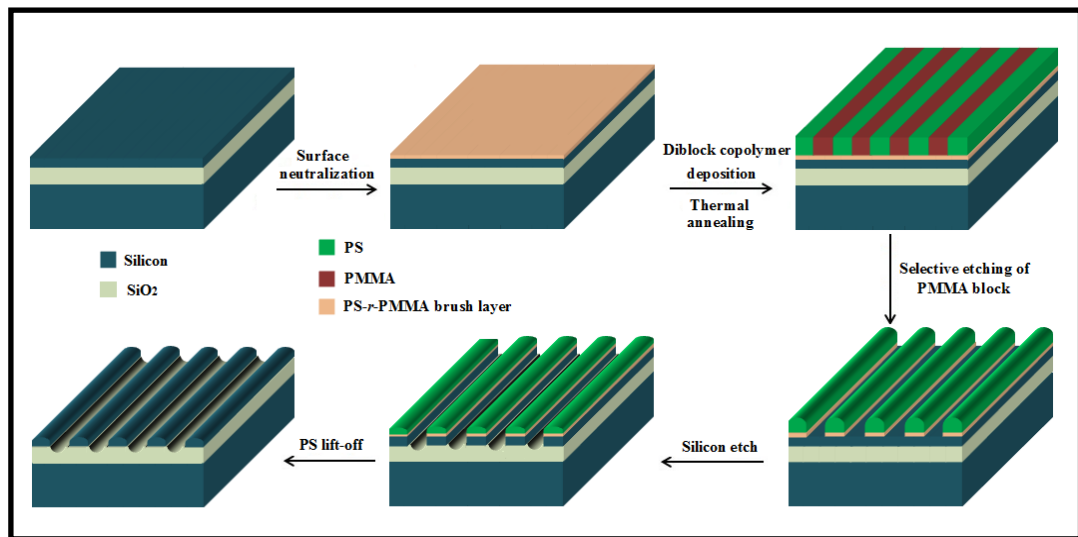
The electrochemical experiments were performed at (293 ± 1) K and prior to experiments solutions were de-aerated by bubbling nitrogen for 30 min. The cyclic voltammetric curves for electro-oxidation of ethanol were measured in a 0.5 M phosphate buffer solution (pH= 7.4) in the potential range of -0.8 and 1.0 V containing ethanol with a platinum foil counter electrode and a saturated Ag/AgCl and KCl as reference electrode in a VersaSTAT 3 (Princeton Applied Research, USA) potentiostat tool that includes the VersaStudio software for quantification of results.

6.4. Results and discussions

6.4.1. Fabrication of SiNW structure from BCP thin films

The symmetric PS-*b*-PMMA thin films prepared on a neutral polymer brush layer exhibit a lamellar morphology upon microphase separation and consist of alternating stripes of PS and PMMA due to the individual domains being oriented perpendicular to the substrate. A schematic showing the fabrication of

SiNWs from microphase separated PS-*b*-PMMA (18k-18k) film on the SOI substrate anchored with a random HO-PS-*r*-PMMA polymer brush is presented in **Scheme 6.1**. Removal of the PMMA block produces the PS line structure shown in top-down and cross-section SEM images (**Figure 6.1(a, b)**, respectively). The PS stripe width can be determined at ~12 nm and a height of ~19 nm from the SEM and FIB data. The lamellae repeat distance was ~26 nm for this BCP system. It can be seen that the pattern exhibits a high degree of domain alignment. It is suggested that this degree of alignment is associated with high levels of molecular motion during thermal annealing associated with a lower molecular weight compared to higher molecular weight systems [21]. Top-down SEM images of SiNWs pattern transferred to the SOI substrate is presented in **Figure 6.2 (a, b)**. An etch time of 9 s was found to be optimum for pattern transfer providing the highest quality features as reported earlier [19, 21]. The BCP derived



Scheme 6.1. Details of the fabrication of SiNWs from microphase separated PS-*b*-PMMA (18k-18k) film on SOI substrate anchored with a random HO-PS-*r*-PMMA polymer brush.

topographically patterned substrates now consist of a uniform coverage of silicon lines that are parallel and aligned over several micron. The silicon nanowire feature size as measured from the SEM image is about 8.7 nm. The fidelity of the pattern transfer can, however, be more directly observed using TEM cross-section as presented in **Figure 6.3(a, b)**. It can be seen that the pattern transfer has occurred

such that the etch penetrates significantly into the insulating silica layer as suggested by the localization of the single crystal region towards the top of the features. The features widths at the base agree reasonably well with the SEM data presented in **Figure 6.2(a, b)**. As can be seen in the images (**Figure 6.3(a, b)**), the pattern transferred silicon shows little sign of

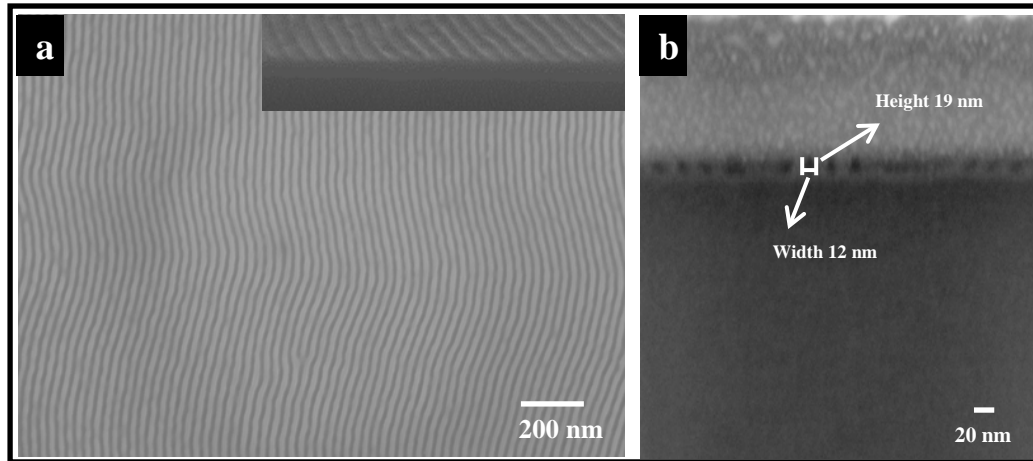


Figure 6.1. (a) Top-down SEM image of the PS template after selective plasma etching of PMMA block of the microphase separated PS-*b*-PMMA (18k-18k) film on SOI substrate, anchored with a random HO-PS-*r*-PMMA polymer brush. Inset in (a) is the 20° tilted SEM cross-section image. (b) FIB cross-section SEM image of PS template.

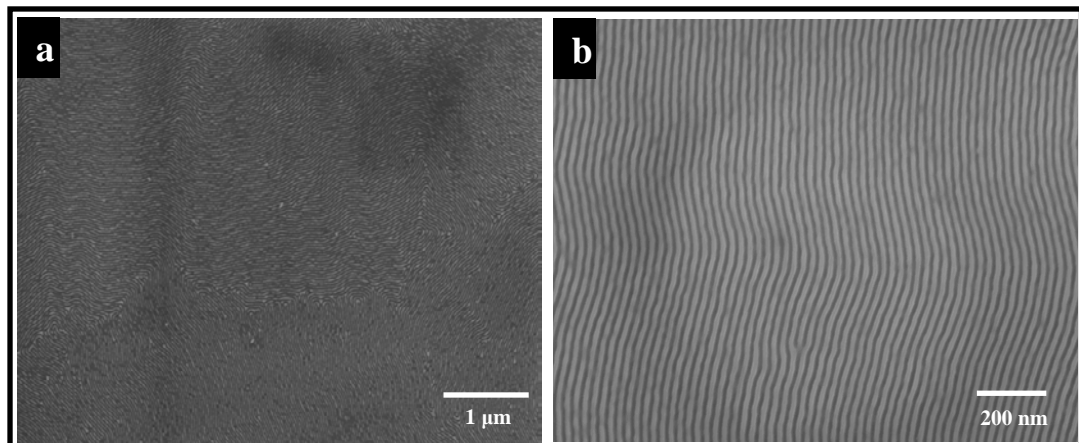


Figure 6.2. Low resolution (a) and high resolution (b) top-down SEM images of SiNWs fabricated using PS mask by etch pattern transfer.

physical damage. Note, in particular, that the silicon features obtained by etching show high crystallinity with lattice planes clearly resolved in the TEM images

(Figure 6.3(c)). There is no evidence of defect inclusion or amorphous region formation as a result of the pattern transfer process. In an ideal pattern transfer process, the nanowire size should be around that of the PS line width (since this is about half the pitch size). This was not observed and etch anisotropy as well as over etch

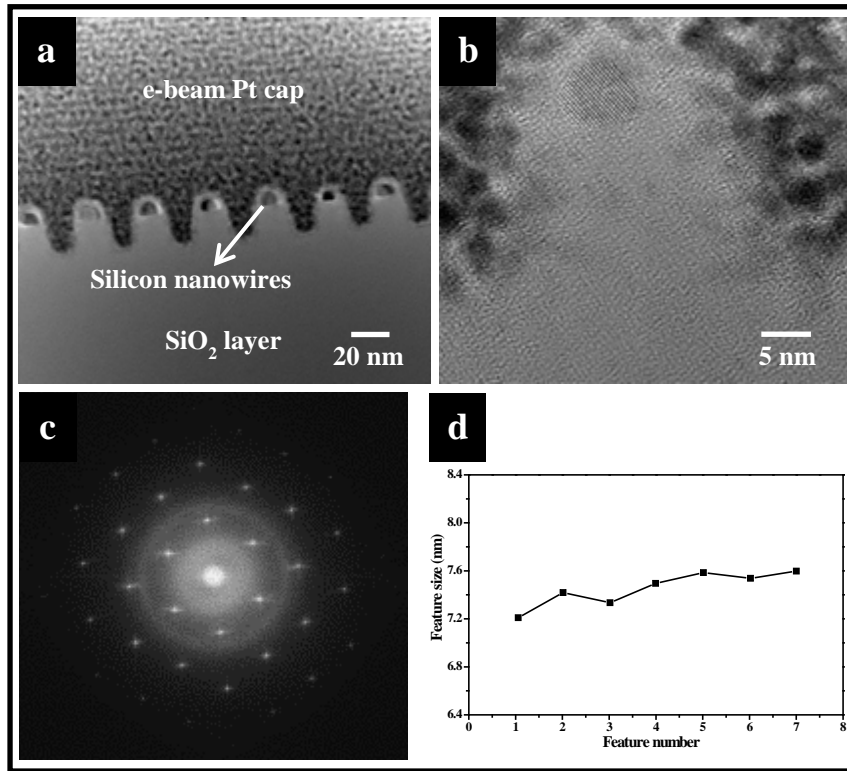


Figure 6.3. (a) TEM cross-section image of SiNWs fabricated as described in the text. (b) Expansion of the data shown in (a), and is a high resolution TEM image of same showing the silicon lattice planes present in the features. (c) Small area electron diffraction (SAED) pattern of a single SiNW feature also illustrating the crystallinity of the etched material. (d) Statistical feature size (nm) diagram of SiNWs against feature number. This is a representative sample and the mean size of 7.35 nm (+/- 0.25 nm (3 σ)) can be measured using large data.

ensured that the feature size was less than the polymer half pitch as shown in the statistical size distribution diagram shown in Figure 6.3(d). A full explanation of the etch limitations and effects is given elsewhere [19]. The SiNWs fabricated on SOI substrate were further characterized by Energy Filtered Transmission

Electron Microscopy (EFTEM) in order to assess the impurity level and efficacy of the pattern transfer process. The results of carbon, oxygen and silicon mapping in the TEM cross-section images are displayed in **Figure 6.4(a, b, c)**. The EFTEM carbon mapping image (**Figure 6.4(a)**) suggests that the SiNWs are devoid of carbon within experimental detection limits. The lack of carbon suggests that the etch process removes all polymer components and the adsorption of carbon containing species is limited. Oxygen (**Figure 6.4(b)**) and silicon (**Figure 6.4(c)**) mapping images of the SiNWs indicate some oxidation of the crystalline silicon etched from the device layer. This is as expected following the final oxygen etch and the exposure to ambient conditions.

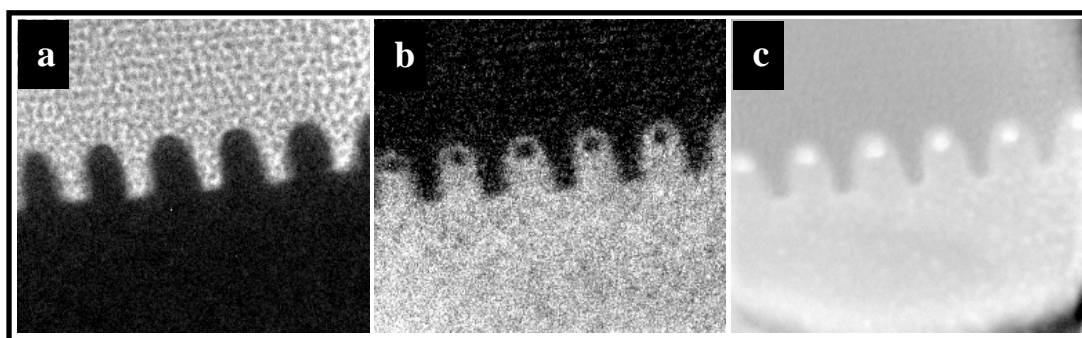


Figure 6.4. Energy filtered TEM cross-section images of SiNWs fabricated using PS template mask and etched into SOI substrate: (a) carbon; (b) oxygen and (c) silicon mapping. For each element white contrast denotes higher concentration of the element indicated.

6.4.2. Electro-oxidation of ethanol by the SiNW electrode

The electrochemical behaviour of the substrate and the nanowire surfaces in the absence and presence of ethanol is shown in **Figure 6.5**. For comparison, data are illustrated for samples in 0.5M phosphate buffer solution (pH = 7.4) and 0.5 M phosphate buffer solution (pH = 7.4) with an addition of 0.2 M ethanol. The non-patterned substrate showed little response as expected from data above. It can be seen that apart from a very minor feature at about -0.05 V, there was no obvious peak observed for the nanowire surface in the phosphate buffer alone. However, with addition of ethanol, prominent oxidation and reduction peaks can be observed, thus, demonstrating the electrocatalytic property of the SiNWs.

The data reported are similar in form to current-voltage profiles reported in literature [22]. The ethanol oxidation peak was observed at ~ 0.1 V. This low oxidation potential is of note as it is significantly lower than that measured on other electrode platforms reported in literature [23-26].

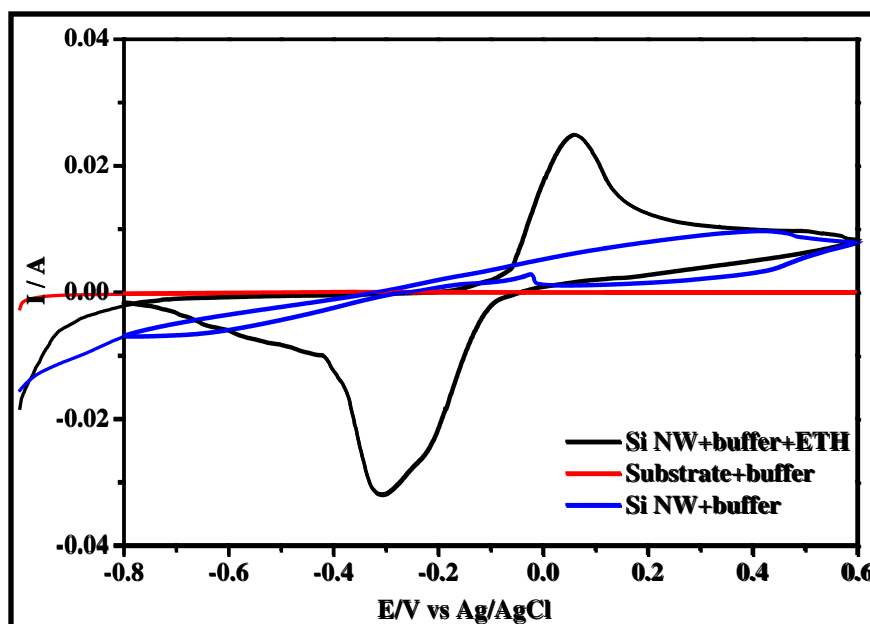
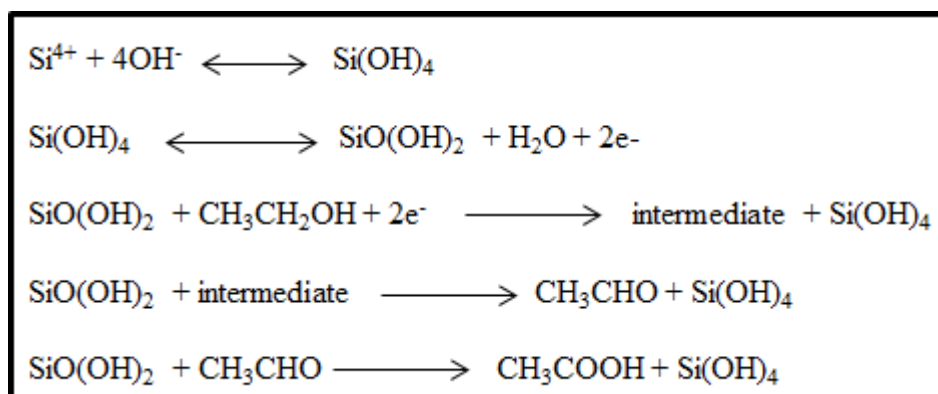


Figure 6.5. Comparative cyclic voltammograms showing the current response (in phosphate buffer) of the non-patterned SOI substrate electrode, a SiNW electrode and the same electrode in the presence of 0.2 M ethanol (0.5 M phosphate buffer solution (pH = 7.4) used in all data). As labeled in figure.

The functionality of the SiNW electrode towards ethanol oxidation is promising as a high current peak density and low energy (E/V) are observed [12]. Tao *et al.* have observed the same behaviour for ethanol oxidation on SiNWs decorated with palladium-nickel (Pd-Ni/SiNWs) although no precious metal component is used in this work [8]. It should be noted that the nature of the supporting electrolyte i.e. basic, acidic or neutral could be an important factor influencing the analyte oxidation potential. Ethanol electro-oxidation is a very complex reaction, in which several reaction products and intermediates can be formed *viz.*, species like CO , CO_2 , CH_3COO^- , CH_3CO , CH_3CHO , and CH_3COOH during the forward oxidation process [8, 12, 27-30]. The reaction mechanism of the formation of the carbonaceous species under the electrochemical conditions is

illustrated in **Scheme 6.2** [8, 12, 31-24]. The Oxidation process is balanced by a reductive process where $\text{SiO}(\text{OH})_2$ (silicon hydroxide oxide) is reduced thereby reactivating the surface of the electrode. Experimentally (**Figure 6.5**), the oxidation of ethanol and other carbonaceous species is indicated by the presence of an intense anodic oxidation peak at -0.32 V. This feature is usually seen at about -0.45 V [8, 12] and the value recorded in the present work suggests an improved



Scheme 6.2. Ethanol oxidation reaction mechanism at the SiNW electrode.

electrocatalytic performance of the SiNW system. Factors that may be the cause of the superior electrocatalytic behavior of the SiNWs towards ethanol oxidation include: the high conductivity of the SiNWs, the uniform diameter of the nanowires, smooth exterior surface and the high available surface area across the substrate. The stability of the SiNW electrode on electrocatalytic oxidation of ethanol was investigated by varying the scan rate from 10 to 100 mVs^{-1} . The cyclic voltammetry experiment was carried out at constant concentration (0.2 M) of ethanol in 0.5 M phosphate buffer solution ($\text{pH} = 7.4$) and the results are presented in **Figure 6.6(a)**. From the CV data two important observations can be made: (1) irreversible electro-oxidation of ethanol is always seen and (2) the anodic current increase was more pronounced for the oxidation sweep compared to the reduction sweep. These observations suggest that the potential sweep favours electro-oxidation of the analyte. Further, the anodic peak current of the SiNW electrode in the ethanol solution increased linearly with increasing scan rate. This suggests that oxidation occurs through direct electron transfer between ethanol and the electrode on electrode surface as described in **Scheme 6.2**. The nature of the

redox process can be found from the Randles-Sevcik equation (**Equation 6.1**) for an anodic oxidation process [31] by plotting the peak current (anodic), I_p , against the square root of scan rate ($v^{1/2}$).

$$I_p = 3.01 \times 10^5 n[(1-\alpha)n_a]^{1/2} AC_b D^{1/2} v^{1/2} \quad (6.1)$$

where n is the number of exchange electrons, α is the electron transfer coefficient, A is the electrode surface area, C is the concentration coefficient of the analyte, and D is the diffusion coefficient of the analyte. The linear plot of

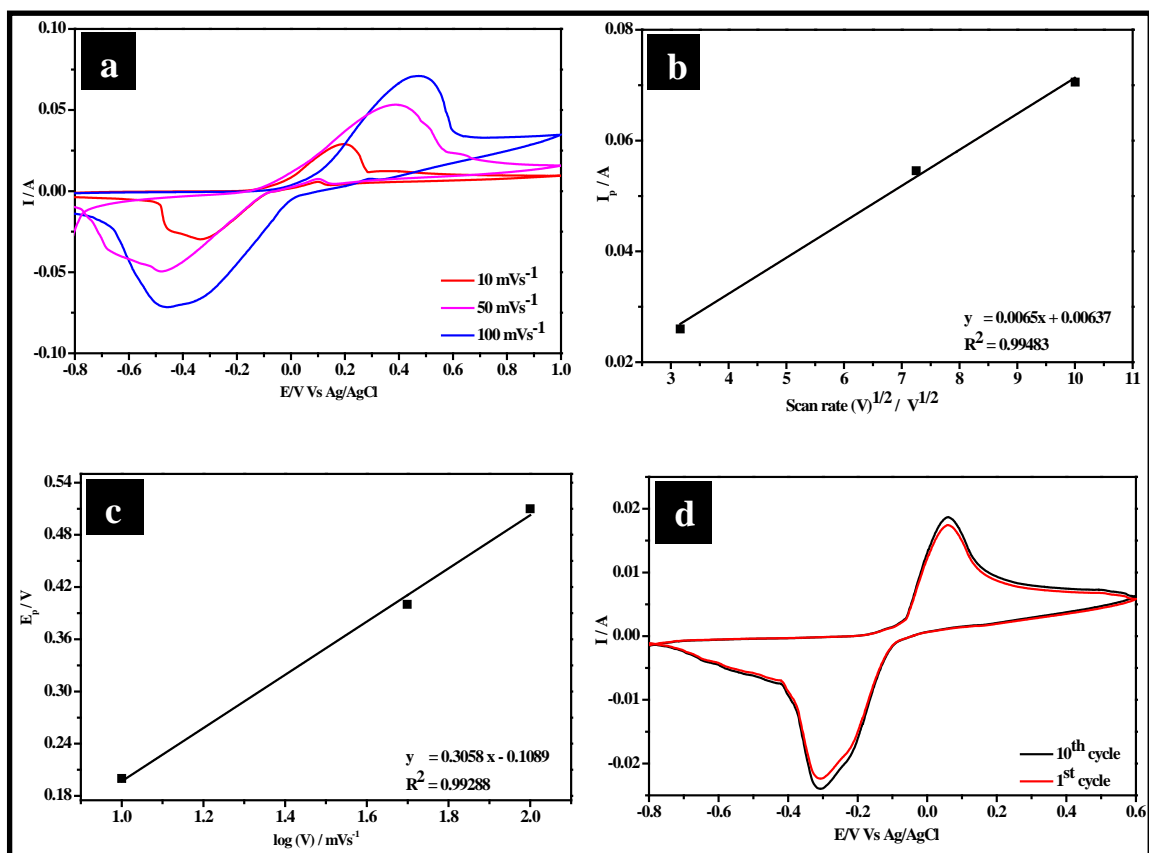


Figure 6.6. (a) Comparative cyclic voltammograms showing the current response of the SiNW electrode with 0.2 M ethanol in a 0.5 M phosphate buffer solution (pH = 7.4) at different scan rates. (b) Plot of I_p vs. $v^{1/2}$ for the anodic process. (c) Tafel plot of E_p vs. $\log v$ for the anodic process. (d) Multiple scanning (10 runs) of the SiNW electrode in 0.2 M ethanol phosphate buffer solution.

I_p vs. $v^{1/2}$ presented in **Figure 6.6(b)**, with a regression coefficient (R^2) value of 0.99483, suggests a diffusion controlled redox process [31-35]. The stability of the SiNW electrode in the electro-oxidation process can be ascertained from the plots of the peaks potential, E_p and the $\log v$ using the Tafel equation (**Equation 6.2**)

[31], given below:

$$E_p = b/2 (\log v) + \text{constant} \quad (6.2)$$

The plot of E_p against $\log v$ was found to be linear as shown in **Figure 6.6(c)**. The value of “b” was estimated from the slope of the Tafel plot and was found to be 621 mVdec^{-1} . Adekunle *et al.* reported a “b” value of 1227 mVdec^{-1} whilst investigating the ethanol electro-oxidation using a platinum-MWCNT-NiO electrode (note MWCNT = Multiwalled carbon nanotube) [36]. The value reported here is substantially lower and indicates a lower concentration of reaction intermediates on the SiNW electrode [31, 37]. This suggestion is further supported by lower anodic potential (-0.32 V) observed in this work (**Figure 6.5**). The multiple scanning of the SiNW electrode in 0.2 M ethanol is presented in **Figure 6.6(d)**. It should be noted that the scans were run up to 50^{th} cycles, however, the scans were overlapped after 10^{th} cycles and, therefore, omitted for clarity in the figure. It was found that a minor rise in current (1.5%) existed between the first and the second scan but for later scans there was no significant changes in CV curves and suggest high stability of the system.

The cyclic voltammetry method was used to investigate the response of the SiNW electrode to different concentrations of ethanol in 0.5 M phosphate buffer and results are presented in **Figure 6.7(a)**. It can be noted that during forward sweeping, the oxidation peak currents increases from 11.3 to 60.6 mA and the oxidation peak potential shifts from 0.21 to 0.38 V with the increase in ethanol concentration. It occurs because of the electrode polarization. With increasing ethanol concentration, the potential of the Si^{2+} reduction peak and the carbonaceous species oxidation peak, is shifted to lower potential during the reverse sweep.

The relationship between the oxidation peak current values and ethanol concentration levels can be employed to quantify the concentration of ethanol present. A plot of current response against concentration is linear as described in **Figure 6.7(b)** and can be fitted as $I_p (\text{A}) = 0.34103 C (\text{M}) - 0.00242$ with a correlation coefficient of 0.99314 . The detection limit (DL) was estimated using the relationship $\text{DL} = 3.3 s/m$ [38], where s is the relative standard deviation of the

intercept and m , the slope of the linear current Vs ethanol concentration. The sensitivity, detection limit and the concentration range can be determined to be $0.08 \mu\text{AmM}^{-1}$, 7.64 mM and $11.3\text{-}200.0 \text{ mM}$, respectively, using the CV technique. The estimated DL value is low and comparable with literature values [39-41].

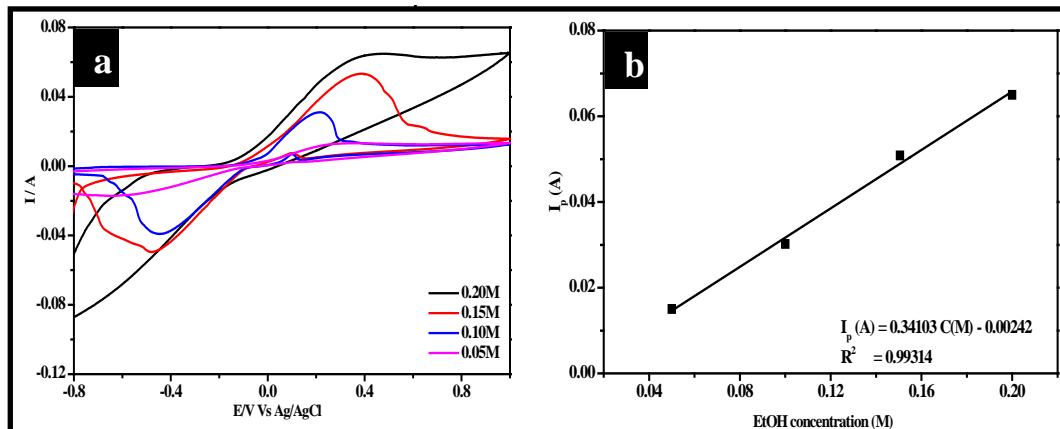


Figure 6.7. (a) Comparative cyclic voltammograms showing the current response of SiNW electrode in a 0.5 M phosphate buffer solution (pH = 7.4) at different concentrations of ethanol at a scan rate of 10 mVs^{-1} . (b) Plot of I_p vs. concentration of ethanol.

6.5. Conclusions

In summary, SiNWs fabricated on a highly *p*-doped SOI substrate using BCP methods show promise in ethanol sensing. This fabrication technique has advantages in being highly reproducible and relatively inexpensive. The simplicity of the processing used would offer cost advantages over traditional silicon fabrication methods. The products have good thermal and mechanical robustness compared to other self-assembly techniques. Good electrocatalytic behavior of the SiNW patterned substrates prepared here show potential for the quantification of ethanol in solution. This could be rationalized in terms of the high conductivity of the SiNWs, the monodispersity of the nanowire diameter, smooth surfaces as well as high available surface area. The results show a very high stability of the SiNW electrode, a lower level of adsorption of reaction intermediates and can withstand the CO poisoning. The low detection limit, the stability of the system and good signal-to-noise characteristics suggest that BCP patterned SiNW systems could be used to

fabricate devices for ethanol sensors and used in commercial applications.

6.6. References

- [1] J. Goldberger, A. I. Hochbaum, R. Fan, P. Yang, *Nano Lett.* **2006**, 6, 973.
- [2] C. Yang, C. J. Barrelet, F. Capasso, C. M. Lieber, *Nano Lett.* **2006**, 6, 2929.
- [3] Y. Cui, Q. Wei, H. K. Park, C. M. Lieber, *Science* **2001**, 293, 1289.
- [4] L. M. Lechuga, J. Tamayo, M. Alvarez, L. G. Carrascosa, A. Yufera, R. Doldan, E. Peralias, A. Rueda, J. A. Plaza, K. Zinoviev, C. Dominguez, A. Zaballos, M. Moreno, A. C. Martinez, D. Wenn, *Sens. Actuators B* **2006**, 118, 2.
- [5] Z. Li, Y. Chen, X. Li, T. I. Kamins, K. Nauka, R. S. Williams, *Nano Lett.* **2004**, 4, 245.
- [6] J. Huang, S. Virji, B. H. Weiller, R. B. Kaner, *Chem. Eur. J.* **2004**, 10, 1314.
- [7] D. Xie, Y. Jiang, W. Pan, D. Li, Z. Wu, Y. Li, *Sens. Actuators B* **2002**, 81, 158.
- [8] B. Tao, J. Zhang, S. Hui, L. Wan, *Sens. Actuators B* **2009**, 142, 298.
- [9] Y. Ma, S. R. Ali, A. S. Dodoo, H. He, *J. Phys. Chem. B* **2006**, 110, 16359.
- [10] K. I. Ozoemena, T. Nyokong, D. Nkosi, I. Chambrier, M. J. Cook, *Electrochim. Acta* **2007**, 52, 4132.
- [11] E. A. Batista, G. R. P. Malpass, A. J. Motheo, T. Iwasita, *Electrochem. Commun.* **2003**, 5, 843.
- [12] R. G. Freitas, M. C. Santos, R. T. S. Oliveira, L. O. S. Bulhoes, E. C. Pereira, *J. Power Sources* **2006**, 158, 164.
- [13] G. M. Morales, H. J. Salavagione, D. E. Grumelli, M. C. Miras, C. A. Barbero, *Polymer* **2006**, 47, 8272.
- [14] T. F. Kang, G. L. Shen, R. Q. Yu, *Anal. Chim. Acta* **1997**, 356, 245.
- [15] N. Elfstrom, R. Juhasz, I. Sychugov, T. Engfeldt, A. E. Karlstrom, J. Linnros, *NanoLett.* **2007**, 7, 2608.
- [16] Y. Hirai, S. Hafizovic, N. Matsuzuka, J. G. Korvink, O. Tabata, *J. Microelectromech. S.* **2006**, 15, 159.
- [17] L. Yang, D. H. Lee, H. Y. Chen, C. Y. Chang, S. D. Liu, C. C. Huang, *VLSI Symp. Tech. Dig.* **2004**, 196.
- [18] T. I. Kamins, R. S. Williams, Y. L. Chang, Y. A. Chang, *Appl. Phys. Lett.* **2000**,

76, 562.

[19] D. Borah, M. T. Shaw, S. Rasappa, R. A. Farrell, C. C. O'Mahony, C. M. Faulkner, M. Bosea, P. Gleeson, J. D. Holmes, M. A. Morris, *J. Phys. D Appl. Phys.* **2011**, *44*, 174012.

[20] R. A. Farrell, N. T. Kinahan, S. Hansel, K. O. Stuen, N. Petkov, M. T. Shaw, L. E. West, V. Djara, R. J. Dunne, O. G. Varona, P. Gleeson, S. –J. Jung, H. –Y. Kim, M. M. Kolesnik, T. Lutz, C. P. Murray, J. D. Holmes, P. F. Nealey, G. S. Duesberg, V. K. Krstić, M. A. Morris, *Nanoscale* **2012**, *4*, 3228.

[21] S. Rasappa, D. Borah, R. Senthamaraiannan, C. C. Faulkner, M. T. Shaw, P. Gleeson, J. D. Holmes, M. A. Morris, *Thin Solid Films* **2012**, *522*, 318.

[22] N. Spataru, X. Zhang, T. Spataru, D. A. Tryk, A. Fujishima A, *J. Electrochem. Soc. B* **2008**, *155*, 264.

[23] Z. –Hwang, J. Li, X. Dong, D. Wang, T. Chen, H. Qiao, A. Huang, *Int. J. Hydrogen Energy* **2008**, *33*, 6143.

[24] R. B. Kutz, B. Braunschweig, P. Mukherjee, R. L. Behrens, D. D. Dlott, A. Wieckowski, *J. Catal.* **2011**, *278*, 181.

[25] S. M. A. Shibli, N. D. Suma, V. S. Dilimon, *Sens. Actuat. B* **2008**, *129*, 139.

[26] B. Ballarin, R. Seeber, D. Tonelli, A. Vaccari, *J. Electroanal. Chem.* **1999**, *463*, 123.

[27] F. Vigier, C. Coutanceau, F. Hahn, E. M. Belgsir, C. Lamy, *J. Electroanal. Chem.* **2004**, *563*, 81.

[28] G. A. Camara, R. B. D Lima, T. Iwasita, *J. Electroanal. Chem.* **2005**, *585*, 128.

[29] V. P. Santos, V. D. Colle, R. B. DLima, G. Tremiliosi-Filho, *Electrochim. Acta* **2007**, *52*, 2376.

[30] S. S. Gupta, J. Datta, *J. Electroanal. Chem.* **2006**, *594*, 65.

[31] A. J. Bard, L. R. Faulkner, *Electrochemical Methods: Fundamentals and Applications*; 2nd Ed., John Wiley & Sons: Hoboken, NJ, **2001**.

[32] S. Majdi, A. Jabbari, H. Heli, A. A. Moosavi-Movahedi, *Electrochim. Acta* **2007**, *52*, 4622.

[33] H. Yao, Y. Sun, X. Lin, Y. Tang, L. Huang, *Electrochim. Acta* **2007**, *52*, 6165.

[34] S. Jo, H. Jeong, S. R. Bae, S. Jeon, *Microchem. Journ.* **2008**, *88*, 1.

[35] X. Wang, N. Yang, Q. Wan, X. Wang, *Sens. Actuat. B.* **2007**, *128*, 83.

[36] A. S. Adekunle, O. S. Oluwafemi, V. Ncapayi, R. E. Sadiku, J. T. Agee, S. O. Ojo, S. P. ong, *Int. J. Electrochem. Sci.* **2012**, *7*, 2695.

[37] A. S. Adekunle, K. I. Ozoemena, *Int. J. Electrochem. Sci.* **2010**, *5*, 1972.

-
- [38] G. D. Christian, *Analytical Chemistry*; 6th Ed., John Wiley & Sons: New York, **2004**.
- [39] J. Gonzalo-Ruiz, M. A. Alonso-Lomill, R. Escude-Pujol, F. J. Munoz, *Electroanal.* **2006**, *18*, 1231.
- [40] E. Scavetta, D. Tonelli, *Electroanal.* **2005**, *17*, 363.
- [41] H. N. Choi, S. H. Yoon, Y. -K. Lyu, W. Y. Lee, *Electroanal.* **2007**, *19*, 459.

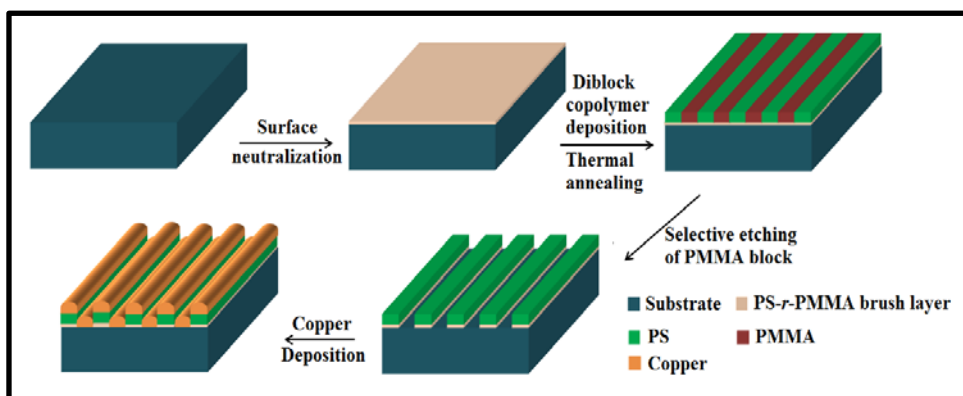
7.1. Abstract

Chapter 7 deals with novel material fabrication for high energy storage using a block copolymer PS-*b*-PMMA (18k-18k) template. The result described may represent a very significant advance in research of supercapacitor systems. Previous literature studies of electrical double layer phenomena reports capacitances up to only hundreds of F/g. The performance of metal-oxide supercapacitors has been improved by anchoring with materials like graphene sheets [1] and copper oxide [2] and these approaches have shown promise. Here, we demonstrate a new supercapacitor fabrication methodology based around the microphase separation of PS-*b*-PMMA [3] which has been used to generate copper nanoelectrodes of dimension ~13 nm. These structures provide excellent capacitive performance with a maximum specific capacitance of ~836 F/g for a current density of 8.06 A/g at a discharge current as high as 75 mA. The excellent performance is due to a high surface area to volume ratio. We suggest that this highly novel, easily fabricated structure might have a number of important applications.

7.2. Introduction

In recent years, electrochemical capacitors have dominated energy storage for various technologies [4]. These devices store energy (at electrode-electrolyte interfaces) as electrical charge and are properly described as Electric Double Layer Capacitors (EDLCs) or more generally supercapacitors (SCs). Nanodimensioned structures are a necessity for high density energy storage [5, 6]. The wide range of applications of these systems requires low cost fabrication, high performance and reliability. Various potential supercapacitor materials have been explored including transition metal oxides [7, 8], carbon materials [9] and conducting polymers [10, 11], etc. A range of top-down and bottom-up approaches to their nanofabrication are being developed [12-14] but bottom-up, or chemical self-assembly, methods may offer cost advantages (avoiding lithographic technology) and techniques such as surfactant mediated self-assembly [15], polymer sphere self-assembly [16] and anodic alumina templates [17] have been explored. Block copolymer (BCP) lithography methods [18-20] are promising nano-fabrication techniques used to generate surface

nanopatterns of sub-15 nm feature size but to our knowledge BCPs have not been used to make supercapacitor structures that have been electrically characterised. Here, we report the use of a PS (polystyrene) - PMMA (polymethylmethacrylate) BCP template for the fabrication of 3-D network structure of copper nanowires on a substrate and explore nanocapacitor device performance. A schematic diagram showing the fabrication of Cu nanowires using the BCP based technique is described in **Scheme 7.1**.



Scheme 7.1. Schematic diagram of the fabrication of Cu nanowires using PS template obtained from microphase separated PS-*b*-PMMA (18k-18k) film on SiO₂ substrate anchored with a random HO-PS-*r*-PMMA polymer brush.

7.3. Materials and methods

Hydroxy-terminated random HO-PS-*r*-PMMA copolymer (number-average molecular weight (M_n) and polydispersity (M_w/M_n) were 12.4 kg mol⁻¹ and 1.25 respectively) and a lamella-forming, symmetric PS-*b*-PMMA diblock copolymer ($M_n = 36$ kg mol⁻¹ and $M_w/M_n = 1.25$) were purchased from Polymer Source, Inc., Canada. The substrates used were (100) orientated silicon wafers with a native oxide layer of thickness 120 nm. Sulphuric acid, hydrogen peroxide, toluene and DMF were purchased from Sigma-Aldrich.

7.3.1. Development of diblock copolymer self-assembled patterns

Details about BCP self-assembly can be found in materials and methods section in 2.3.2 and 2.3.3 in **Chapter 2** and in Borah *et.al.* [3]. Substrates were cleaned in a piranha solution, rinsed with deionized water, and dried under N₂ flow.

A HO-PS-*r*-PMMA brush solution of 1.0 wt. % in toluene was spin-coated at 3000 rpm for 30 s and annealed in a vacuum oven (Townson & Mercer EV018) at 170 °C for 6 h. Non-chemically bound polymer was removed by sonication (Cole-Palmer 8891 sonicator) and rinsing in toluene (film thickness ca. 5 nm as measured by transmission electron microscopy (TEM)). Thin films of PS-*b*-PMMA were prepared by spin-coating the polymer solution of 1.0 wt. % in toluene onto the brush anchored surfaces at 3200 rpm for 30 s (film thickness ca. 45 nm as measured by ellipsometry). Samples were annealed at 180 °C under vacuum for 4 h, to induce phase separation and evaporation of any remaining solvent. Thin films were removed from the oven immediately after annealing, without any controlled cooling stage.

7.3.2. Preparation of diblock copolymer templates

Selective removal of PMMA block from the annealed PS-*b*-PMMA thin films on a neutral polymer bush was accomplished by plasma etching in a OIPT Plasmalab System 100 ICP180 with an Ar/O₂ etch recipe of Ar (5 sccm) and O₂ (15 sccm) at 10 mT and 100 W for 6 s to generate PS template mask structures. Full details are given in *Chapter 2* and in references [3, 22].

7.3.3. Development of capacitor structures

Copper was deposited by a thermal evaporation technique using Temescal FC-2000 evaporation system on the PS templates generated by selectively removing PMMA block. The deposition rate was $\sim 1 \text{ Å s}^{-1}$ as measured by the evaporation of a 13 nm copper film on a flat substrate using an evaporation period of 120 s. The evaporation was performed to generate an over-deposition of copper so that all of the PS topography was filled.

7.3.4. Characterization of materials

Diblock copolymer thin film thickness was determined by ellipsometry (Plasmos SD2000 Ellipsometer). Powder X-ray diffraction (XRD) measurements were performed with a Philips X'Pert diffractometer using Cu K_α radiation with an anode current of 40 mA and an accelerating current of 40 kV. Top-down and cross-sectional Scanning Electron Microscope (SEM) images of polymer templates and copper nanowires were obtained by a high resolution (< 1 nm) Field Emission Zeiss Ultra Plus Scanning Electron Microscope with a Gemini[®] column operating at an

accelerating voltage of 5 keV. Elemental analysis via energy dispersive X-ray analysis (EDAX) of the copper samples was carried out using an Oxford Instruments INCA tool at an operating voltage of about 20 keV. Transmission Electron Microscope (TEM) imaging was achieved by e-beam platinum deposition onto the nanowire patterns followed by ion-beam platinum deposition. This double deposition allowed good in-fill of the sample and protected the films during cross-section preparation. Milling and polishing of the protective coatings was carried out in a Zeiss Auriga Focused Ion Beam (FIB) with a Cobra ion column and were subsequently analysed by a FEI Titan-Transmission Electron Microscope operating at an accelerating voltage of 130 keV.

7.3.5. Electrochemical characterization of copper nanowires

AC impedance and current-voltage (I - V) characteristics of the copper nanowire structures were performed in a three electrode electrochemical cell set-up consisting of a working electrode, a reference electrode and a counter electrode along with the electrolytic solution. The copper nanowires fabricated using the block copolymer template on SiO₂ substrate acted as the working electrode. The reference electrode consists of Ag/AgCl and KCl and a platinum gauze was used as the counter electrode. A mixture of potassium ferric cyanide and KCl was used as the electrolyte. These experimental set-ups were connected to a potentiostat VERSAT tool for the electrochemical measurements.

7.4. Results and Discussions

Briefly, the substrate was coated with a random copolymer (HO-PS-*r*-PMMA) brush to generate a neutral surface as discussed in *Chapter 2* [3, 21]. A symmetric polymer PS-*b*-PMMA thin film on the brush exhibited lamellar morphology upon microphase separation with a lamellar domain spacing of 26 nm. A soft PS mask template was generated by selective removal of the PMMA block [22]. Top-down and cross-section SEM images of the resultant PS mask are shown in **Figure 7.4.1(a)**. The PS stripes have a full-width-half-maximum of 12 nm and a height of around 23 nm. Cu nanowires were generated by thermal evaporation onto this structure. **Figure 7.4.1(b)** shows the top-down SEM image of the nanowires and

a corresponding TEM cross-section of bright and dark field images are shown in **Figure 7.4.1(c, d)**. This reveals a structure that consists of two layers of copper nanowires in a 3-D geometry. The lower layer at the SiO₂ substrate surface and an upper layer supported by the PS lines. At the substrate surface, the mean diameter of the nanowires is ~13 nm with a pitch of 26 nm consistent with BCP template. The upper level nanowires have a mean diameter of ~15 nm.

The presence of copper is confirmed by XRD (**Figure 7.4.2(a)**) and EDAX (**Figure 7.4.2(b)**) analysis. The copper nanowires formed by this procedure are polycrystalline and X-ray diffraction (XRD) shows features at $2\theta \sim 43.6, 50.82,$ and 74.58° assignable to (111), (200) and (220) reflections from the face centred cubic structure of Cu (JCPDS file 04-0836). A peak at $46.76^\circ 2\theta$ is a reflection from the silicon substrate. The Cu(200) plane has a much greater peak intensity than expected and indicates preferred growth in this direction. The nanowire crystallinity is also revealed by obvious diffraction fringes in bright field TEM cross-section images (**Figure 7.4.1(d)**). EDAX analysis from SEM shows strong copper signals and also visible is O, Si (SiO₂) and carbon features (PS). Electrochemical alternating current (AC) impedance spectroscopy (EIS) is widely used in supercapacitor characterisation and represents a global view of the electrical properties of the substrate surface [6]. Data are shown in **Figure 7.4.3(a)** of the 3-D nanowire system fabricated here (DC bias potential of 5 V, amplitude 280 mV for a frequency range of 0.1 Hz to 1000 Hz). The semicircle is representative of the electrical double layer of the capacitor and the vertical line represents the supercapacitive properties. Linear voltammetry *I-V* scans were performed using the 3-D copper nanowire structure as the working electrode (**Figure 7.4.3(b)**). These data represent the presence of the 3-D copper nanostructure since data from a bare SiO₂ substrate (**Figure 7.4.3(c)**) indicates only low signal, high noise levels expected from an insulator. The data in **Figure 7.4.3(b)** were repeated many times and showed extremely reproducible behaviour indicating the system stability. The data always showed a periodic profile

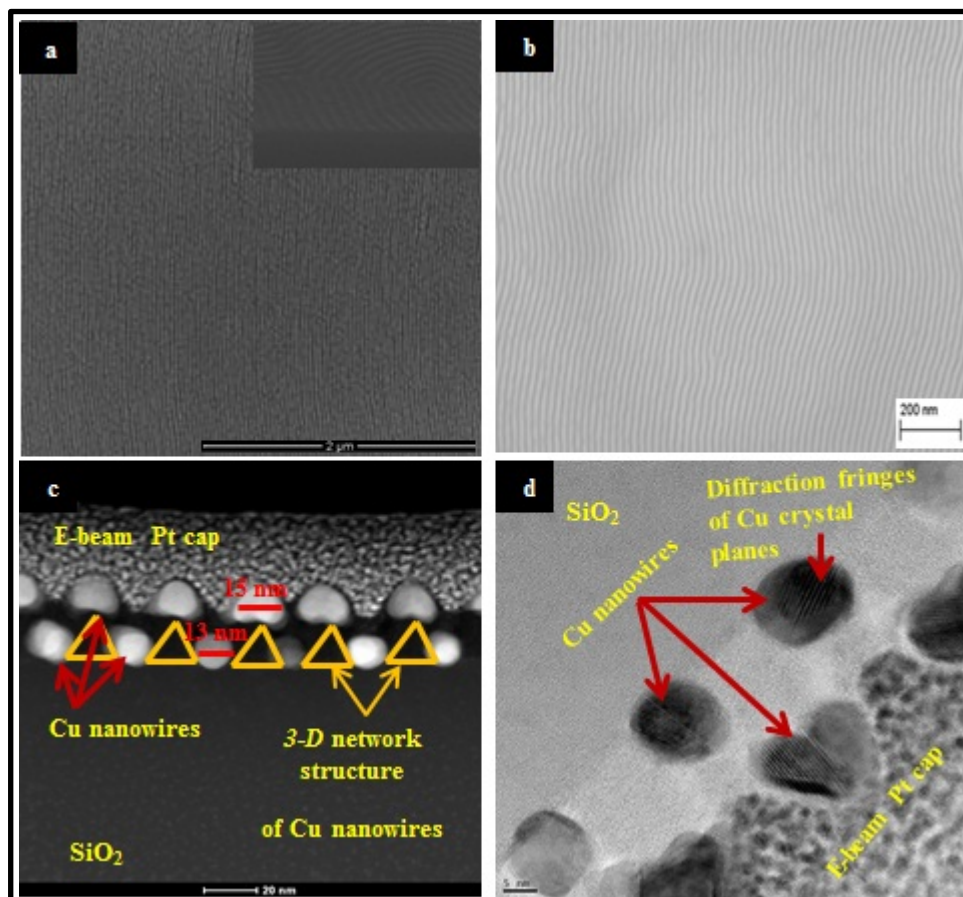


Figure 7.4.1. (a) Top-down SEM image of the PS template obtained from microphase separated PS-*b*-PMMA (18k-18k) film after selective dry etching of PMMA block (inset is the cross-section SEM image of the PS template), (b) Top-down SEM image of Cu nanowires obtained by depositing copper on PS mask template. (c) Dark-field TEM cross-section images of Cu nanowires with 3-D geometry. (d) Bright-field TEM cross-section image of Cu nanowires with 3-D geometry.

reflecting charging and discharging phenomena taking place in the electrochemical cell with respect to the working electrode. We believe that this phenomenon can be explained by properly considering the complex geometry of the system. The top and bottom layer of nanoelectrodes are structurally different with different electrode (nanowire) sizes, separations (**Figure 7.4.1(c)**) and electrolyte exposure (much greater at the upper layer) and this leads to a potential difference being developed between the top and bottom layers.

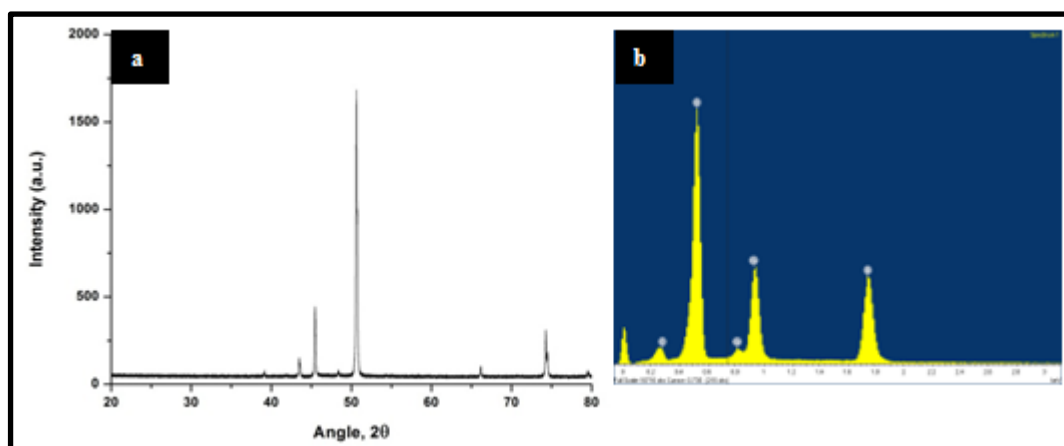


Figure 7.4.2. (a) X-ray diffraction (XRD) spectrum Cu nanowires and (b) EDS spectrum of Cu nanowires.

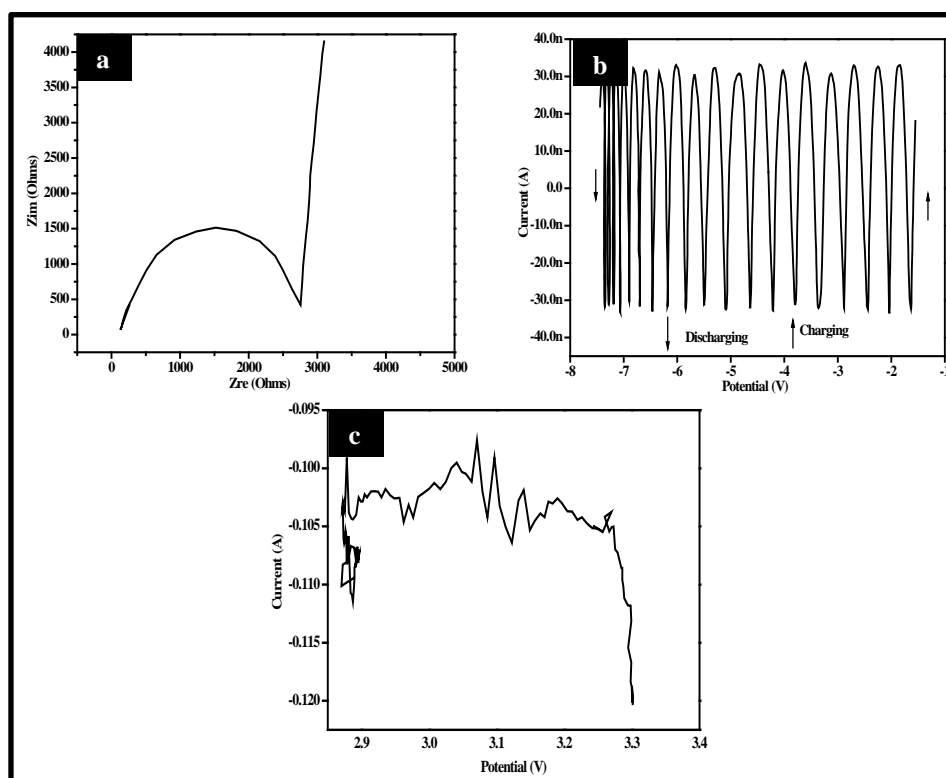
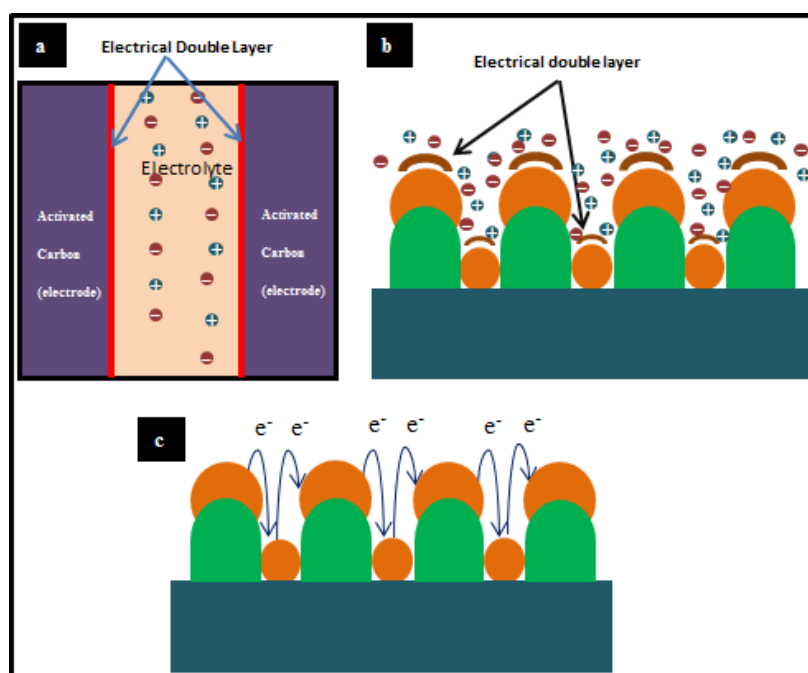


Figure 7.4.3. (a) Electrochemical AC impedance spectroscopy (EIS) scan of Cu nanowires on SiO₂ substrate in an electrolyte mixture of 0.1 mol L⁻¹ KCl and 0.5 mmol L⁻¹ Fe(CN)₆^{4-/3-}. (b) and (c) Linear *I-V* characteristics of Cu nanowires on SiO₂ substrate and bare SiO₂ substrate in the electrolyte mixture.

whereas in our system, as shown in **Scheme 7.2(b)**, each individual copper nanoelectrodes provides an electrical double layer formation leading to complex

behaviour and electrical transport between the upper and lower electrode layers. Because of the structural arrangement of the working electrode, once the potential difference is developed, electron transport between electrodes appears to be a quite as described in **Scheme 7.2(b)**. This phenomenon compels the supercapacitor system



Scheme 7.2 (a) Schematic of conventional EDL supercapacitor. (b) Schematic of electrical double layer formation on 3-D structured copper nanoelectrode supercapacitor. (c) Schematic of electron transport phenomenon in top and bottom layer copper nanoelectrodes.

complex phenomenon. We believe that during a voltage sweep that negative ions are primarily discharged at the top electrode layer developing a negative potential difference between the upper and lower nanowire layers. Effectively, the confinement of the bottom nanoelectrodes layer limits electrical discharge until the potential difference is such to provide electrical breakdown between the two layers to behave in the sinusoidal manner by **Figure 7.4.3(b)** due to the electron transport as shown in **Scheme 7.2(c)**. Almost ideal supercapacitance behaviour is demonstrated in **Figure 7.4.4(a&b)** by following charge-time curves at various currents

(25 mA to 75 mA in the charging scan and -25 mA to -75 mA in the discharging scan). Similar data have been reported from other systems [23].

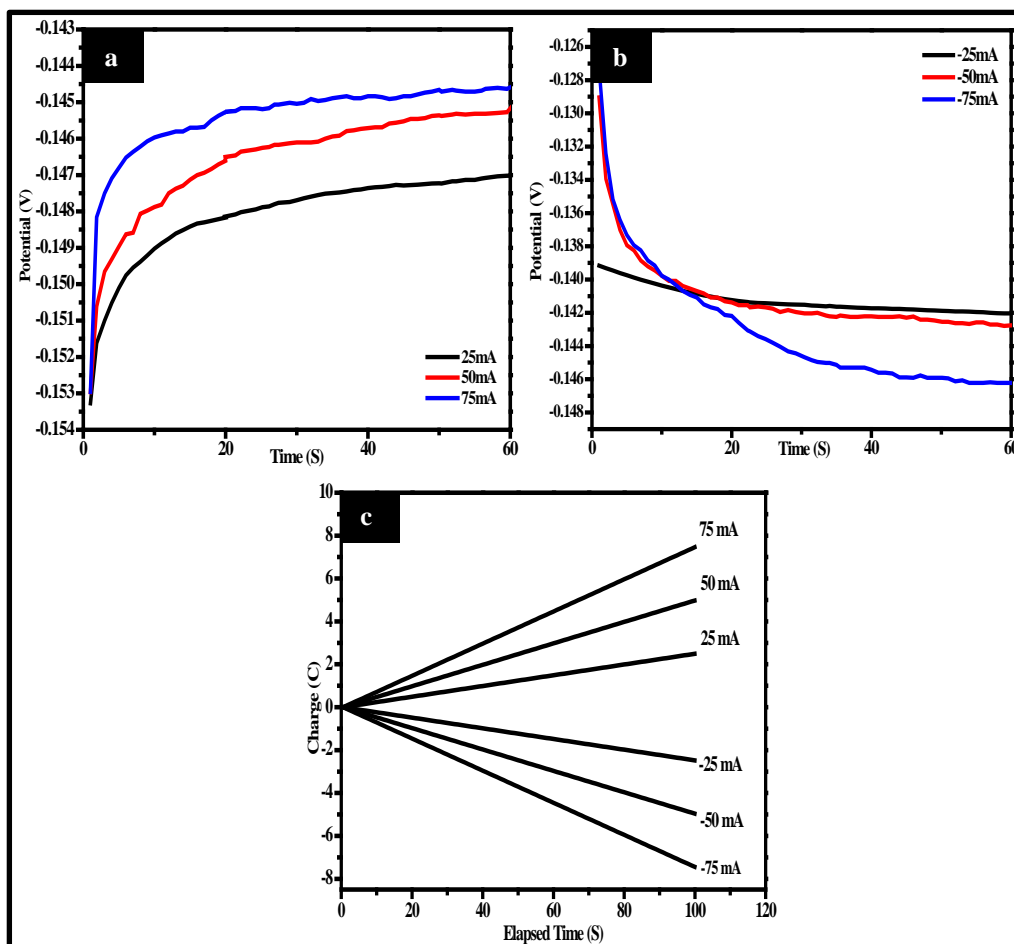


Figure 7.4.4. (a) Charging profile at current 25 mA, 50 mA and 75 mA. (b) discharging profile at current -25 mA, -50 mA and -75 mA of Cu nanoelectrodes in an electrolyte mixture of 0.1 mol L⁻¹ KCl and 0.5 mmol L⁻¹ Fe(CN)₆^{4-/3-} for 100 s. (c) Time analysis of charging and discharging phenomena in Cu nanoelectrodes in the electrolyte mixture.

From **Figure 7.4.4(c)**, it can be seen that the charging and discharging phenomena is taking place at a similar rate and that the relationship between charging and discharging profile is constant regardless of the potential. The performance of a supercapacitor can be evaluated by the specific capacitance (C_s) using the established chronopotentiometry where, $C_s = I / (\partial E / \partial t) m = I / (\text{slope}) m$; where, I = constant applied current, $\partial E / \partial t$ = slope of the charge curve after IR drop and m = mass of the active electrode material [7, 23, 24]. These structures provide excellent capacitive

performance with a maximum specific capacitance of ~836 F/g for a current density of 8.06 A/g at a discharge current as high as 75 mA. The excellent performance is due to a high surface area: volume ratio. We suggest that this highly novel, easily fabricated structure may be used in a number of on-chip charge storage applications.

7.5. Conclusions

In summary, we have fabricated a copper nanowire structure using block copolymer templates in a simple quick and reproducible way. The methodology is consistent with simple fabrication procedures that can be introduced into conventional semiconductor manufacturing and offer considerable advantage over more expensive lithographic methods and does not necessitate the use of materials or processes that might afford major integration challenges. The 3-D structure showed some unexpected characteristics but detailed electrochemical measurements showed very high capacitance compared to conventional systems [1, 12, 25]. We believe this approach may be used in a number of on-chip charge storage applications.

7.6. References

- [1] X. Xia, T. Jiangping, Y. Mai, R. Chen, X. Wang, C. Gu, X. Zhao, *Chem. Eur. J.* **2011**, *17*, 10898.
- [2] V. D. Patake, S. S. Joshi, C. D. Lokheande, O. -S. Joo, *Mater. Chem. Phys.* **2009**, *114*, 6.
- [3] D. Borah, M. T. Shaw, S. Rasappa, R. A. Farrell, C. T. O'Mahony, C. M. Faulkner, M. Bosea, P. Gleeson, J. D. Holmes, M. A. Morris, *J. Phys. D: Appl. Phys.* **2011**, *44*, 202.
- [4] B. E. Conway, *Electrochemical Supercapacitors: Scientific Fundamentals and Technological Applications* (Kluwer) **1999**.
- [5] J. -K. Chang, C. -M. Wu, I. -W. Sun, *J. Mater. Chem.* **2010**, *20*, 3729.
- [6] B. Kim, H. Chung, W. Kim, *Nanotechnology* **2012**, *23*, 155401.
- [7] X. Lang, A. Hirata, T. Fujita, M. Chen, *Nat. Nanotechnol.* **2011**, *6*, 232.
- [8] S. Chen, J. Zhu, X. Wu, Q. Han, X. Wang, *ACS Nano* **2010**, *4*, 2822.

- [9] X. Li, J. Rong, & B. Wei, *ACS Nano* **2010**, 4, 6039.
- [10] L. Nyholm, G. Nyström, A. Mihranyan, M. Strømme, *Adv. Mater.* **2011**, 23, 3751.
- [11] M. -H. Jung, H. Lee, *Langmuir* **2008**, 24, 9825.
- [12] W. -D. Zhang, J. Chen, *Pure Appl. Chem.* **2009**, 81, 2317.
- [13] J. P. Zheng, P. J. Cygan, & T. R. Jow, *J. Electrochem. Soc.* **1995**, 142, 2699.
- [14] V. Polshettiwar, B. Baruwati, R. S. Varma, *ACS Nano* **2009**, 3, 728.
- [15] Y. X. Zhang, H. C. Zeng, *Langmuir* **2008**, 24, 3740.
- [16] C. L. Cheung, R. J. Nikolić, C. E. Reinhardt, T. F. Wang, *Nanotechnology* **2006**, 17, 1339.
- [17] Y. Piao, H. Kim, *J. Nanosci. Nanotechnol.* **2009**, 9, 2215.
- [18] I. W. Hamley, *Nanotechnology* **2003**, 14, R39.
- [19] M. P. Stoykovich, P.F. Nealey, *Mater. Today* **2006**, 9, 20.
- [20] J. Y. Cheng, C. A. Ross, E. L. Thomas, H. I. Smith, G. J. Vancso, *Appl. Phys. Lett.* **2002**, 81, 3657.
- [21] P. Mansky, Y. Liu, E. Huang, T. P. Russell, C. Hawker, *Science* **1997**, 275, 1458.
- [22] R. A. Farrell, N. Petkov, M. T. Shaw, V. Djara, J. D. Holmes, M. A. Morris, *Macromolecules* **2010**, 43, 8651.
- [23] M. Naumowicz, Z. A. Figaszewski, *J. Membrane Biol.* **2011**, 240, 47.
- [24] M. J. Jung, E. Jeong, S. Cho, S. Y. Yeo, Y. S. Lee, *J. Colloid. Interf. Sci.* **2012**, 381, 152.
- [25] Y. Song, J. Wang, Z. Li, D. Guan, T. Mann, Q. Liu, M. Zhang, and L. Liu, *Micropor. Mesapor. Mater.* **2012**, 148, 159.

8.1. Abstract

Germanium nanowires (GeNWs) have importance in emerging device applications because of their high hole mobility. Reported in this *chapter 8* is the fabrication of GeNWs on a SiO₂ insulator substrate from a phase separated lamellar PS-*b*-PMMA block copolymer (BCP) by a simple and reproducible method. The parent BCP film was selectively etched to remove PMMA block generating PS template, as mentioned in *chapter 4*, which was then used for seedless fabrication of GeNWs by a thermal evaporation technique. XRD, Raman and TEM cross-section analysis reveal the formation of GeNWs on SiO₂ substrates. Thermal treatment of the GeNWs was used to probe thermal stability and crystallisation properties. It was observed that thermal treatment of GeNWs resulted in red-shifts in the Raman spectra. The results demonstrate an exciting nanofabrication technique for creating high density nanowires for the nanoelectronic industry.

8.2. Introduction

The very impressive device scaling implemented by the semiconductor industry has led to the development of current computer and communication devices [1]. However, there is considerable research impetus towards the development of novel semiconductor materials and CMOS device structures as it has become a significant challenge to maintain progress by miniaturization alone [2-6]. One area of interest is the use of semiconductors with superior electronic properties to complement and replace the conventional silicon based technology. Germanium (Ge) is a leading candidate with a lower band gap energy, lower effective electron masses and higher carrier mobilities [7]. Further, Ge is compatible with current CMOS design but might afford development of devices with lower drive voltages and higher drive currents for high-speed electronic applications [7]. However, the use of Ge is a challenge because of cost, reactivity and manufacturing integration challenges and conventional fabrication technologies will not be applicable.

It seems likely that in the future nanoelectronic devices might be based around the use of nanowire type structures [8]. Various methods have been employed to synthesize germanium nanowires (GeNWs). The first GeNW synthesis using a

solvothermal approach was reported by Heath and LeGoues [9]. Synthesis of GeNWs can also be achieved by molecular beam epitaxy (MBE) [10], laser ablation [11], physical vapor transport [12], solution within a supercritical fluid medium [13, 14], and low-temperature chemical vapor deposition (CVD) [15] methods. Many of these synthesis methods proceed through a vapor-liquid-solid (VLS) crystal growth mechanism in the presence of Au nanocatalysts [16] whose characteristics determines the features of the grown nanowires *viz.*, diameter and their distribution, growth direction, location, and orientation. The major disadvantage of these methods is that there is little control over the orientation, arrangement or placement of the nanowires and this limits their applicability in the fabrication of real devices.

Reported here is the fabrication of GeNWs on silicon substrate with a thick insulator (SiO_2) layer using a bottom-up approach based on block copolymer (BCP) self-assembly technique. Ge was deposited by a thermal evaporation technique onto a polystyrene (PS) template fabricated from a microphase separated polystyrene-*b*-polymethylmethacrylate (PS-*b*-PMMA) BCP nanopatterned film. The topographical template was created by selective etch of the PMMA component. This methodology has advantages in generating wires of uniform size, and spacing and, further, does not require the aid of catalysts and involves manufacturing methods well established in industry.

8.3. Materials and methods

8.3.1. Materials

A hydroxyl-terminated random copolymer composed of styrene (S) and methyl methacrylate (MMA), denoted as HO-PS-*r*-PMMA, and a symmetric lamella-forming PS-*b*-PMMA BCP were purchased from Polymer Source, Inc., Canada, and used as received. The detail characteristics of the polymers are compiled in **Table 8.1**. The substrates used were silicon wafers <100> with a passive oxide (SiO_2) layer of thickness 120 nm. Sulphuric acid, hydrogen peroxide, toluene, DMF, acetone and isopropyl alcohol were purchased from Sigma-Aldrich and used without further purification unless otherwise stated. De-ionised (DI) water was used wherever necessary.

Table 8.1. Characteristics of polymer used for present study.

M_n / g mol^{-1}	Designation	Polydispersity index, M_w/M_n	PS mole fraction, %
12,400	HO-PS- <i>r</i> -PMMA	1.25	0.58
36,000	PS- <i>b</i> -PMMA	1.07	0.46

8.3.2. BCP film preparation

Substrates were cleaned in a piranha solution (1:3 v/v 30% H_2O_2 : H_2SO_4) at 363 K for 60 min, rinsed with DI water, and dried under N_2 flow. A hydroxyl-terminated random copolymer brush solution of 1.0 wt. % in toluene was spin-coated (P6700 Series Spin-coater) onto substrates at 3000 rpm for 30 s. The brush coated samples were annealed in a vacuum oven (Townson & Mercer EV018) at 443 K under vacuum (13.25 mbar of residual pressure), well above the glass transition temperatures (T_g) of both PS (373 K) and PMMA (388 K) for 6 h. This allows the end-functional hydroxyl groups of the random copolymers to react with silanol groups on the silica surface resulting in the polymer chain brushes anchored on the substrate via condensation reactions. Unbound polymers were removed by sonication (Cole-Palmer 8891 Sonicator) and rinsing in toluene.

PS-*b*-PMMA thin films were prepared by spin-coating the polymer solution of 1.0 wt. % in toluene onto the brush anchored surfaces at 3200 rpm for 30 s (film thickness ca. 38 nm). Samples were annealed at 453 K under vacuum (13.25 mbar of residual pressure) for 4 h, to induce phase separation and remove any remaining solvent. Thin films were removed from the oven immediately after annealing, without any specific cooling temperature profile.

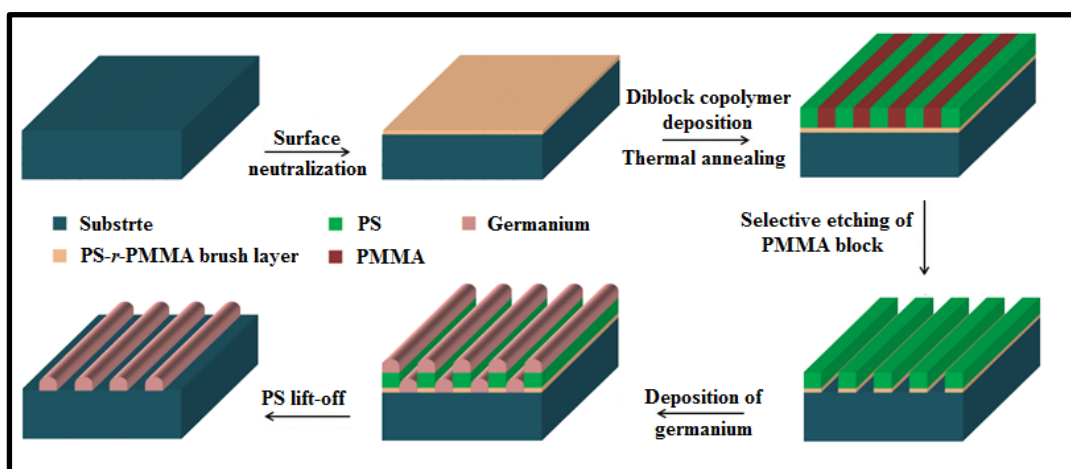
8.3.3. PS template preparation

Selective removal of PMMA block from the annealed PS-*b*-PMMA thin films on a neutral polymer bush was accomplished by inductively coupled plasma (ICP) etching in a OIPT Plasmalab System 100 ICP180 with an Ar/ O_2 etch recipe of

Ar (5 sccm) and O₂ (15 sccm) at 1.3 Pa and 100 W for 6 s to generate PS template mask structures. Full details are given elsewhere [17, 18].

8.3.4. Ge deposition and PS template lift-off

Deposition of Ge was achieved by a thermal evaporation technique using a Temescal FC-2000 evaporation system. Ge was evaporated onto the PS templates generated as detailed above. The substrate was held at 333 K during evaporation. The deposition rate was around 1 Å s⁻¹ which delivered a film thickness of 13 nm.



Scheme 8.1. Schematic diagram of the fabrication of GeNWs using a PS template obtained from microphase separated PS-*b*-PMMA (18k-18k) film on SiO₂ substrate whose surface was chemically modified with a random HO-PS-*r*-PMMA polymer brush.

A wet, chemical, solvent lift-off process was developed to remove the PS template. Lift-off was carried out by sonication in various solvents such as toluene, acetone, etc., for 5 min followed by extensive rinsing in fresh solvents. It was found that a solvent mixture of acetone and isopropyl alcohol in the ratio of 1: 1 gave the best results in terms of producing non-damaged materials and effective removal of polymer residues. Finally, the samples were dried at 333 K for 60 min under vacuum. A schematic diagram showing the fabrication of GeNWs using BCP template is presented in **Scheme 8.1**.

8.3.5. Annealing of GeNWs

The GeNWs fabricated on SiO₂ substrate were annealed in a tube furnace (Lenton Thermal Design) under an inert environment (Ar). Samples were heated at a

ramp rate of 283 K min^{-1} and kept at the desired temperature (573 or 873 K) for 30 min before cooling down to room temperature at a rate of 283 K min^{-1} . Annealed samples were stored in air tight containers to minimize atmospheric oxidation prior to analysis.

8.3.6. Material characterization

BCP film thickness was determined by ellipsometry (Plasmos SD2000 Ellipsometer). An average of three readings collected from different locations on a sample surface was reported as the film thickness result. Microscopic studies of the polymer films were made by an atomic force microscope (DME 2452 DualScope Scanner DS, AFM) operated in tapping mode under ambient conditions using silicon microcantilever probe tips with a force constant of $60,000 \text{ N m}^{-1}$ and a scanning force of 0.11 nN. Topographic and phase images were recorded simultaneously. Powder X-ray diffraction (XRD) measurement was performed with a Philips X'Pert diffractometer using Cu K_α radiation with an anode current of 40 mA and an accelerating current of 40 kV. Raman data were recorded in a confocal backscattering configuration at ambient conditions using a Renishaw InVia Raman microscope with spectral resolution of 1 cm^{-1} and collected by a CCD detector. The sample was excited by the red line of an Ar^+ laser ($\lambda = 488 \text{ nm}$) and it the source was focused with an X100 objective lens to give a $0.85 \text{ }\mu\text{m}$ focus spot in diameter. The laser power was lowered to 5 mW on the sample to prevent excessive local heating with, the substrate acting as a heat sink to reduce the local heating.

Top-down and cross-sectional scanning electron microscope (SEM) images were obtained by a high resolution ($< 1 \text{ nm}$) field emission Zeiss Ultra Plus SEM equipped with a Gemini[®] column operating at an accelerating voltage of 5 kV. An FEI Strata 235-Focused Ion Beam (FIB) tool with resolution up to 10 nm was used to analyse cross-section samples. For sectioning these, electron-beam platinum was deposited above the nanowire patterns followed by the ion-beam platinum. Milling and polishing of the protective coatings was done at the lower aperture size and then the specimen was imaged under the higher resolution Zeiss Ultra Plus SEM. Transmission electron microscope (TEM) lamella specimens were prepared by the

Zeiss Auriga-Focused Ion Beam (FIB) with a Cobra ion column having a 2.5 nm resolution and were image analysed using a FEI Titan-TEM operating at an accelerating voltage of 130 kV.

8.4. Results and discussion

8.4.1. BCP self-assembly and PS template fabrication on SiO₂ substrate

Upon thermally induced microphase separation the symmetric PS-*b*-PMMA thin films, prepared on a neutral polymer brush layer, exhibit a morphology consisting of alternating lamellae of PS and PMMA. The brush layer is necessary to ensure that the lamellae are oriented perpendicular to the substrate [19]. **Figure 8.1(a)** shows the topography image of the PS-*b*-PMMA film on SiO₂ substrate. The random copolymers are used to manipulate interfacial energies at the substrate-BCP interface. The surface is deemed neutral because both blocks interact equally with the brush, therefore, directing the strip-like pattern into a vertical (to the surface plane) [19].

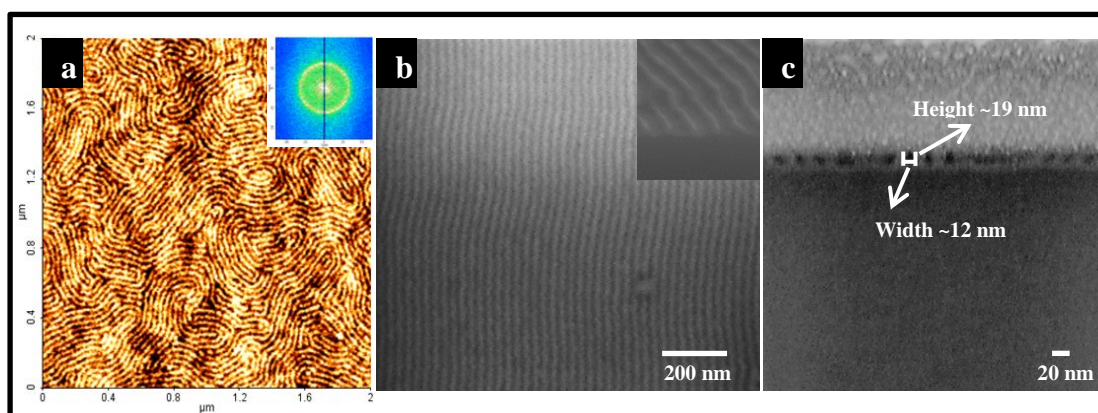


Figure 8.1. (a) AFM topography 2-D image of microphase separated PS-*b*-PMMA (18k-18k) film on SiO₂ substrate anchored with a random HO-PS-*r*-PMMA polymer brush. Inset (a) is the FFT of the topography image. (b) Top-down SEM image of the PS template created by a selective etch of the PMMA block. Inset (b) is the cross-section SEM image. (c) FIB cross-section image of PS template.

Both blocks also exist at the air-BCP interface since the surface tension difference between PS and PMMA is small [20]. The Fourier transform of the topography image, inset in **Figure 8.1(a)** displays a ring structure indicating the

random arrangement of the lamellae with a lamellae repeat distance (λ_L) of 26 nm (as determined from the Fourier transform).

In order to generate substrate features from the BCP nanopatterns, the simplest method is to develop structural templates (e.g. by introducing polymer topography) into which active materials can be deposited [20]. This can be achieved by selectively removing one of the components. A selective plasma etch was developed based around conditions which showed different etch rates for the two blocks. Careful optimisation of the etch conditions and gases using homopolymer films allowed selective removal of PMMA as reported elsewhere [17, 18]. The etch process used here was shown to have a PMMA etch rate 7 times faster than that of PS [17, 18]. It should be noted that PMMA removal during the etch also results in complete removal of any brush components. Typical top-down SEM image of film is shown in **Figure 8.1(b)** and this confirms the removal of PMMA domains generating PS template masks since topographical contrast is developed. The SEM cross-section image of the PS template generated upon plasma etching is shown in inset **Figure 8.1(b)**, illustrating the empty channels between the PS line structures. Etching of PMMA was further verified by FIB cross-section image as shown in **Figure 8.1(c)** which shows PS stipe width of ~12 nm and height of ~19 nm. The top of the PS domains have become curved indicating that the etch process is at least partially isotropic resulting in shrinking of the features during etching. This is a phenomenon known as faceting. This also confirms homopolymer studies that PS component is etched during the etch process but at a slower rate than the PMMA. It was observed while SEM imaging that the pattern is significantly aligned with more than 90 % coverage on SiO₂ substrate. It can be noted that the AFM image in **Figure 8.1(a)** shows fingerprint type of patterns on SiO₂ substrate, which is inconsistent with the SEM image in **Figure 8.1(b)**.

8.4.2. Fabrication and characterisation of GeNW arrays

The PS soft mask template fabricated from the BCP pattern on SiO₂ substrate can be used to develop GeNW arrays by simple thermal evaporation of Ge and subsequent lift-off. A top-down SEM image is presented in **Figure 8.2(a)** and the improved contrast does suggest some localised germanium deposition has been

achieved. However, it is difficult to ascertain the complete removal of PS stripes from the top-down SEM image and, therefore, TEM analysis was carried out. **Figure 8.2(b)** shows the TEM cross-section image of the GeNWs after the lift-off process. The presence of a well-defined single layer of GeNWs confirms the effectiveness of the PS lift-off process. The SEM image shows that the GeNWs are uniform in diameter and were unaffected by the solvent used in the lift-off process. The average diameter of the GeNWs is ~ 12 nm with almost a similar spacing between them ~ 13 nm and this is consistent with the original BCP pattern dimensions provided above. The presence of GeNWs in these samples was confirmed by XRD analysis and the diffractogram is presented in **Figure 8.3**. There is little evidence of high or sloping backgrounds in XRD data or any very large peaks which would be indicative of the presence of amorphous Ge [21].

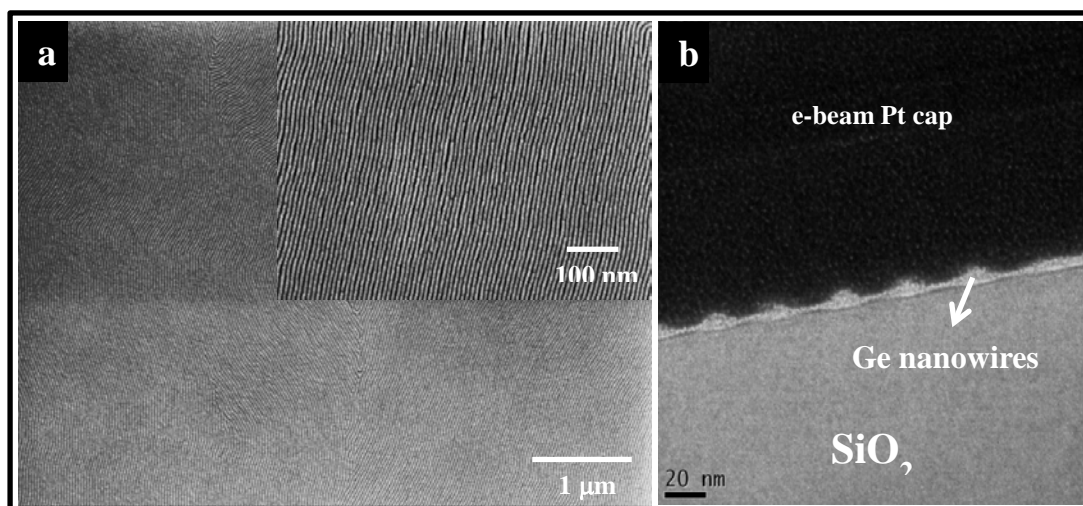


Figure 8.2. (a) Top-down SEM image of GeNWs obtained after PS lift-off. Inset (a) is the high resolution SEM image. (b) Bright-field TEM cross-section image of GeNWs obtained after PS lift-off.

The only obvious Ge related feature is observed at a 2θ angle of $\sim 54.5^\circ$ and this reflection can be indexed as (311) plane of the cubic structure of Ge (JCPDS card no. 040545) [22]. The crystallite lattice parameter can be calculated from the (311) peak position and is 5.54 \AA which is consistent with literature values [23]. The absence of other features from germanium suggests there is strong preferential growth of germanium in the (311) direction. The absence of features derived from germanium dioxide (GeO_2) peaks in the diffraction data clearly indicates that the

nanowires did not suffer extensive oxidation in the solvent lift-off stage. It should be noted that during air exposure, GeO_2 reacts with ambient conditions to produce well-defined germanium hydroxide features which can be easily observed. The observation of amorphous wires by TEM cross-sectioning is in contrary to other evidence of a crystalline structure. The difference probably results in the amorphitization or oxidation (to GeO_2) at the surface sponsored during FIB cross-section [24]. As can be seen, the Ge(311) feature is relatively narrow suggesting the

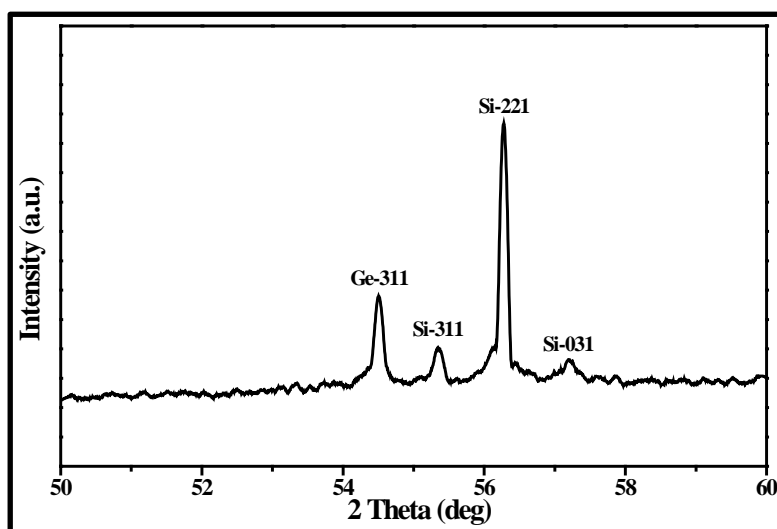


Figure 8.3. XRD diffractogram of GeNWs developed on SiO_2 substrate. Silicon features from the substrate can also be seen and are indexed as shown according to JCPDS card nos. 040545 and 271402.

crystallite grain size (L_C) is relatively large. The well-known Scherrer equation [25] can be used to calculate L_C of the GeNWs from the width of the (311) reflection in the XRD profile (**Equation 8.1**).

$$LC = \frac{K\lambda}{\beta \cos \theta} \quad (8.1)$$

where K is a constant of order one (0.89), λ is the X-ray wavelength (0.154 nm), β (in radians) is the half-height width of a reflection and θ is the Bragg angle. Using a β value of 0.165 degrees, the grain size can be estimated at about 54 nm. Since the angle of a (311) plane is 72.4° to the (010) and (001) planes, an estimate of the grain size in the (001) or (010) direction is around 16.2 nm. This is similar to the measured

nanowire width as measured above and suggests that the wires are largely crystalline in nature with a width limited by crystallite growth across the width of the nanowire.

8.4.3. Effect of thermal treatment on GeNWs

In order to crystallise the nanowires further, it is likely some thermal treatment would be required. Thus, the GeNWs were annealed at higher

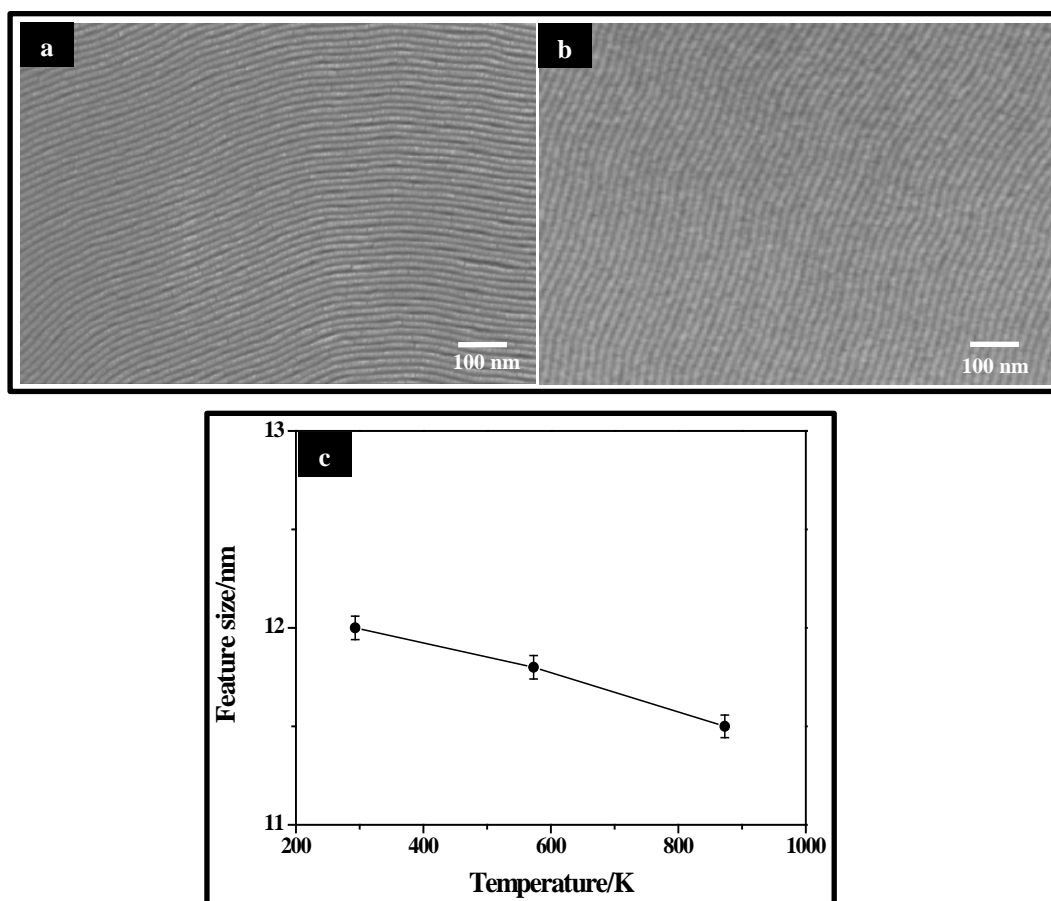


Figure 8.4. Top-down SEM images of GeNWs annealed at (a) 573 K and (b) 873 K for 30 min in inert environment (Ar). (c) Plot of GeNW feature size vs. anneal temperature.

temperatures in an inert atmosphere to understand any structural property and morphology changes that may occur under thermal load. Data are presented in **Figure 8.4(a, b)**. The top-down SEM images of the annealed GeNWs reveal that the nanowires retain the *1-D* nanostructure and the thermal treatment brings about little mechanical damage to the nanostructures. However, minor decrease in the feature size of the GeNWs is observed from the data (derived from the SEM images) shown

in **Figure 8.4(c)**. It should be noted that the average feature size of the nanowires is reported in the figure. This could be accounted to either smoothing of the GeNWs or shrinking in feature size or both during thermal treatment.

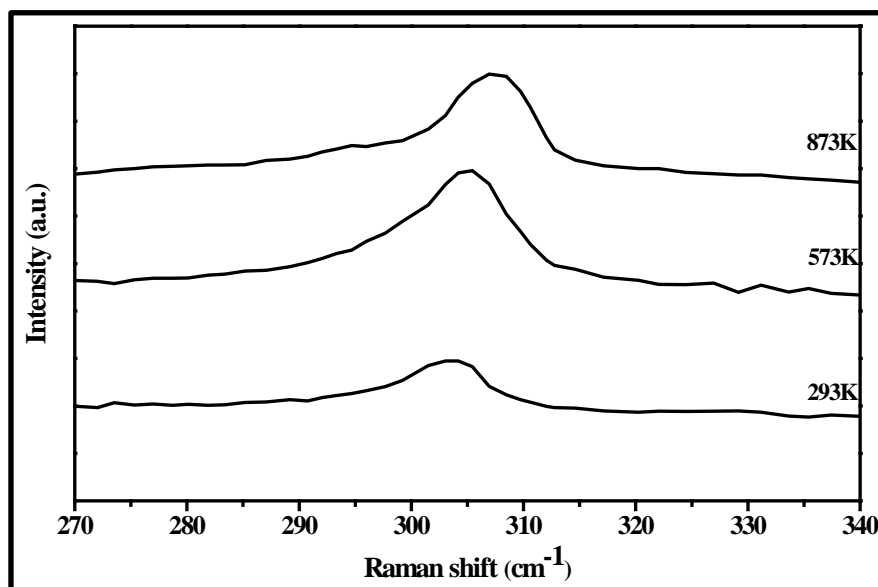


Figure 8.5. Raman spectra of GeNWs annealed at different temperatures.

The crystalline quality, phonon confinement effect and lattice strain of the GeNWs before and after anneal was further studied by Raman analysis and data are shown in **Figure 8.5**. The spectrum of unannealed GeNWs shows a Raman peak at 303 cm^{-1} with a full-width-at-half-maximum (FWHM) of 5.7 cm^{-1} . The Raman measurement was performed at various locations of the sample to understand the homogeneity of nanowire diameter and yielded similar Raman spectra suggesting uniform GeNW diameter. This mode is attributed as the well-known Raman active first-order transverse optical phonon mode of crystalline Ge (Ge-Ge stretching mode) [26]. This is consistent with the XRD analysis and confirms the crystalline nature of the as-deposited nanowires. The peak is red-shifted by 3 cm^{-1} compared to that of bulk Ge at 299 cm^{-1} indicating the phonon confinement effect expected at the small wire dimensions. The effect arises because of the small diameter of the nanowires which is smaller than the excitonic Bohr radius of Ge (24.3 nm) [27]. This effect has been widely reported for Ge nanocrystals and a noticeable phonon confinement effect was observed on nanocrystals as large as 7 nm [28].

However, similar studies on one-dimensional aligned GeNWs fabricated based around BCP lithography are lacking [29] and to further understand this effect the GeNWs were annealed at higher temperature. The results are presented in **Figure 8.5** and suggest even stronger quantum confinement of optical phonon in GeNWs. It can be seen that the Raman peak is further red-shifted (peak positions were 305 and 308 cm^{-1} at 573 K and 873 K, respectively) and also show increased peak intensities. Quantum confinement in the thermally treated GeNWs samples is due to decrease in feature size of GeNWs as is evident from **Figure 8.4(c)**.

8.5. Conclusions

We report here the method of fabricating GeNW arrays by BCP lithography approach. The GeNWs were fabricated by thermal evaporation of Ge onto the BCP template developed from PS-*b*-PMMA (18k-18k). The GeNWs are uniform in diameter (12 nm) and shows crystallinity. Raman spectra of the nanowire arrays reveal the phonon confinement effect in GeNWs. The method demonstrated for the fabrication of GeNWs is highly reproducible, time and cost effective and have great potential for integrating into the device fabrication process.

8.6. References

- [1]. <http://public.itrs.net/>, **2011**.
- [2] C. A. Mack, *IEEE T Semiconduct M.* **2011**, 24, 202.
- [3] H. J. Dai, *Acc. Chem. Res.* **2002**, 35, 1035.
- [4]. C. M. Lieber, *MRS Bull.* **2003**, 28, 486.
- [5]. Y. N. Xia, P. D. Yang, *Adv. Mater.* **2003**, 15, 351.
- [6]. P. D. Yang, *MRS Bull.* **2005**, 30, 85.
- [7]. S. M. Sze, *Physics of Semiconductor Devices*, John Wiley, New York, **1981**.

- [8]. M. Henini, Ed. *Handbook of Self Assembled Semiconductor Nanostructures for Novel Devices in Photonics and Electronics*, Elsevier Ltd., ISBN: 978-0-08-046325-4, **2008**.
- [9]. J. R. Heath and F. K. LeGoues, *Chem. Phys. Lett.* **1993**, 208, 263.
- [10]. Y. Wu, R. Fan and P. Yang, *Nano. Lett.* **2002**, 2, 83.
- [11]. A. M. Morales and C. M. Lieber, *Science* **1998**, 279, 208.
- [12]. G. Gu, M. Burghard, G. T. Kim, G. S. Dusberg, P. W. Chiu, V. Krstic, W. Q. Han, *J. Appl. Phys.* **2001**, 90, 5747.
- [13]. R. G. Hobbs, S. Barth, N. Petkov, M. Zirngast, C. Marschner, M. A. Morris and J. D. Holmes, *J. Am. Chem. Soc.* **2010**, 132, 13742.
- [14]. C. Collins, M. Kolesnik, V. Krstic and J. D. Holmes, *Chem. Mater.* **2010**, 22, 5235.
- [15]. Y. Cui and C. M. Lieber, *Science* **2001**, 291, 851.
- [16]. R. S. Wagner and W. C. Ellis, *Appl. Phys. Lett.* **1964**, 4, 89.
- [17]. D. Borah, M. T. Shaw, S. Rasappa, R. A. Farrell, C. O'Mahony, C. M. Faulkner, M. Bosea, P. Gleeson, J. D. Holmes, M. A. Morris, *J. Phys. D: Appl. Phys.* **2011**, 44, 174012.
- [18]. R. A. Farrell, N. T. Kinahan, S. Hansel, K. O. Stuen, N. Petkov, M. T. Shaw, L. E. West, V. Djara, R. J. Dunne, O. G. Varona, P. G. Gleeson, S. -J. Jung, H. -Y. Kim, M. M. Kolesnik, T. Lutz, C. P. Murray, J. D. Holmes, P. F. Nealey, G. S. Duesberg, V. K. Krstić, M. A. Morris, *Nanoscale* **2012**, 4, 3228.
- [19]. P. Mansky, Y. Liu, E. Huang, T. P. Russell and C. Hawker, *Science* **1997**, 275, 1458.
- [20]. S. B. Darling, *Surf. Sci.* **2007**, 601, 2555.
- [21]. D. Riabinina, F. Rosei and M. Chaker, *J. Exp. Nanosci.* **2005**, 1, 83.
- [22]. W. Wang, B. Poudel, J. Y. Huang, D. Z. Wang, S. Kunwar and Z. F. Ren, *Nanotechnology* **2005**, 16, 1126.
- [23]. R. R. Kumar, K. N. Rao and A. R. Phani, *Appl. Nanosci.* **2011**, 1, 211.
- [24]. P. K. Giri and S. Dhara, *J. Nanomater.* **2012**, 2012, 905178.

-
- [25]. K. Kinoshita, *Carbon: Electrochemical and Physicochemical Properties*, Wiley, New York, **1988**.
- [26]. Z. Sui and I. P. Herman, *Phys. Rev. B* **1993**, *48*, 17938.
- [27]. Y. Maeda, N. Tsukamoto, Y. Yazawa, Y. Kanemitsu and Y. Masumoto, *Appl. Phys. Lett.* **1991**, *59*, 3168.
- [28]. J. R. Heath, J. J. Shiang and A. P. Alivisatos, *J. Chem. Phys.* **1994**, *101*, 1607.
- [29]. Y. F. Zhang, Y. H. Tang, N. Wang, C. S. Lee, I. Bello and S. T. Lee, *Phys. Rev. B* **2000**, *61*, 4518.

9. Conclusions

The major challenges in the ITRS based industries for device miniaturisation are increasing costs, the need for high end lithographic tools and increasingly challenging plasma etch processes. These issues are addressed in this thesis and here is reported an extension beyond the current lithographic limitations using self-assembly methods. Here, we propose the development of new block copolymer (BCP) techniques which may provide novel non-conventional methods quite different to other methods of device structure fabrication. Fabrication of well determined silicon nanostructures over a large scale was demonstrated.

Here we report a qualitative and quantitative detailed study of silicon nanowire fabrication and its feature size reduction by different BCP systems. Researchers in the BCP world mainly deal with reducing the feature size by use of a particular BCP molecular weight. We extended this conventional pathway of feature size reduction using various BCP and also by previously unreported plasma-over etch technique. Achieving good fidelity and sub-10 nm feature size were the main goal in this work and this was achieved using PS-*b*-PMMA BCP systems of four different molecular weights say 85k-91k, 52k-52k, 37k-37k and 18k-18k.

Depending on the molecular weight of PS-*b*-PMMA BCP system the feature size of silicon nanowires can be tuned in a controlled manner. This BCP lithography, especially on molecular weight based methodology has not been reported anywhere before with a systematic study of Si structure using TEM cross-sections of the individual silicon features of as a function of molecular weight. The molecular weight based size reduction is predictable, reproducible and reliable. This method does not involve any other etch mask of feature size enhancement. The major challenge in all these methods is the etch process in the pattern transfer of BCP to the underlying substrate which is achieved in this work with a low aspect ratio. In order to get the desirable aspect ratio of the silicon features, the etch plasma conditions like pressure, time and gas flow rate must be very carefully optimised. Since the ICP plasma etcher has a high efficient gas, the etch was very quick and as a consequence it was difficult to control the aspect ratio. A detailed study of plasma etch pattern transfer is reported here and has been discussed with the aid of high resolution TEM images that show the crystalline arrangements of the silicon

features. This phenomenon was shown in both bulk silicon and silicon on insulator (SOI) substrates. Physically and electrically isolated silicon nanowires were shown on the SOI substrates with a high fidelity and reproducibility. Both the bright field and dark field images prove the patterns created that are highly consist of ordered arrangement of silicon features in the sub-10nm nanoscale region.

A Plasma over etch technique was applied, examined and reported in this thesis for the feature size reduction of device structures. This simple but powerful technique can create almost ideal features for CMOS device fabrication. PS-*b*-PMMA BCP systems of high and low molecular weights 85k-91k and 18k-18k were used for this particular study. The plasma etch stability and its critical dimension limitations were evident in this thesis. Previous work in BCP lithography has largely been as “one-off” demonstrations of capability rather than detailed and systematic investigation of the processes. Here, we have carried out a range of work which should help to establish the methodology and provide understanding of the fundamental barriers that might limit its progress towards industrial use. It has been proven that it is a reliable, reproducible and suitable methodology for large substrate areas patterning. Highly crystalline features are generated and generally show little sign of physical damage. Substrate features generated in this way were not ideally regular and shape anisotropy was present due to fundamental limitations of the etch mask and the etch processes. These limitations are more easily seen in smaller features. This limiting size may be related to the intrinsic mechanical properties of low diameter features or to their shape that is imposed on them through the pattern transfer techniques used.

The other promising polymer system for the sub-10 nm features fabrication with a pitch size of sub-16 nm is the PS-*b*-PDMS system. Most of the literature discusses PS-*b*-PDMS pattern alignment on the substrates. Here, we reported the pattern alignment on both the planar and grapheoepitaxial substrates and, more importantly, the pattern transfer to the underlying silicon. Unlike the PS-*b*-PMMA pattern transfer, PS-*b*-PDMS needs complex plasma etch procedures for a successful pattern transfer with good selectivity and aspect ratio. The major difficulty in PS-*b*-PDMS pattern transfer appears to be the wetting PDMS layer above the substrate and the top residual layer. In all likelihood, due to this problematic process, researchers

have been unable to show the pattern transferred cross-sectional images in other of the literature studies. However, in this thesis we successfully proved that it is possible to fabricate sub-8 nm features after pattern transfer using high resolution cross-sectional images. The controlled etch process shows the aspect ratio of the wires and the PS-*b*-PDMS system shows long range alignment of over almost macroscopic dimensions at both planar and graphoeptaxy substrates.

The etch results demonstrate a pitch size of 16 nm can be achieved and beyond state-of-the-art device fabrication can be readily attained by use of lower molecular weights of these BCP systems. The evidence of the plasma over etch process and the possibility of using lower systems molecular weight proves that still we remain in the era of Moore's law and scaling can be continued to be for several years and certainly beyond the 16 nm technology node. The other important aspect of device fabrication is the defect density (DD) parameter, which is the most important factor in determining the performance of the device. Here, we clearly reported defect density from high resolution SEM images. Though the DD seems quite high for the higher molecular weights of PS-*b*-PMMA for 18k-18k it was only 25-30/ μm^2 which must be reduced in further high grade cleanroom which could be used for BCP deposition. We performed BCP deposition in ambient conditions and observed a reasonably low defect density with little effort.

Electrochemical sensing properties of silicon nanowires are well demonstrated and show better sensitivity and selectivity compared to other previously reported studies. These studies demonstrate an important application of sub-10 nm silicon wires fabricated using BCP system due to their high surface to volume ratio.

Furthermore, a PS-*b*-PMMA BCP template was used to fabrication of 3-D copper and germanium nanowire array. The methodology of using BCP template can be used for fabrication of many kinds of materials for even modern semiconductor device industries. The techniques described here provide a powerful way of producing nanostructures in large scale and, may have considerable importance in fields other than silicon scaling for processor applications.